PNNL-13682

Annual Report

Development of a Remotely Operated NDE System for Inspection of Hanford's Double Shell Waste Tank Knuckle Regions

*A. F. Pardini

*J. M. Alzheimer
*S. L. Crawford
*A. A. Diaz
*K. L. Gervais
*R. V. Harris
*D. M. Riechers
*T. J. Samuel
*G. J. Schuster
*J. C. Tucker
*Pacific Northwest National Laboratory

- R. A. Roberts
-Center for NDE at Iowa State University

September 2001

Prepared for the U.S. Department of Energy
under Contract DE-AC06-76RLO 1930

This work is funded by the Office of Science and Technology
within the Energy's Office of Environmental Management
under the Tanks Focus Area Program

ANNUAL REPORT

Development of a Remotely Operated NDE System for Inspection of Hanford's Double Shell Waste Tank Knuckle Regions

*A. F. Pardini

*J. M. Alzheimer
*S. L. Crawford
*A. A. Diaz
*K. L. Gervais
*R. V. Harris
*D. M. Riechers
*T. J. Samuel
*G. J. Schuster
*J. C. Tucker
*Pacific Northwest National Laboratory

- R. A. Roberts
-Center for NDE at Iowa State University

September 2001

Prepared for the U.S. Department of Energy
under Contract DE-AC06-76RLO 1930

This work is funded by the Office of Science and Technology within the Energy's Office of Environmental Management under the Tanks Focus Area Program, Technical Task Plan RL37C131

Summary

The need to examine the knuckle region of Hanford's double shell tanks (DSTs) has received considerable attention over the past couple of years. Commercial, off-the-shelf systems to examine the knuckle are not available. Preliminary tests at the Pacific Northwest National Laboratory (PNNL) in FY 1999 indicated that a unique technology utilizing ultrasonics could provide a solution to the knuckle examination problem. In FY 2000 PNNL embarked on a study to provide evidence that the ultrasonic technology had the capability to detect and size stress corrosion cracks in the knuckle region of the DSTs.

Analysis of the examination results conducted at PNNL in FY2000 provided engineering data strongly supporting a proof-of-principle concept for utilizing a combination of pulse-echo Synthetic Aperture Focusing Technique (SAFT) and tandem-SAFT (T-SAFT) inspection methodologies. These methods can be applied to the problem of flaw detection, localization, and sizing in Hanford's double shell waste tank knuckle region and beyond.

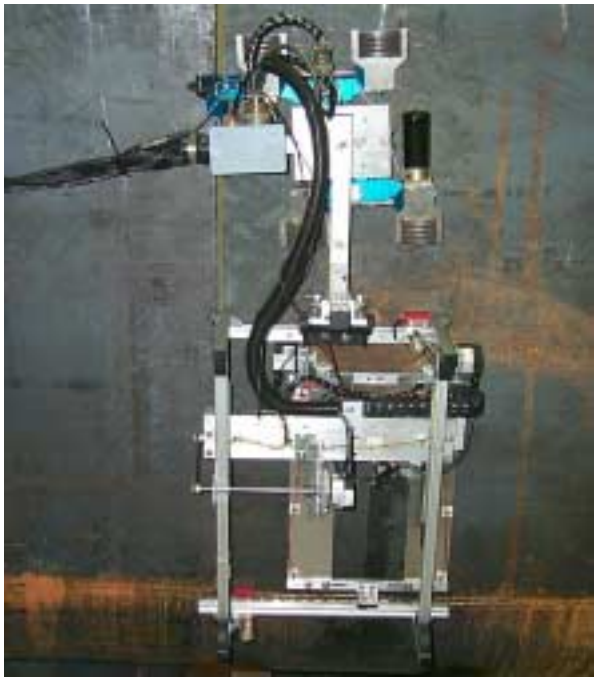

Based on the results of the work completed in FY2000, PNNL began the design and fabrication of a prototype system capable of examining the knuckle region of the DSTs. This ultrasonic system known as the Remotely Operated Nondestructive Examination (RONDE) system shown here has completed initial demonstrations in September 2001.

In support of the FY01 testing, three tank knuckle mockups were fabricated from carbon steel. The mockups contained a variety of machined defects that simulated cracking within the knuckle region. These mockups proved invaluable in supporting the development effort. The mockups allowed PNNL researchers to test different system protocols in an effort to provide the best system configuration for characterization of the tank flaws.

Results of initial tests of the RONDE system have exceeded our performance expectations. All simulated defects in all of the mockups were readily detected. PNNL sized all of the flaws in the knuckle region. The sizing results are shown here.

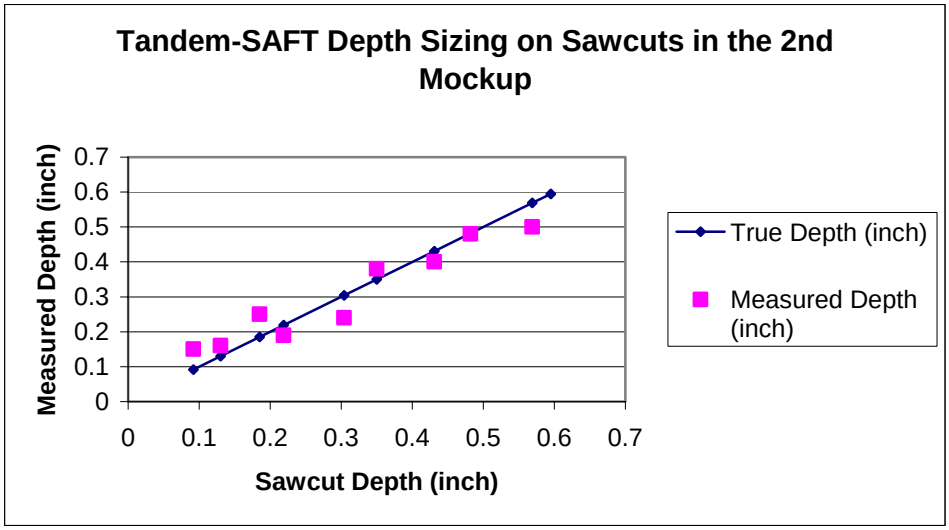

The RMS error associated with the sizing demonstration was 1.2 mm (0.047 in.) well within the Hanford requirements of 2.54 mm (0.10 in.). In addition, simulated flaws have been readily detected at distances exceeding 1067 mm (42 in.) from the transducer. This capability opens the door to performing tank inspections in a much more comprehensive and time effective manner.

Work planned for FY02 includes a complete acceptance test of the entire prototype system as well as a performance demonstration test. PNNL has been contracted to fabricate a cracked knuckle mock-up that will have actual stress corrosion cracks in it to support further testing of the RONDE system. Deployment into the annulus of a DST is scheduled for the 3rd quarter of FY02.

Results from the successful development and testing of the remotely operated NDE system, that utilizes the SAFT/T-SAFT technology, clearly demonstrated its capability to provide required tank knuckle information throughout the knuckle region and significant distances onto the floor of the tank.

The work described in this report was funded and supported by the U.S. Department of Energy's (DOE) Tanks Focus Area (TFA) Safety program under the coordination of Mike Terry. The TFA provides science and technology solutions to safely and efficiently remediate waste stored in underground storage tanks at five DOE sites.

Acknowledgments

The authors acknowledge the contributions of the following PNNL staff members: Kimberly Lessor for her assistance in electrical wiring and connectors support, Lindsey Johnson, AWU student who assisted in data acquisition, and Twilla Knowles and Karen Salisbury-Miller who supported us with administrative assistance.

The authors would also like to acknowledge the contributions of Mr. Mike Terry, Tanks Focus Area Safety Technical Integration Manager, and Mr. Chris Jensen from CH2M Hill Hanford Group for problem definition and reviews.

Table of Contents

List of Figures

Tables

1 Introduction

One of the key elements in ensuring the integrity of the Hanford's Double-Shell Tanks (DSTs) is the examination of the knuckle region of the primary tank. This examination poses a significant technical challenge because the area that requires examination is not accessible using conventional measurement techniques. The Pacific Northwest National Laboratory (PNNL) has offered a possible solution to this problem. Utilizing an advanced signal processing method known as Synthetic Aperture Focusing Technique (SAFT), PNNL proposed to introduce sound waves from above the knuckle region where access is readily achieved and examine the knuckle region below. The sound is divergent in nature and propagates around the knuckle and along the bottom of the waste tank. Work performed by PNNL in FY00 provided a solid foundation for development of a knuckle inspection system (Pardini et al., 2001). The SAFT technique provides a detection and location method for cracks in the knuckle region. An advanced nondestructive evaluation (NDE) method known as Tandem-SAFT or T-SAFT utilizes two transducers in a pitch-catch mode to characterize the detected crack. T-SAFT has the ability to accurately size the crack both in length and depth.

This report documents work performed at PNNL in FY01 to support development of a Remotely Operated NDE (RONDE) system capable of inspecting the knuckle region of Hanford's DSTs. The development effort utilized commercial off-the-shelf (COTS) technology wherever possible and provided a transport and scanning device for implementing the SAFT and T-SAFT techniques. PNNL contracted for the fabrication of carbon steel mockups that were used for deployment and testing during the development effort. These carbon steel mockups contained simulated defects that were used for calibration as well as for testing the detection and sizing capabilities of the system.

This document has been divided into ten major sections. Section 2 describes the requirements that must be met for the successful examination of the knuckle region of the DSTs. Section 3 provides background information on SAFT and T-SAFT technology. Section 4 provides information on the mockups used during the development of the RONDE system. Section 5 describes the mechanical design of the deployment device used for placement of the ultrasonic transducers for data acquisition. Section 6 describes the control system design for the deployment device and the SAFT/T-SAFT data acquisition. Section 7 describes the electronic design of hardware used for data acquisition and control. Section 8 describes the SAFT/T-SAFT software and modifications necessary for data focusing and data visualization. Section 9 provides an analysis of the test results. Section 10 provides modeling activities associated with the empirical data. Section 11 discusses the demonstrations performed in FY01. Section 12 provides conclusions for work performed in FY01 and Section 13 outlines work planned for FY02.

Two demonstrations occurred in FY01 to provide status of the ongoing work. A Demonstration Test Plan was written to outline the necessary steps for a successful demonstration. The Demonstration Test Plan is included as Appendix A to this

document. Also included in this document is a draft operating procedure to provide preliminary instructions for the inspection of the DST knuckle region.

2 Requirements

To assure that the DSTs at Hanford maintain their structural integrity, an inspection plan was developed and implemented (Pfluger 1994). This inspection plan describes the ultrasonic testing (UT) system, the qualification of the equipment and procedures, field inspection readiness, DST inspections, and post-inspection activities. The plan also provides the basis for the flaw characterization requirements. Utilizing this information, a Functions and Requirements (F&R) document was developed by PNNL (Pardini et al., 2001) to define a system capable of reliably examining the knuckle region of the primary waste tank. Specifically, PNNL is chartered with developing a Nondestructive Examination (NDE) system to examine the knuckle region. PNNL examined this inspection challenge and determined that the best approach would be based on using SAFT, and an advanced NDE sizing technique utilizing tandem transducers known as T-SAFT.

The flaw characteristics of interest are planar flaws located in the knuckle region emanating from the inside surface of the tank. This region contains the highest stress point of the entire primary steel tank (Shurrab et al., 1991). Examinations shall concentrate on cracks that are caused by stress corrosion and are circumferentially oriented. Figure 2.1 provides a graphical example of a planar-type stress corrosion crack that is of interest.

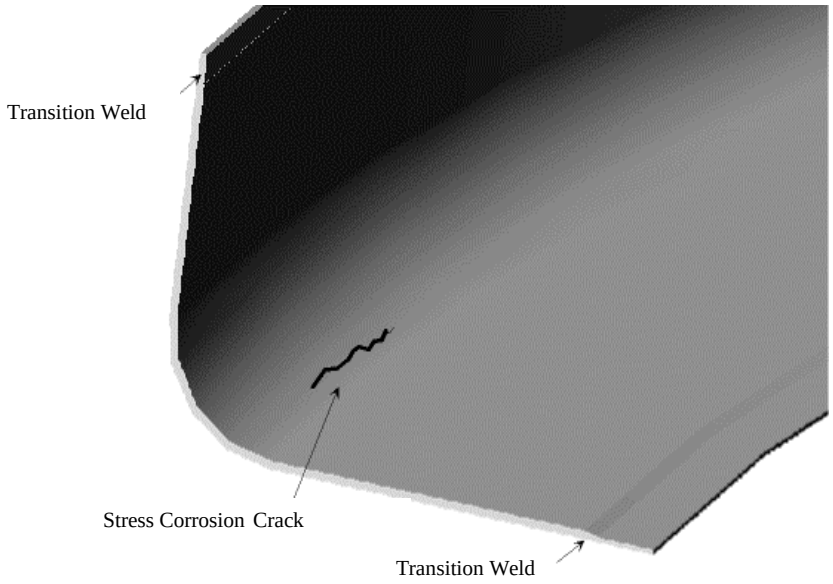

Figure 2.1. Planar Crack on Primary Tank Inside Diameter

The flaw characterization requirements (Pfluger 1995, Jensen 2001) stipulate the minimum dimension required to be characterized and specific accuracy requirements. Circumferential cracks emanating from the inside surface of the primary tank shall be detected when the crack depth is greater than 0.2t where t is the thickness of the knuckle region. Characterization of the crack shall be in accordance with Table 2.1.

Table 2.1. Sizing Requirements

Condition	Minimum Dimension To be Characterized (1)	Accuracy
Cracks (circumferential)	305 mm (12 in.) long x 0.2t deep	± 2.54 mm (±0.100 in.) (depth) ± 25.4 mm (±1.00 in.) (length)

[1] Nominal tank wall thickness is t.

The SAFT/T-SAFT system shall be capable of detecting planar flaws located in the knuckle region of the primary tank. The knuckle region as shown in Figure 2.2 describes the inspection areas. The inspection area begins just above the construction weld on the vertical portion of the tank and extends just past the transition weld located on the tank bottom. Locations of construction welds vary depending on which tank farm is being inspected.

Requirements for the detection and characterization of pitting, wall thinning, and cracks oriented in the meridional direction were not addressed in the FY01 work. PNNL will perform preliminary tests in FY02 to establish whether these types of anomalies can be detected and characterized by SAFT/T-SAFT.

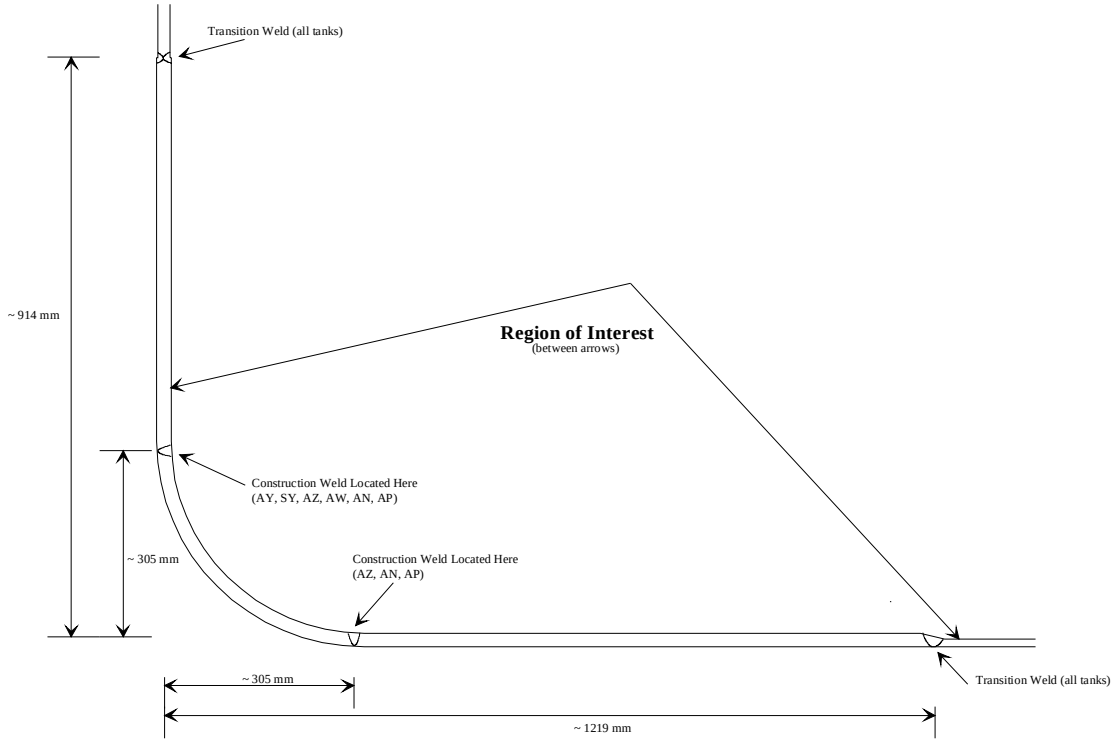

Figure 2.2. Examination Parameters in Knuckle Region

3 Technology Background

3.1 SAFT Technology

SAFT technology is able to provide significant enhancements to the inspection of materials when using unfocused ultrasonic transducers where the attenuative effects of path length, material noise, and sound beam divergence are evident. The resolution of all imaging systems is limited by the effective aperture area, that is, the area over which data can be detected, collected, and processed. SAFT is an imaging method, which was developed to overcome some of the limitations imposed by large physical transducer apertures, and has been successfully applied in the field of ultrasonic testing. Relying on the physics of ultrasonic wave propagation, SAFT is a very robust technique.

"Synthetic aperture focusing" refers to a process in which the focal properties of a large-aperture focused transducer are synthetically generated from data collected over a large area using a small transducer with a divergent sound field (Hall et al., 1988). The processing required to focus this collection of data has been called beam-forming, coherent summation, or synthetic aperture processing. The resultant image is a full-volume, high resolution, and high signal to noise ratio (SNR), focused characterization of the inspected area.

Utilizing the pulse-echo configuration for typical data collection, the transducer was positioned on the surface of the PNNL mockups, and radio frequency (rf) ultrasonic data were collected. As the transducer was scanned over the surface of the specimen, the A-scan records (rf waveform) were amplified, filtered, and digitized for each position of the transducer. Each reflector produced a collection of echoes in the A-scan records. The unprocessed rf data sets were then post-processed using the SAFT algorithm, and invoking a variety of full beam angle values (between 1 degree and 12 degrees) in an attempt to optimize the spatial averaging enhancement.

If the reflector is an elementary single point reflector, then the collection of echoes will form a hyperbolic surface within the data-set volume. The shape of the hyperboloid is determined by the depth of the reflector in the specimen and the velocity of sound in the specimen. This relationship between echo location in the series of A-scans and the actual location of the reflectors within the specimen makes it possible to reconstruct a high-resolution, high SNR focused image from the acquired raw data.

If the scanning and surface geometries are well known, it is possible to accurately predict the shape of the locus of echoes for each point within the test object. The process of coherent summation for each image point involves shifting a locus of A-scans, within a regional aperture, by predicted time delays and summing the shifted A-scans. This process may also be viewed as performing a spatial matched filter operation for each point within the volume to be imaged. Each element is then averaged by the number of points that were summed to produce the final processed value. If the particular location correlates with the elementary point response hyperboloid, then the values summed will be in phase and produce a high-amplitude result. If the location does not correlate with

the predicted response, then destructive interference will take place and the spatial average will result in a low amplitude value, thus reducing the noise level to a very small value.

All SAFT processing software was contained in and invoked on a personal computer (PC) workstation. The SAFT imaging software provides the user the capability to view the entire ultrasonic data set (three-dimensional array of points) in two-dimensional slices. The software provides a platform for viewing color-enhanced composite images that depict slices of the three-dimensional array in the X-Y plane (C-scan view), the Y-Z plane (B-Scan end-view) and X-Z plane (B-scan side view).

3.2 T-SAFT Technology

A single transducer in pulse-echo configuration works well for location and detection of a defect but may provide ambiguous results for sizing of the defect in the knuckle region and beyond due to the lack of a tip-diffracted signal. The tandem configuration reduces the ambiguities and improves sizing of vertical defects. During the examination of the mockups, the pulse-echo configuration coupled with SAFT processing was used for detection and localization of a defect, and this information was used to optimize the spatial positioning for a tandem configuration to be implemented for sizing of the defect.

Fundamentally, the tandem SAFT (T-SAFT) configuration provides a uniform illumination of the vertical object plane. The central ray of the transmitter's divergent beam is always centered on the receiving transducer by scanning the transmitter synchronously but in the opposite direction of the receiver. At the completion of each pass of the transmitter and receiver, the two-transducer configuration is incremented so that a rectilinear pattern is obtained. Since a more uniform illumination of the vertical object plane is possible, the vertical extent of a defect can be accurately measured. When both paths are collected and processing occurs beyond the far surface, the result is a real and conjugate image. Sizing is accomplished by measuring the extent of the real and conjugate images and dividing the resultant value by two. In the T-SAFT mode, the transmitter initially starts in front of the receive transducer. Both transducers are scanned equal distances but in opposite directions as shown in Figure 3.1 (top view) and Figure 3.2 (side-view).

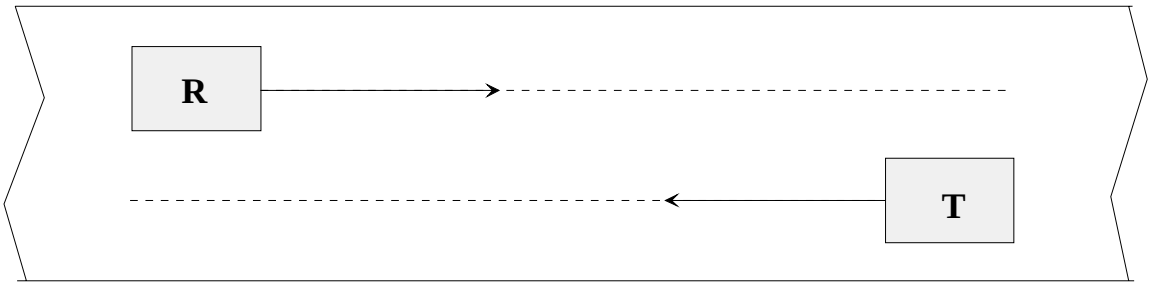

a) Initial Position of Transducers for T-SAFT Scanning (Top View)

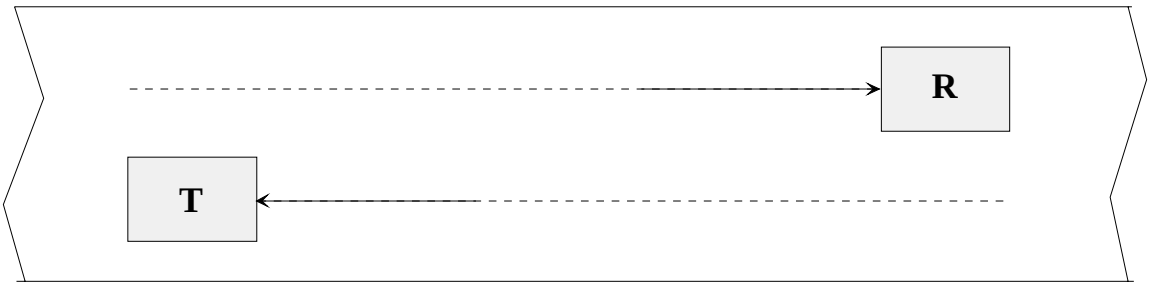

b) Final Position of Transducers for a Single Pass in T-SAFT Scanning Mode (Top View)

Figure 3.1. T-SAFT Scanning Transducer Configuration

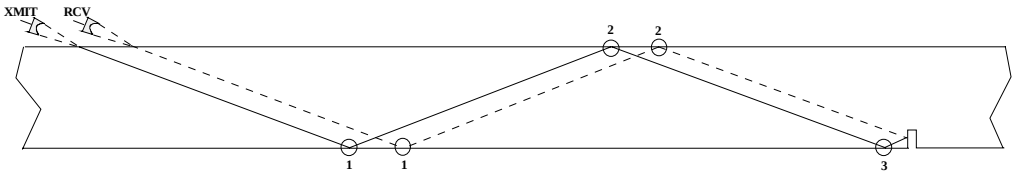

Figure 3.2. Side View Showing V Paths

Tandem image analysis uses techniques similar to those of pulse-echo analysis. Defects may be categorized as volumetric, planar, or crack. The primary difference between the tandem and pulse-echo image is that the tandem image of a crack presents the entire cross section of the crack and not just the corner-trap and tip-diffracted echoes. Often, the tip-diffracted echo is very illusive because of the weak nature of the tip-diffracted echo compared to the very strong corner-trap echo; and without a tip-diffracted echo, the vertical extent of a crack is difficult to estimate.

The signal-to-noise ratio of a tandem image is often much superior to that of a pulse-echo image, because a separate receiver eliminates noise caused by the initial pulse, the near surface interface, and the specular backscatter from the material structure under examination. Tandem image indications are vertical in appearance, as opposed to the slanted (projected) appearance of a pulse-echo image. The location of the indication within the image space is influenced by the material thickness, velocity, and refracted angle. The wall thickness in the area of the knuckle region is assumed to be accurately known. The SAFT/T-SAFT algorithm implemented at PNNL assumes isotropic and homogeneous material with respect to acoustic velocity; that is, the calculations performed by the SAFT processing algorithm make the approximation that the velocity is constant throughout the material. Also, the algorithm requires that the acoustic velocity of the material under test be known to some degree of accuracy. This is the case with the carbon steel specimens used as mockups.

3.3 Signal Processing Parameters

The SAFT signal processing algorithm requires the entry of multiple parameters that affect the resultant processed output. This section describes the basis for using the various signal processing parameters employed on the raw data. The SAFT processing software requires the operator to enter pertinent information associated with the transducer(s) used, the acoustic modality, refracted angle, frequency, geometric information, material property information, sampling information and so forth. These parameters vary in their significance with regard to their affect upon the resultant processed output.

The RONDE system utilizes 70-degree shear waves as the primary inspection modality. The transducers used are circular-contact, flat piston radiators, 12.7 mm (0.50 in.) in diameter with nominal center frequencies of 3.5 megahertz (MHz). The transducers are affixed to wedges that provide the correct incident angle for propagation of 70-degree shear waves in the tank knuckle mockups. The full beam angle (entered in degrees) affects the processed image and determines the size of the synthetic aperture to be used when SAFT processing is performed. Typically, small beam angles are used initially to reduce the processing time and larger angles are used later if a higher image quality is desired. Utilizing the line SAFT code developed during this FY allows the operator to process the rf data with a 12 degree processing angle. The beam entry diameter also affects the processed image. SAFT assumes a synthetic aperture with a point source at the beginning, expanding in the general shape of a cone. Since the aperture is small at the near surface, the number of off-center A-scans used during processing is also small. In order to take advantage of the spatial averaging inherent in SAFT processing, the operator typically enters a value equal to one-half the transducer element diameter. The effect on the synthetic aperture used in the processing is to create a cylinder with a diameter equal to the beam entry diameter parameter that would extend into the material until it intersects the normal aperture cone.

Material properties are also very important to the processing scheme. In the case of the knuckle wall, the material type, wall thickness and acoustic properties are all known to a

high degree of accuracy. Sampling information includes parameters that are related to the temporal sampling (digitization) of the waveform as well as the use of linear averaging for reduction of electronic (white) noise. In order to achieve sufficient sampling, a sample rate of 25 MHz was employed. At an examination frequency of 3.5 MHz, this corresponded to a digitization rate of approximately 7 points per cycle. Due to the attenuative effects of long path lengths and beam divergence, the receive amplifier was required to operate at high levels. The step increment in both the X and Y-axes affects the quality of the processed image. Typically, increment steps of $\lambda/2$ (where λ is the wavelength) are desired; however, in order to reduce file sizes to more manageable levels and decrease the processing times, slightly larger increment step sizes were used in certain instances. The wavelength in the knuckle material was approximately 0.91 mm (0.036 in.), and the incremental step size in both axes was nominally kept at .76 mm (0.030 in.). Finally, selection of a threshold value for processing can affect the resultant processed file. If a threshold value is selected, and the amplitude of any elementary data element being processed is below this threshold value, then no off-center A-scans will be summed. In this study, a threshold value of -20 dB (corresponding to 10% of the maximum value) was used in order to increase processing speed; however, the threshold value was lowered to 0 dB later on specific scans to help detect the lower weld signal.

4 Mockups Used for RONDE Development

Various mockups have been fabricated for use in the development of the RONDE system. One of the mockups provides a standard set of end-mill notches that can be used for calibration of the system. The second mockup contains a variety of simulated flaws. The flaws were fabricated using a circular abrasive wheel thereby producing a flaw indication called a saw cut.

4.1 Calibration Standard

A calibration standard mockup was fabricated using the same type carbon steel as was used on the construction of the DSTs. The material that was used for the mockup was A516 Grade 70 carbon steel. End-mill notches at 10% deep were placed into the knuckle region at selected areas. Figure 4.1 shows a drawing of the calibration standard mockup. The mockup was used to provide a reference amplitude of the ultrasonic signal at known distances from the transducer. This reference amplitude was used to assist in the characterization of a flaw.

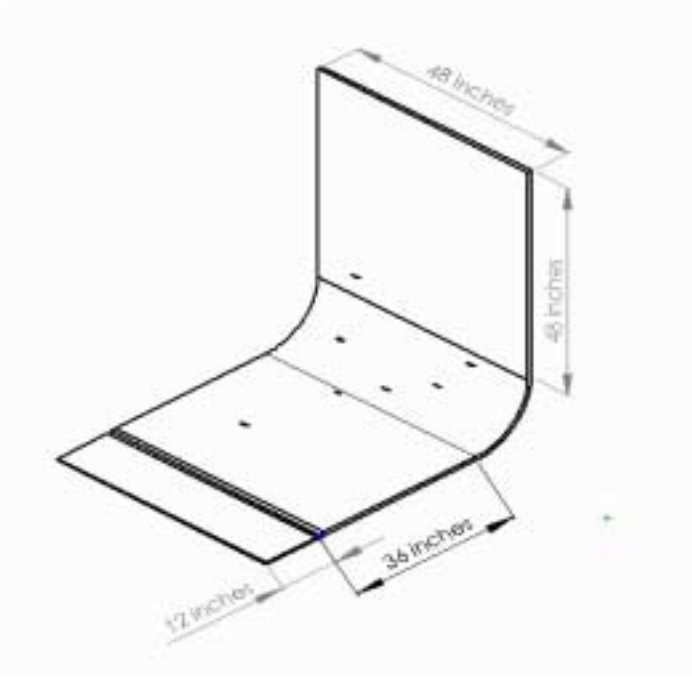

Figure 4.1. Calibration Standard Mockup

4.2 Flaw Standard

A flaw standard was created to assist in the detection and sizing of flaws that would simulate a crack developing in the knuckle region of the DST. Table 4.1 provides a listing of the flaws within the mockup and their dimensions.

Table 4.1 Saw Cut Dimension in the Knuckle Region of Flaw Standard Mockup

Through Wall Depth (%)	True Depth mm (in.)	Axial Position mm (in.)	Starting Circumferential Position mm (in.)	Length mm (in.)
10	2.3 (0.092)	88.8 (3.5)	947.42 (37.3)	33.02 (1.3)
15	3.3 (0.13)	368.3 (14.5)	490.22 (19.3)	40.64 (1.6)
20	4.7 (0.185)	254.0 (10)	205.74 (8.1)	48.26 (1.9)
25	5.6 (0.219)	463.6 (18.25)	896.62 (35.3)	53.34 (2.1)
35	7.7 (0.304)	254.0 (10)	396.24 (15.6)	60.96 (2.4)
40	8.9 (0.35)	25.4 (1)	566.42 (22.3)	66.04 (2.6)
50	10.9 (0.431)	120.7 (4.75)	312.42 (12.3)	71.12 (2.8)
55	12.2 (0.482)	196.9 (7.75)	744.22 (29.3)	73.66 (2.9)
65	14.4 (0.569)	254.0 (10)	655.32 (25.8)	83.82 (3.3)
70	15.1 (0.595)	444.5 (17.5)	154.94 (6.1)	83.82 (3.3)

Figure 4.2 shows the location of the flaws on the flaw standard mockup. Ten flaws are located on the ID of the knuckle region. To assist in the RONDE system's capability to distinguish between ID and OD flaws, a pair of flaws was placed on the OD and is not reflected in Table 4.1.

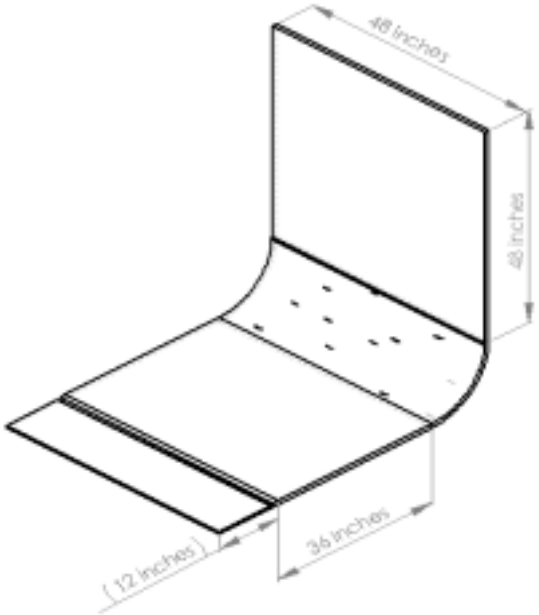

Figure 4.2. Flaw Standard Mockup

5 RONDE Mechanical Design

The RONDE crawler bridge scanning system consists of two primary system components: the motorized magnetic crawler and the X and Y scanning bridge system. When attached they measure 18.5” in width, 47.0” in length and 9.5” in height. Figure 5.1 provides the design concept of the RONDE crawler bridge scanning system as shown on a simulated mockup.

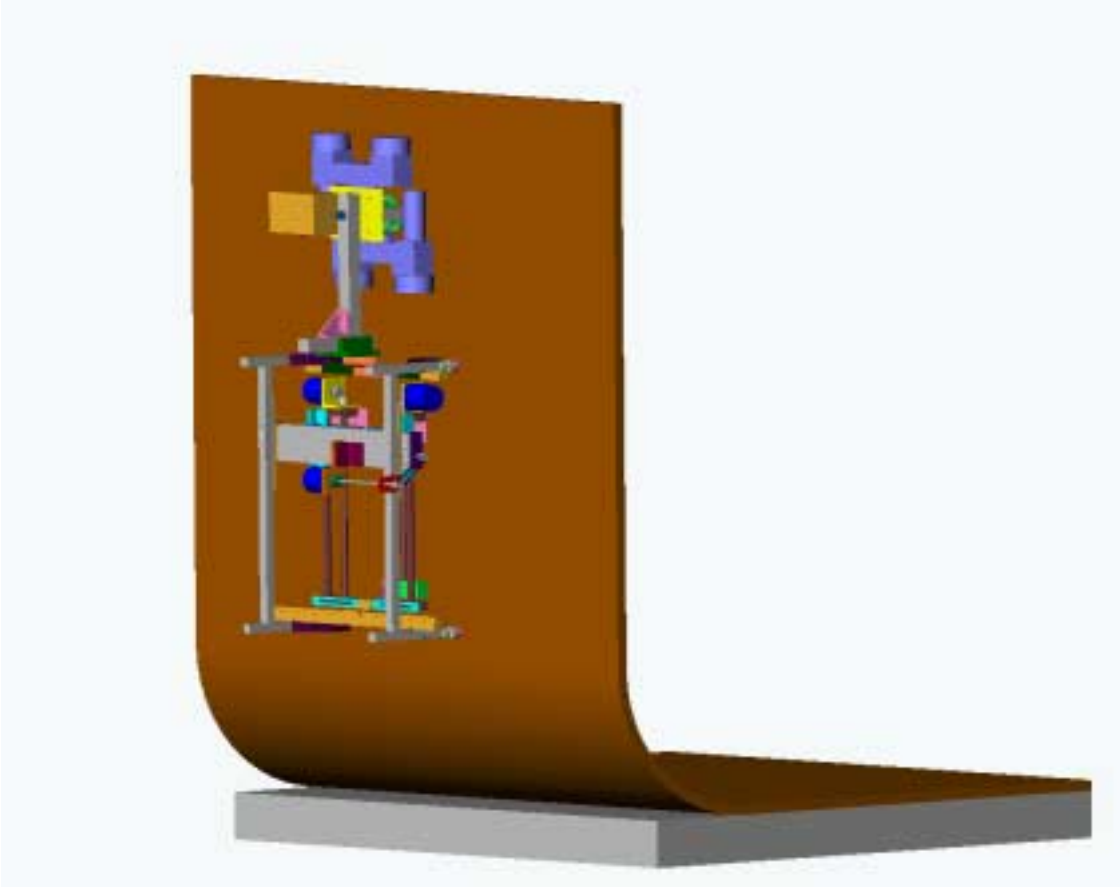

Figure 5.1. Design of the RONDE Shown on Simulated Mockup

5.1 Magnetic Wheel Crawler

The crawler is designed to maneuver the scanning bridge on the tank wall. It performs this gravity-defying feat by means of permanent magnetic wheels. The wheels are on a four-wheel independent suspension. The crawler uses skid steering for turning and is operated by a remote joystick. The joystick cable is 425 ft. long. Two independent DC motors power the wheels. The crawler has a maximum speed of 254 mm (10 in.) per

second and has an encoder for real time distance traveled. The crawler weighs 20 pounds and can accommodate a 40-pound payload without slipping.

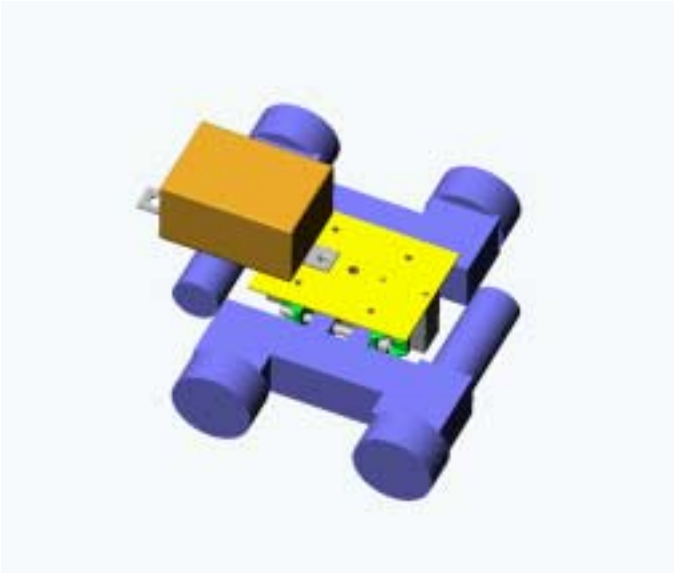

The crawler is an off-the-shelf product with the exception of one additional factory installed magnet per wheel. These additional magnets increase the crawler's payload capacity. Figure 5.2 shows the design drawing of the magnetic wheel crawler and Figure 5.3 shows the off-the-shelf crawler purchased for this application.

Figure 5.2. Design Drawing of Magnetic Wheel Crawler

Figure 5.3. Off-the-Shelf Crawler

5.2 Scanning Bridge

The scanning bridge controls the X and Y movements of the transducers. It hangs freely from the crawler like a pendulum. This feature permits the crawler to turn in any direction and transverse the wall at any angle desired. The bridge weighs 28.6 pounds. It uses high precision linear worm drive assemblies for positioning. The maximum X and Y scan distances are 305 mm (12 in.). The Compumotor brand stepper motors mounted on the bridge control accurate positioning of the transducers. The transducers are mounted on low profile spring-loaded transducer arms. These transducers have the means of being lifted from the tank wall for the journey to the scan location. Once the bridge has been positioned at the scan location electromagnets are activated to lock the bridge in place for the 305 mm (12 in.) scan.

Figure 5.4. Design Drawing of the RONDE Scanning Bridge

After completing the scan the bridge magnets are released and the crawler is driven forward approximately 305 mm (12 in.) or less. The crawler encoder ensures the accuracy of the distance driven forward. Bosch aluminum structural framing and components were predominately used because of their prototypic versatility, cost effectiveness and lightweight intrinsic characteristics. Figure 5.4 shows the design drawing of the scanning bridge and Figure 5.5 shows the custom design scanning bridge fabricated for this application.

Figure 5.5. Custom Scanning Bridge

6 RONDE Control System Design

The RONDE control system is composed of three main components:

- RONDE magnetic wheel crawler and scanning bridge
- Tank top electronics
- Control station

The diagram shown in Figure 6.1 provides the general layout of components at the tank farm. Approximately 100 ft. of multi-conductor cable separates the crawler/scanning assembly from the tank top electronics. Approximately 425 ft. separates the tank top electronics from the control station. This 425 ft. connection consists of a small multi-conductor cable for the joystick and a single fiber optic cable with two fibers for data and control of the remote computer.

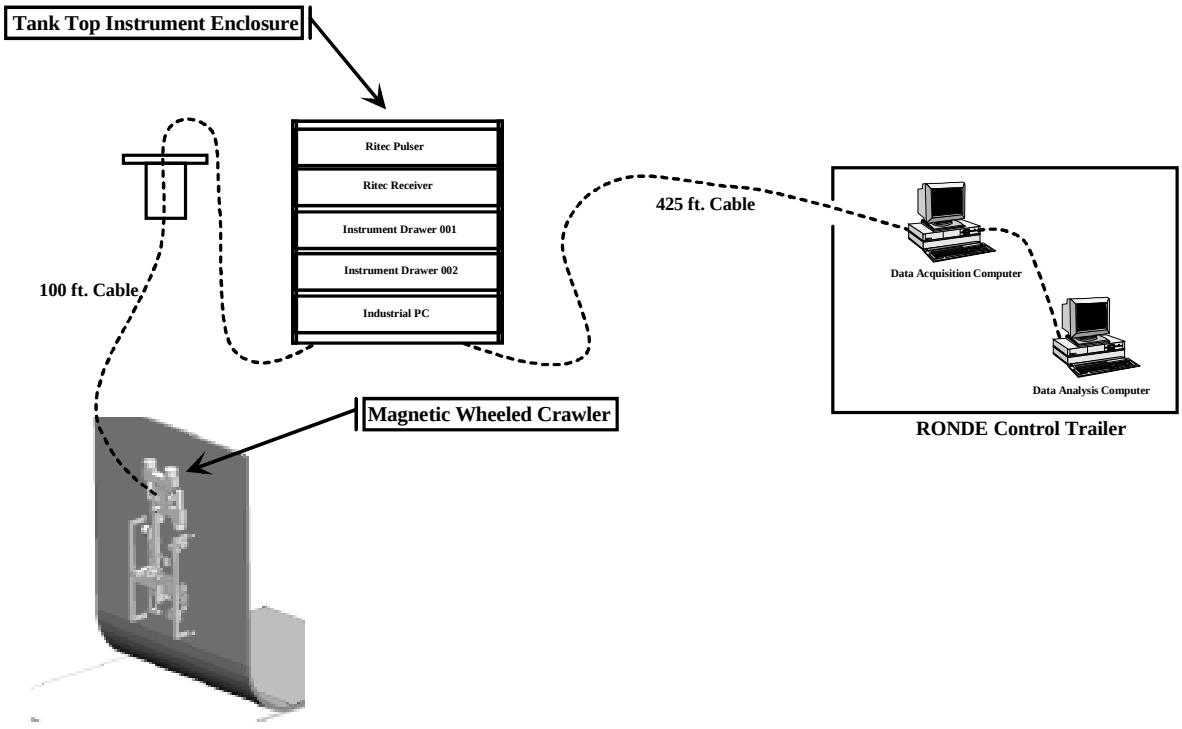

Figure 6.1. General Layout Diagram

6.1 RONDE Control

PNNL designed the RONDE control system around existing control architecture that was developed under a previous contract with the U. S. Nuclear Regulatory Commission (USNRC). Control system design is similar to the previous NRC SAFT/T-SAFT control

system designs, with the main exception being that newer hardware has replaced the motor control system. In this case a Parker 6K4 universal controller has replaced a Parker AT6400 motor controller. The new 6K4 controller is self-contained, and utilizes either serial communications or Ethernet communications for the connection to the host computer. The older AT6400 controller was mounted in the host computer on the ISA bus. Since the ISA bus has been removed from most new computers, it was decided that it was time to upgrade the motor controller from previous SAFT/T-SAFT systems. For the RONDE system, a serial link between the host computer and the 6K4 controller was used.

The 6K4 controller is a low level motor controller that works in conjunction with the Parker Zeta stepper motor drives. It provides an interface between the motor drives, which supply power to the stepper motors, and the host computer. Commands are given to the 6K4 controller by the host computer, which is translated into electrical pulses that are sent to the stepper motor drives. The stepper motor drives translate these electrical pulses into motor drive pulses for the stepper motors. A block diagram of the system is included in Figure 6.2.

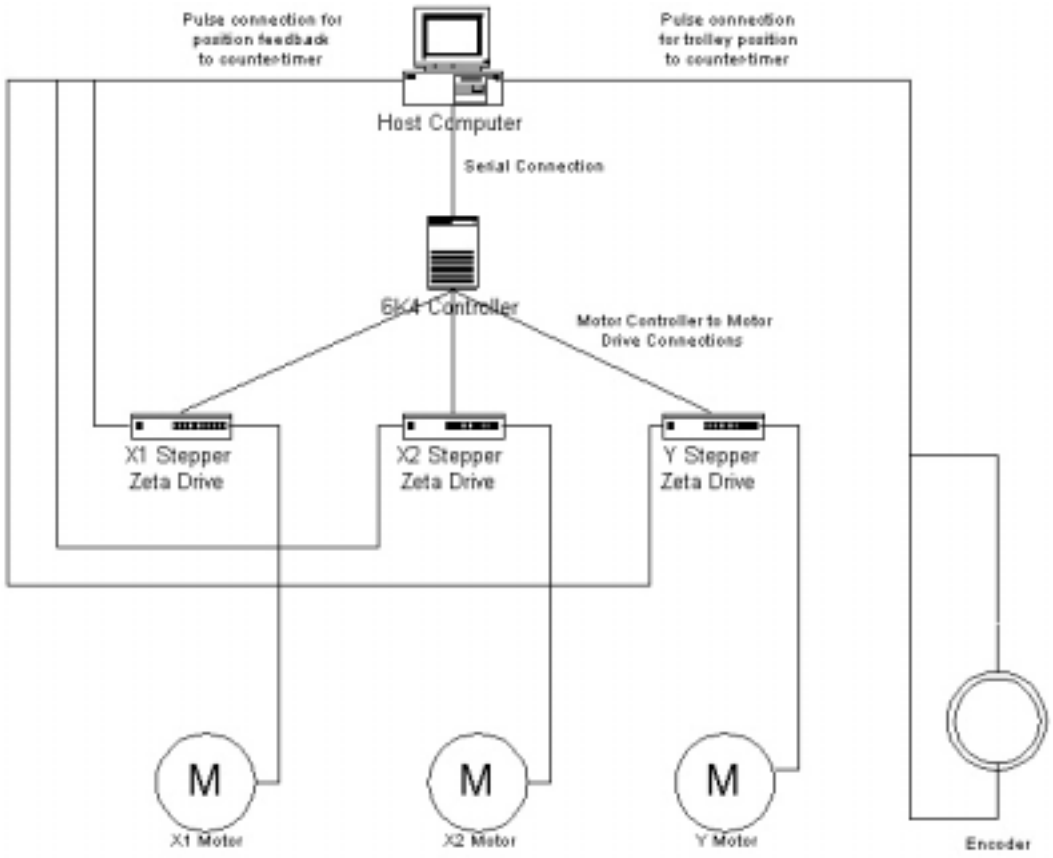

Figure 6.2. Block Diagram of RONDE Control System

Motor control for the RONDE system is done via several commands that are sent to the 6K4 controller. Most of these commands are identical to the AT6400 model, but some commands are either changed or removed entirely. The SAFT/T-SAFT software, running on the host computer, sends the control commands through a Parker developed driver for the 6K4 controller. A function is called within the SAFT/T-SAFT software that links with the Parker driver, in order to send the commands through the serial link. The advantage of this system is that the Parker driver allows multiple connections to it, which allows easier debugging of the software. Commands that have been sent by the driver are readily visible during debugging, as well as the response from the controller. The 6K4 controller will then send signals to the motor drives to move the stepper motors.

Once the motors have been commanded to move, the software listens for motor pulses using a high-speed counter module that is used to synchronize the motor movement with data collection. This allows accurate sample timing and position information for each data set. This same counter module is used to link with an encoder that is tied to a wheel to measure the distance traveled by the crawler. Through the use of custom electronics, the encoder sends pulses on one channel if the crawler is moving forward, and along another channel if the crawler is moving backward. By subtracting one set of pulses from the other, the system can record how far the crawler has moved since it was last reset.

6.2 Tank Top Electronics

The tank top electronics will be located near the entrance riser to the tank annulus. Multi-conductor cables extend from the tank top electronics enclosure to the RONDE crawler and scanning bridge. Housed in the tank top enclosure are electronics for driving the magnetic wheel crawler, electronics for driving the scanning bridge mechanisms, and the ultrasonic pulser/receiver for inspection of the tank knuckle. Figure 6.3 shows the tank top enclosure and associated electronics. Section 7 of this document discusses the tank top electronics in greater detail.

Figure 6.3. Tank Top Electronics

6.3 RONDE Control Station

The RONDE control station provides the computing hardware necessary to perform the data acquisition and data analysis.

The control station consists of two major components:

- Data acquisition station
- Data analysis station

Figure 6.4 shows the two computing stations. The dual monitors are used for data analysis.

Figure 6.4. Data Acquisition and Data Analysis Workstations

7 RONDE Electronics

The electronics design was based on a previous design of a SAFT/T-SAFT system developed by the NRC. Much of the electronics was specified as a requirement to be compatible with the old SAFT/T-SAFT software that was being implemented. Further narrowing of the electronics was specified to be the natural progression of industry standard upgrades for the existing equipment to the latest designs while still being compatible with the existing software with minimal changes. As a result the following hardware was pre-specified.

- Compumotor controller AT6400 16 bit ISA slot
  Later to be upgraded to Compumotor 6K4 RS-232 serial port controller
- National Instruments PC TIO-10 counter/timer 16 bit ISA slot
  Later to be upgraded to National Instruments 32 bit PCI slot PCI-6602
- Tektronix – Gage Compuscope 12 bit 100 Mega sample per second digitizer - PCI (dual slot)
- Ritec ultrasonic square wave pulser SP-801
- Ritec broadband receiver BR-640
- Ritec diplexer RDX-2
- Ritec high impedance pre-amplifier PAT-0.1-25
- Ritec high power attenuator RA-30
- Gulf X-ray Services crawler and MC controller

The data acquisition card on this new system was slightly different from the one on the old existing SAFT system, being a newer version of the same model. Because of this, it was necessary to use updated driver files to communicate with the card.

The earlier SAFT work used an A-scan acquisition length of 4,000 points or fewer. This was not adequate for the long path lengths involved in the knuckle inspection. Several program modules had to be revised to allow acquisition and display of longer A-scans.

The previous NRC systems were designed with Compumotor LN Series (Low Noise Analog) motor drivers. They are no longer manufactured and have been replaced with Zeta (Switcher) motor drives by Compumotor, which are specified as a lower noise driver according to Compumotor specifications.

On the previous NRC system, Compumotor Model S57-51 motors were used. The OS21B-SNL10 was chosen as a replacement because they are the same size, weight, and bolt pattern, but have 82 oz. in.^{2} and 0.660 inertia rather than 65 oz. in.^{2} and 0.546 inertia.

An existing system control printed circuit board (PCB) designed at PNNL was used. It has inputs to receive motor driver pulses and routes them into the counter/timer for on-the-fly data acquisition. It also has inputs to decode quadrature encoders and supplies that information to the counter timer for positional data to control scanners via a National

Instruments counter/timer card. The 16-bit ISA counter/timer resides in an ISA buss computer slot. The counter/timer (in computer) ribbon cable that hooks up to the PNNL PCB (in rack mount box) can be no longer than 1 meter as specified by National Instruments. Therefore a remote computer system was required for data acquisition at the tank entry point. Also, the Ritec Ultrasonics system and digitizer should remain as close to the data acquisition transducers as possible, further specifying the need for a tank top computer.

Cyber Research specializes in thin line rack mount computer systems. The Model LBJ 6P 2RU was chosen based on the slot requirements of the computer circuit boards needed for the controller system. It stands only 3.5" high in the rack. Also added was an HP CD writer 9600 series CDR for software installation and backup capability. The computer specifications are as follows:

- Cyber Research MicroRack Model LBJ 6P: 2RU
- One 20 gig EIDE ATA-66 (space for 2 internal 3.5" drives)
- One 3.5" floppy
- 19" x 21" x 3.5" high - 23 pounds empty
- 2 – 42 CFM ball bearing fans
- HP CD-writer 9600si Internal SCSI 12X/8X/32X CD writer
- Keyboard & Microsoft mouse
- System upgraded to 350 watt power supply
- Windows NT 2000 installed and complete system checkout at factory
- 2 full length empty PCI slots / 1 full length PICMG CPU slot / 2 full length empty ISA slots

  Slot PCI 1 = PCI-6602 Counter/Timer
  Slot PCI 2 = Gage 100 Megahertz Flash Card
  Slot ISA 3 = ISA Counter/Timer
  Slot ISA 4 = AT6400 Motor Controller
  Slot ISA 5 = Empty (overhang from the Gage double slot card)
  Slot PCI/ISA 6 = CPU card

- CPU = CPCS-COP-866
- 866 MHz Pentium III Coppermine
- 133 MHz front-buss with 512 Megs RAM
- VGA 4Meg on board video ram i810e chipset (uses up to 4 Megs of shared memory)
- Dual Intel 82559 Ethernet/LAN ports

- Dual EIDE ATA-66 ports
- Dual channel SYMBIOS 53C1010 Ultra SCSI controller (supports 30 devices)
- Dual USB ports
- Dual RS-232 serial ports
- AC97 stereo sound controller built into Intel i810e chipset (mic in, line in, cd in headers; 1/8" line out on the backplate)
- Hardware monitor can display card temperature, CPU fan speed, & supply voltage status
- 60°C max operating temperature

A 8.5" high rack mount box was chosen to house the controller, motor drivers, EMI/RFI kits, control PCB, power supplies, relay card, supply voltage meter, switches, connectors, cooling fan. On the front of the Scanner control box are the following switches:

- AC power
- 24 volt power to the electromagnets and solenoids (must be on {p} for normal use)

For the following switches if the switch is left in the down (device not activated) position, then computer program control is possible through the counter/timer digital outputs:

- bottom left electromagnet
- bottom right electromagnet
- both top electromagnets
- solenoids activation (momentary contact computer control always enabled)
- Pitch Catch/Pulse Echo

8 RONDE Imaging System

The Pacific Northwest National Laboratory (PNNL) has developed an ultrasonic examination system that utilizes the Synthetic Aperture Focusing Technique (SAFT) for application to the knuckle region of Double-shell waste tanks in the 200 East and 200 West areas of the Hanford site. This section addresses the focusing and visualization of ultrasonic inspection data using this SAFT imaging methodology.

The section describes the general requirements of the imaging subsystem, the assumptions used in developing the imaging sub-system, focusing features, visualization features, and testing performed.

8.1 General Requirements

The software requirements for the imaging sub-system were completed in FY01 and documented in project records. This software requirements document provided the general requirements for an imaging sub-system and then showed how these requirements were met. The requirements can be subdivided into characterization requirements, focusing requirements, and visualization requirements.

The characterization requirements apply to the entire RONDE inspection system. The system is designed to detect and size circumferential planar cracks, emanating from the inside surface of the tank. The detection sensitivity is designed to find these cracks with a minimum depth of 4.6 mm (0.18 in.). The crack sizing capability of the RONDE system has an error of less than $\pm$ 2.5 mm ($\pm$ 0.10 in.). The location of cracks is done to within a maximum error of $\pm$ 25.4 mm ($\pm$ 1.0 in.).

The focusing requirements include near real time performance and ease of use. Near real-time focusing performance is defined to be the same or less than the time required to acquire the data. The focusing software has a graphical user interface that makes the software easy to use.

The data visualization requirements include providing material coordinates for the responses in the images and a visual cue of the inside surface. Material coordinates for volume elements are given in X and Y values measured along the outside tank wall: X: distance from weld center in inches; Y: distance from known feature on tank wall in inches; Z: distance from outside surface of the tank wall in inches, measured perpendicular to the tangent at the X, Y location.

8.2 Assumptions

The imaging software was tested on existing data files in the development stage and those test results are reported in this section. Test results from the new RONDE mockups are reported in Section 9 of this document. The imaging software was tested on raw and

focused files that were collected in PNNL's preliminary testing stage [Pardini 2000] and are discussed in sections 8.3 and 8.4. The focusing code takes as its input, a raw data file in the SAFT-99 format. The output is a processed data file, in the SAFT-2001 data format. These processed files may be viewed with the existing code or the viewing code to be developed as part of the data visualization portion of this project.

Pulse echo line SAFT is used for detection. The modality is 3.5 MHz vertically polarized 70 degree refracted angle shear waves. Tandem line SAFT is used for sizing. The pulse-echo transducers are used in the tandem (sizing) test, 3.5 MHz vertically polarized 70 degree refracted angle shear waves.

The existing data from the flat plate trials were adequate for testing proper operation of the focusing code. The inspections of the curved knuckle generated hyperbolic time of flight shapes. This was also the case for the flat plate data. The testing on the new mockups resolved curvature issues and enhancements were specified after the testing on the new mockups.

The inspected volume (the knuckle) is a simply curved plate of uniform thickness. In particular the inside and outside surfaces are concentric quarter-circles. The secondary curvature of the cylindrical tank can be ignored. The front and back surfaces are parallel. The plate is composed of one to three sections, each of which is either flat or has a uniform circular curvature of a known radius.

8.3 Focusing System Features

The image focusing software is a program that runs on the analysis computer. The data collection occurs first and operates independently of the data analysis. The focusing code takes as its input, the raw data file. The file is SAFT processed and the results stored on disk as an output processed data file. It is the processed data file that is viewed for detection and sizing information.

Acquisition is performed by a modified version of the SAFT code. This is the same version that was used in the phase 1 tests. The inspection data, generated by the RONDE system, is 16-bit. Data acquisition is performed on the first computer in a two-computer system. Data analysis is performed on the second computer of a two-computer system.

8.3.1 Development Framework

The focusing code uses a previously established structure for adding project specific algorithms to PNNL's SAFT-UT imaging system. Table 8.1 shows the portion of this structure that is useful to RONDE with the C++ class names for the existing code. The code is written in C++ with the Microsoft Visual C++ version 6.0 compiler and uses the Microsoft Foundation Class (MFC) Library with MFC extension dynamic link libraries (DLLs) for modular programming.

Tables 8.1-8.3 show the existing 8-bit and 16-bit versions of the most fully developed and tested focusing code. New sixteen-bit versions of the focusing code have been developed for RONDE to meet project requirements for speed and ease of use.

Table 8.1 shows the C++ classes that own and control the unfocused inspection data. Inspection data is held in separate classes depending on the type of focusing that is relevant to that data: normal beam, angle beam, and tandem SAFT. These RF (unfocused) data classes also contain the controls that permit the user to change the default values that the inspection data specifies. After the user adjusts the focusing controls the RF data classes will respond to the *start focusing* command by creating instances of the relevant focusing objects. The focusing code can retrieve the control values from and report performance to the RF data classes.

Table 8.1. RF Data Classes and the Controls

Mode	RF data class	Focusing control classes	Algorithm control classes
Normal beam	CRfDataDoc	CFocusingControlFrame CFocusingControlPropSheet CFocusingStartPage CFocusingPerformancePage CFocusingSubVolumePage CFocusingBeamPage CFocusingEnvDetectPage CFocusingSkipPage CFocusingLenSamplingPage CFocusingNormalizePage CFocusThicknessPage	CAlgorithmControlFrame CAlgorithmControlPropSheet CAlgorithmSelectionPage CAlgorithmThreadingPage
Angle beam	CRfAngledDataDoc		
Tandem	CRfTandemDataDoc		

Tables 8.2 and 8.3 contain the C++ classes for focusing pulse echo angle beam data and tandem SAFT data. The focused data is owned by the CFocusDoc class and it creates the controls for viewing and calibrating the focused data. After the controls are created, CFocusDoc selects the approximation to apply to the inspection data: 3D SAFT, line SAFT, etc. If 3D SAFT was chosen, then a C3dSaft object is created. If line SAFT was chosen, then CLineSaft is created. C3dSaft creates and uses separate objects for 8-bit and 16-bit inspection data. CLineSaft was implemented for use on RONDE and a 16-bit version of the code

Table 8.2. Angle Beam SAFT Algorithm Classes

Algorithm	*Approximation*	Release	*Status*
By element CAngleFocusDoc	3D SAFT CAngle3dSaft	Beta CAngle3dSaft8bit CAngle3dSaft16bit	Pre-existing code
	Line SAFT CAngleLineSaft	Cangle2dSaft16bit	Developed for RONDE

Table 8.3. Tandem SAFT Algorithm Classes

Algorithm	*Approximation*	*Release*	*Status*
By element CTandemFocusDoc	3D SAFT CTandem3dSaft	CTandem3dSaft8bit	Pre-existing code
	Line SAFT CTandemLineSaft	Ctandem2dSaft16bit	Developed for RONDE

8.3.2 Pulse Echo Line SAFT

The focusing code is written to process a single channel and a single line of pulse echo SAFT data. The line SAFT system focuses individual data scans or lines of data. These processed data lines are then viewed and examined for indication/flaw detection. The data may be viewed as a single line, a B-scan, or a composite of selected data lines, a composite B-scan. Length sizing information in the circumferential direction is obtained by viewing this pulse echo data. The cracks are assumed to be circumferential. It is also assumed that the data is acquired with the SAFT scanning axis in a direction perpendicular to the tank circumference and the SAFT index axis is parallel to the tank circumference.

8.3.2.1 Focusing beam settings

Both the beam entry diameter in inches and the focusing aperture angle in degrees must be specified. The beam entry diameter is typically half of the contact transducer diameter and the SAFT aperture angle is typically optimal at the probe's lateral resolution [Busse 1984]. The line SAFT code was tested for a beam entry diameter of 7.6 mm (0.30 in.) and an aperture angle from two to twelve degrees on the phase one data.

8.3.2.2 Focusing skip settings

The current skip options are implemented to increase processing speed by not processing or skipping low-amplitude data points. Both the no skip and zero on skip at a –20 dB threshold options are implemented and tested.

8.3.2.3 Focusing envelope detection settings

The SAFT processed data is envelope detected to generate a rectified and smoothed output data file. The window length for this detection is generally half a wavelength and was tested for that length in the line SAFT code.

8.3.2.4 Focusing normalization settings

The SAFT processing currently normalizes the data to the sum. Specifically, the number of sums in the aperture normalizes each processed data point. This was implemented and tested.

8.3.2.5 Pulse echo line SAFT test results

A 16-bit data representation was implemented since the data acquisition hardware contains a twelve-bit analog-to-digital converter for increased dynamic range.

Table 8.4 lists the test files by name and acquisition parameters. Data obtained from a reference 25.4 mm (1 in.) thick flat plate are listed first and then the data obtained from the tank mockup is listed. Tandem data will be discussed in Section 8.3 but is also listed in this table.

Table 8.4. Listing of Existing DST SAFT Data Acquired in FY 00

Listing of Existing DST SAFT Data, Acquired in 2000																	
File Name Flat Plate	X Start (inch)	X Step (inch)	X Step (inch)	Num. X	Y Start (inch)	Y Step (inch)	Y Step (inch)	Num. Y	Y Path Start (inch)	Path Stop (inch)	Path Step (inch)	Z Start (inch)	Z Stop (inch)	Z Step (inch)	PtsPerScan	Max. Angle Processed (degrees)
1_2V_70S_3_5MHz_small_sawcut.rf [1]	0	3.50	0.015	233	0	3.00	0.015	200	2.000	5.992	0.0025	0.684	1.912	0.0089	1414	6
3_2V_70S_3_5MHz_small_sawcut.rf [2]	0	3.00	0.015	200	0	3.00	0.015	200	6.001	11.400	0.0025	2.380	3.699	0.0089	1771	2
5_2V_70S_3_5MHZ_small_sawcut.rf [3]	0	6.00	0.015	333	0	3.00	0.015	200	11.100	17.999	0.0025	3.796	6.156	0.0089	2716	2
70S_3_5MHz_large_sawcut_Exit.rf [4]	0	6.00	0.050	120	0	4.00	0.050	80	35.500	48.500	0.0025	12.142	16.582	0.0089	3937	2
70S_3_5MHz_small_sawcut_fix4.rf [5]	0	6.00	0.050	120	0	4.00	0.050	80	35.500	48.500	0.0025	12.142	16.582	0.0089	3937	2
H20_70S_3_5MHz_big_sawcut.rf [6]	0	6.00	0.020	300	0	0.40	0.020	20	35.500	48.500	0.0025	12.142	16.582	0.0089	3937	2
H20_70S_3_5MHz_small_sawcut.rf [7]	0	6.00	0.020	300	0	0.40	0.020	20	35.500	48.500	0.0025	12.142	16.582	0.0089	3937	2
H20_70S_3_5MHz_Multi_big.rf [8]	0	6.00	0.050	120	0	6.00	0.050	120	40.000	50.160	0.0025	13.681	17.156	0.0089	4000	2
H20_70S_3_5MHz_Multi.rf [9]	0	6.00	0.050	120	0	0.50	0.050	10	39.999	50.160	0.0025	13.681	17.156	0.0089	4000	2
H20_70S_3_5MHz_1_2V.rf [10]	0	3.50	0.050	70	0	0.50	0.050	10	1.001	5.997	0.0025	0.342	2.061	0.0089	1967	12
H20_70S_3_5MHz_1V.rf [11]	0	3.50	0.050	70	0	0.50	0.050	10	4.000	8.999	0.0025	1.368	3.078	0.0089	1968	12
H20_70S_3_5MHz_3_2V.rf [12]	0	3.50	0.050	70	0	0.50	0.050	10	7.000	11.499	0.0025	2.394	3.903	0.0089	1771	12
70S_3_5MHz_SMALL_SAWCUT_Bot_WELD.RF [13]	0	6.00	0.050	100	0	4.00	0.050	80	30.500	40.650	0.0025	10.430	13.910	0.0089	3089	2
Knuckle Mockup																
70S_3_5MHz_mockup_sawcut_24in_from_end.rf [14]	0	6.00	0.050	120	0	8.00	0.050	160	14.001	24.161	0.0025	4.790	8.280	0.0089	4000	2
70S_3_5MHz_mockup_sawcut_4in_from_end.rf [15]	0	6.00	0.050	120	0	4.00	0.050	80	34.000	42.899	0.0025	11.630	14.670	0.0089	3583	2
70S_3_5MHz_Mock_up_end.rf [16]	0	6.00	0.050	120	0	4.00	0.050	80	39.001	47.000	0.0025	12.997	16.075	0.0089	3543	2
Tandem Data																
TandemOnMockup.rf [17]	0	3.00	0.050	80	0	5.00	0.050	100	33.052	41.001	0.0025	11.288	14.023	0.0089	3149	12
Screwstick.dat* [18] (6.7" thick block)	-10	0.00	0.040	250	0	4.00	0.080	50	5.500	13.500	0.0098	3.883	9.531	0.0089	813	
Screwstick.dat* [19] (6.7" thick block)	-10	0.00	0.040	250	0	4.00	0.080	50	5.500	13.500	0.0098	3.883	9.531	0.0089	813	
Screwstick.dat* [20] (6.7" thick block)	-10	0.00	0.040	250	0	4.00	0.080	50	5.500	13.500	0.0098	3.883	9.531	0.0089	813	
* This file was acquired from another project																

A variety of data file sizes are included as shown by the x, y, and z starts, stops and step sizes. The path start variations were used in testing the SAFT focusing at different depths in the material.

Each file was acquired with a 3.5 MHz, 70-degree shear mode transducer. A 4000-point limit to the number of points per A-scan limits the part path to approximately 254 mm (10 in.) and the depth inspected (Z) to approximately 86 mm (3.4 in.) at the 70-degree inspection angle. However the path start varies in this data from 51 to 1016 mm (2 to 40 in.) and provided a good test range for the focusing code at different depths.

The right column in the table shows the largest aperture angle that was used to process a given file. The line SAFT code was designed and tested to process at an angle of up to twelve degrees.

Table 8.4 also associates a file number, in square brackets with each of the file names. Files 10-12 contain end-of plate data acquired at 1/2, 1, and 3/2 V part paths. The files are small and each have 1.27 mm (0.050 in.) steps in the x and y direction, scan and increment direction respectively. The number of points per A-scan is less than 2000. This is good data for initially testing the focusing code on smaller part paths, larger aperture angles (up to twelve degrees) and in a timely manner since the processing time was small.

The next group of files to test is files 1-3. This data was acquired from the 5.1 mm (0.20 in.) deep saw cut in the flat plate. Data was obtained at ½, 3/2, and 5/2 V part paths. The step size in x and y is 0.381 mm (0.015 in.) and the part path is longer for the 5/2 V data. Testing on this data will confirm focusing on larger part paths and larger data files with aperture angles up to twelve degrees.

The third testing phase was on file 9. This data has the largest part path of 1016 mm to 1274 mm (40.00 in. to 50.16 in.) and the maximum number of points per A-scan at 4000. The step sizes are 1.27 mm (0.050 in.) and there are only 10 scans in the y direction so the file is approximately 5 Mbytes in size. This was a good smaller file for testing the focusing at large part paths and aperture angles up to twelve degrees.

The fourth set of data for testing is from files 4 and 5. This data was acquired on the large saw cut that is 12.7 mm (0.50 in.) deep. The step size in x and y is 1.27 mm (0.050 in.). Both the part path and number of points per A-scans are large. This is good data for testing the focusing at large part paths, with a large aperture angle on a second machined flaw with known dimensions.

The data acquired from the tank mockup is represented in files 14-16. The x and y step sizes are 1.27 mm (0.050 in.) and the part paths are not outside the range that will already be tested in the flat plate data above. File 14 is significant in that it is data from a flaw in the knuckle to flat plate transition. A 4.6 mm (0.18 in.) deep saw cut is in this location. Test file 15 was obtained from a 2 mm (0.080 in.) deep saw cut in the mockup, 102 mm (4.0 in.) from the end of the mockup plate. The saw cut is in the bottom of the tank, in the flat region outside of the knuckle. An end of plate data file, number 16, also was acquired.

Table 8.5 shows the files that were used in testing the line SAFT code and also the parameters that were tested with each file.

Table 8.5. Parameters to Test in the Line SAFT Focusing

Listing of Existing DST SAFT Data, Acquired in 2000 and Parameters to Test in the Line SAFT Focusing							
File Name and Number	Beam		Envelope	Normalize	Skip		
	Aperture Angle	Beam Entry Diameter	Samples	To Sum	No Skip	Zero on Skip	No. of Tests
Flat Plate	(degree)	(inch)				(-20 dB)	
H20_70S_3_5Mhz_1_2V.rf [10]	12	0.3	4	yes	yes	yes	2
H20_70S_3_5MHz_1V.rf [11]	12	0.3	4, 8	yes			2
H20_70S_3_5MHz_3_2V.rf [12]	12	0.3	4	yes			1
1_2V_70S_3_5MHz_small_sawcut.rf [1]	6, 12	0.3	4	yes	yes		2
3_2V_70S_3_5MHz_small_sawcut.rf [2]	2, 6, 12	0.3	4	yes	yes		3
5_2V_70S_3_5MHZ_small_sawcut.rf [3]	2, 6, 12	0.3	4	yes	yes		3
H20_70S_3_5MHz_Multi.rf [9]	2, 6, 12	0.3	4	yes	yes		3
	12					yes	1
70S_3_5MHz_large_sawcut_6x4.rf [4]	2, 12	0.3	4	yes		yes	2
70S_3_5MHz_small_sawcut_6x4.rf [5]	2, 12	0.3	4	yes		yes	2
H20_70S_3_5MHz_big_sawcut.rf [6]	2, 12	0.3	4	yes		yes	2
H20_70S_3_5MHz_small_sawcut.rf [7]	2, 12	0.3	4	yes		yes	2
H20_70S_3_5MHz_Multi_big.rf [8]							0
70S_3_5MHz_SMALL_SAWCUT_8x4_WELD.RF [13]							0
Knuckle Mockup							
70S_3_5MHz_mockup_sawcut_24in_from_end.rf [14]	2, 6, 12	0.3	4	yes		yes	3
70S_3_5MHz_mockup_sawcut_4in_from_end.rf [15]	2, 6, 12	0.3	4	yes		yes	3
70S_3_5MHz_Mock_up_end.rf [16]	2, 6, 12	0.3	4	yes		yes	3

8.3.3 Tandem Line SAFT

After a flaw/indication has been detected with the pulse echo line SAFT inspection, the area of interest is scanned in the tandem mode for flaw depth sizing. Separate transmit and receive transducers are scanned across a line perpendicular to the flaw. The receive data is recorded and T-SAFT processed to produce flaw depth information from that line of data. Several lines of tandem data are acquired to size the deepest portion of the flaw. The tandem line SAFT focusing code was modified from the volumetric T-SAFT code. Note that the tandem focusing works best on vertically oriented planar defects [Hall 1988].

8.3.3.1 Focusing beam settings

Both the beam entry diameter in inches and the focusing aperture angle in degrees must be specified. The beam entry diameter is typically half of the contact transducer diameter and the SAFT aperture angle is typically optimal at the probe's lateral resolution [Busse 1984]. The line SAFT code was tested for a beam entry diameter of 7.6 mm (0.3 in.) and an aperture angle from two to twelve degrees on the phase one data.

8.3.3.2 Focusing skip settings

The current skip options are implemented to increase processing speed by not processing or skipping low-amplitude data points. Both the no skip and zero on skip at a –20 dB threshold options were implemented and tested.

8.3.3.3 Focusing envelop detection settings

The SAFT processed files will be envelope detected to generate a rectified and smoothed file. The window length for this detection is generally half a wavelength and that length was used in tests of the line tandem SAFT code.

8.3.3.4 Focusing normalization settings

The SAFT processing currently normalizes the data to the sum. Specifically, the number of sums in the aperture normalizes each processed data point. This was implemented and tested.

8.3.3.5 Focusing thickness settings

The part thickness must be known for T-SAFT processing. An allowable error range has not been defined but the given four tests files will be evaluated for T-SAFT focusing over a range of $\pm$5% of the known part thickness.

8.3.3.6 Line tandem test results

The tandem data files that will be used in testing the line T-SAFT code are listed earlier in Table 8.4.

A tandem data file was available from the mockup. It was acquired on the 4.6 mm (0.18 in.) deep saw cut, 102 mm (4.0 in.) from the end of the plate. Data obtained on another project is included here as files 18-19 to allow additional testing of the line T-SAFT code. This data is from notches 10, 30, and 50 mm (0.39, 1.18, and 1.97 in.) deep in a 170 mm (6.7in.) thick block fabricated for another project.

The testing matrix for the tandem code is listed in Table 8.6.

Table 8.6. Line T-SAFT Focusing

Listing of Data to Test the Line T-SAFT Focusing								
File Name and Number	Beam		Envelope	Normalize	Skip		Thickness	
	Aperture Angle (degree)	Beam Entry Diameter (inch)	Samples	To Sum	No Skip	Zero on Skip (-20 dB)		No. of Tests
TandemOnMockup.rf [17]	12	0.30	4	yes	yes	yes		2
							"±5%"	2
Flat Plate								
1cmnotch.dat [18] (6.7" thick block)	12	0.125	2, 3, 4	yes	yes			3
							"±5%"	2
3cmnotch.dat [19] (6.7" thick block)	12	0.125	3	yes	yes			1
							"±5%"	2
5cmnotch.dat [20] (6.7" thick block)	12	0.125	3	yes	yes			1
							"±5%"	2

8.3.4 Performance

Near real-time performance of the focusing code was achieved. A comparison of an estimate of the processing time and the scan time for the test files is listed in Table 7.7. The nominal processing rate of 10 mega sums per second and a scan rate of 25.4 mm (1 in.) per second were measured. Ideally the process time is equal to or less than the time to acquire the data. The processing times vary as the number of steps in the x direction or scan line vary and are also dependant on the number of points in an A-scan. From the data in Table 8.7, the worst performance is shown in files 6 and 7. These files have a reasonable step size of .51 mm (0.020 in.) (half a wavelength) and 4000 points per A-scan. The processing time is estimated to be six times longer than the acquisition time.

Table 8.7. Comparison of Estimated Processing and Scan Times

Comparison of Estimated Processing and Scan Times										
File Name and Number	X Start (inch)	X Stop (inch)	X Step (inch)	Num. X	Path Start (inch)	Path Stop (inch)	Path Step (inch)	Pts/Ascan	Estimate of Time to Process[1] (seconds)	Estimate of Scan Time[2] (seconds)
Flat Plate										
1_2V_70S_3_5MHz_small_sawcut.rf [1]	0	3.50	0.015	233	2.000	5.592	0.0025	1414	7.7	3.5
3_2V_70S_3_5MHz_small_sawcut.rf [2]	0	3.99	0.015	266	6.901	11.400	0.0025	1771	12.5	4.0
5_2V_70S_3_5MHZ_small_sawcut.rf [3]	0	5.00	0.015	333	11.100	17.999	0.0025	2716	30.1	5.0
70S_3_5MHz_large_sawcut_6x4.rf [4]	0	6.00	0.050	120	35.500	45.500	0.0026	3937	5.7	6.0
70S_3_5MHz_small_sawcut_6x4.rf [5]	0	6.00	0.050	120	35.500	45.500	0.0025	3937	5.7	6.0
H20_70S_3_5MHz_big_sawcut.rf [6]	0	6.00	0.020	300	35.500	45.500	0.0025	3937	35.4	6.0
H20_70S_3_5MHz_small_sawcut.rf [7]	0	6.00	0.020	300	35.500	45.500	0.0025	3937	35.4	6.0
H20_70S_3_5MHz_Multi_big.rf [8]	0	6.00	0.050	120	40.000	50.160	0.0025	4000	5.8	6.0
H20_70S_3_5MHz_Multi.rf [9]	0	6.00	0.050	120	39.999	50.160	0.0025	4000	5.8	6.0
H20_70S_3_5Mhz_1_2V.rf [10]	0	3.50	0.050	70	1.001	5.997	0.0025	1967	1.0	3.5
H20_70S_3_5MHz_1V.rf [11]	0	3.50	0.050	70	4.000	8.999	0.0025	1968	1.0	3.5
H20_70S_3_5MHz_3_2V.rf [12]	0	3.50	0.050	70	7.000	11.498	0.0025	1771	0.9	3.5
70S_3_5MHz_SMALL_SAWCUT_8x4_WE	0	8.00	0.050	160	30.500	40.656	0.0025	3999	10.2	8.0
Knuckle Mockup										
70S_3_5MHz_mockup_sawcut_24in_from_	0	6.00	0.050	120	14.001	24.161	0.0025	4000	5.8	6.0
70S_3_5MHz_mockup_sawcut_4in_from_	0	6.00	0.050	120	34.000	42.898	0.0025	3503	5.0	6.0
70S_3_5MHz_Mock_up_end.rf [16]	0	6.00	0.050	120	36.001	47.000	0.0025	3643	5.1	6.0
Tandem Data										
TandemOnMockup.rf [17]	0	3.00	0.050	60	33.002	41.001	0.0025	3149	1.1	3.0
1cmnotch.dat [18] (6.7" thick block)	-10	0.00	0.040	250	5.500	13.900	0.0098	813	5.1	10.0
3cmnotch.dat [19] (6.7" thick block)	-10	0.00	0.040	250	5.500	13.900	0.0098	813	5.1	10.0
5cmnotch.dat [20] (6.7" thick block)	-10	0.00	0.040	250	5.500	13.900	0.0098	813	5.1	10.0
[1] based on a nominal 10 mega sums per second processing rate										
[2] based on a nominal 1 inch per second scan rate										

8.4 Visualization Features

This section contains a description of the visualization features that were designed and implemented for the data displays from the ultrasonic inspection of the DST knuckle region. The principal requirement for the visualization sub-task was to estimate the material coordinates for responses from ultrasonic reflectors. The approach was to provide a transformation from volume elements in the ultrasonic images to knuckle coordinates in inches from an established reference. This section also provides a description of the testing results for response location in the knuckle mockups.

8.4.1 Response Location Feature

A *response location* tool (Figure 8.1) for the tank wall and knuckle geometry was designed and implemented. The implementation includes a dialog box which, when the user clicks on any point in the data volume, will tell what the datum's material coordinates are. This tool operates on a SAFT-2000 ultrasonic data file (either

unprojected or projected). It displays the material depth and knuckle position (in inches and degrees) of a center-ray reflection at the cursor. The tool is available in a modified version of SAFT 2001.

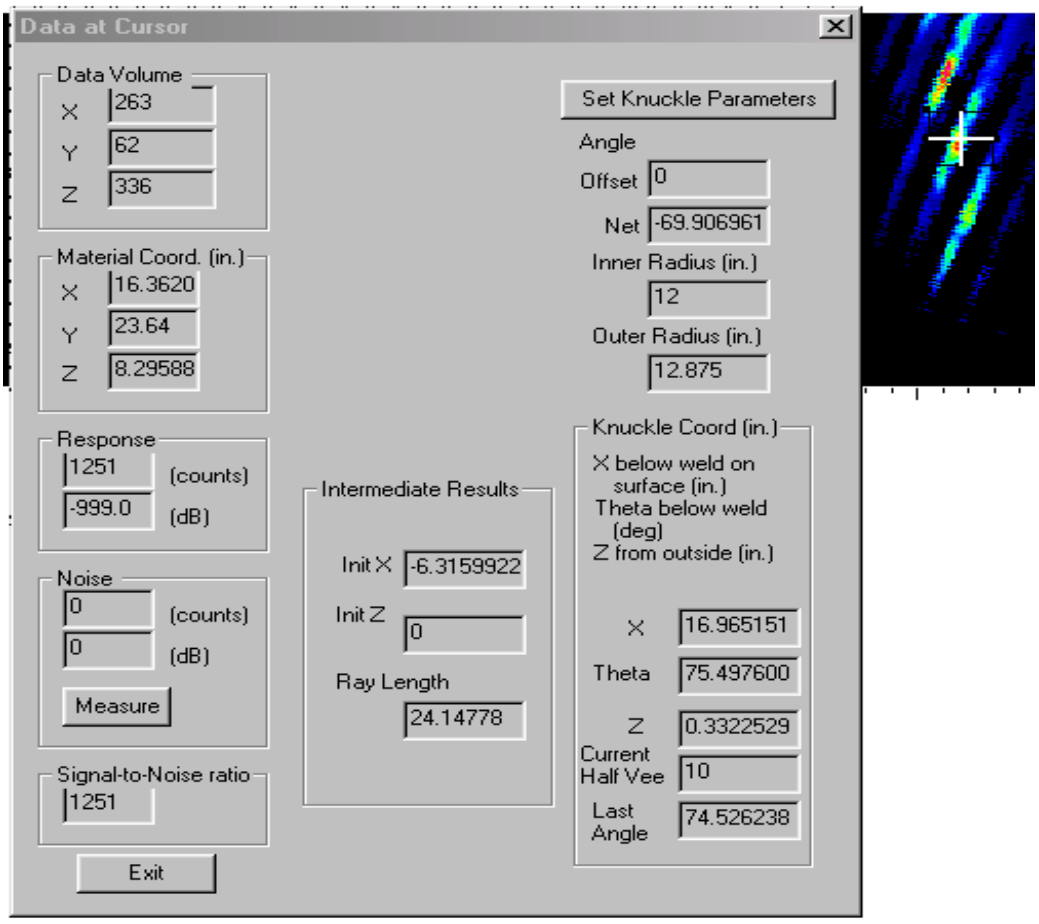

Figure 8.1. Response Location Display

The left-hand column of controls in the dialog box contains the standard SAFT response location display for flat components. The center column (Intermediate Results) is primarily for verifying the operation of the new response location display. It shows the X position at which the transducer was located, the depth Z at which the ray began, and the Ray Length as measured along the bounce path. The X coordinate is 0 at the start of the knuckle, negative in the vertical wall, and positive as measured with a flexible tape along the outside around the knuckle and under the tank. The initial Z should be 0. The ray length should equal the diagonal distance from the transducer to the cursor, which is calculated by subtracting Intermediate Init X from Material Coord. X and squaring the result; squaring the Material Coord. Z; adding these; and taking the square root.

The right-hand column contains the main operational parts of the tool. The button at the top is used to set the knuckle radius and an optional angle offset as shown in Figure 8.2.

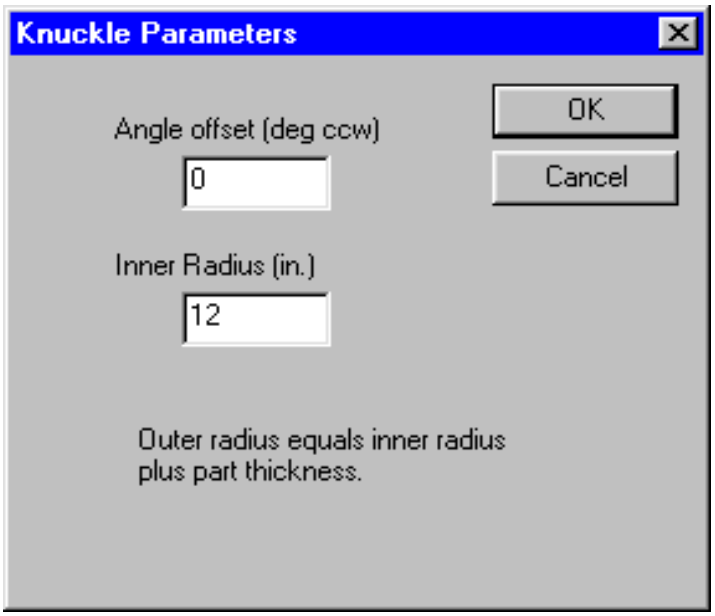

Figure 8.2. Knuckle Parameters Dialog Box

The angle offset allows the choice of a ray other than the central ray. For example, if the transducer has a 70 refracted angle (for historical reasons, this is entered as –70), and the angle offset is set to +5, the ray path for a 65-degree ray will be used for the calculations. The reason for providing this offset will be seen in Section 8.4.2, below. The inner radius defines the knuckle geometry. A value of 0 causes the calculations to be based on a flat-plate geometry. A value of (for example) 12 defines the radius of the inside surface of the knuckle as 305 mm (12 in.). The outer radius is, as noted in the dialog box, equal to the inner radius plus the part thickness (defined elsewhere in the SAFT code).

Continuing the description of Figure 8.1, the Angle Offset is the value set by the Knuckle Parameters, and the Net is the actual ray angle to be used (refracted angle plus offset angle). The Inner and Outer Radii are as described for Figure 8.2. The Knuckle Coordinates give the information about the cursor location. X is the distance from the beginning of the knuckle to the cursor, as measured along the outside surface of the tank (note that the "weld" is defined as the beginning of the knuckle). Theta is the angle between horizontal and the cursor location, as shown on a cross-section drawing of the knuckle. Z is the depth of the cursor from the outer surface, measured along the surface normal. Current Half Vee counts the number of ray segments, including the initial ray from the transducer. It is always one less than the number of reflections in the (one-way) path from the transducer to the cursor. Last Angle is the angle between the surface normal at the last reflection point and the last ray segment.

8.4.2 Testing Results for Response Location Feature

The tool was tested on indications in SAFT-processed flat-plate files and was found to perform as expected, correctly locating the indication (including all reflections) at front or back surface. The tool gives correct ray-tracing of the cursor for locations in the knuckle; however, location of indications is not demonstrated.

When the Inner Radius is set to 0 (Flat Plate case) the interpretation of the results is intuitive for an operator experienced in angle-beam inspection of plates. As the cursor is moved up and down over the multiple indications in the projected view, the Z value varies linearly from 0 to Part Thickness and back, while the Current Half Vee increments or decrements regularly by one. However, in an actual knuckle, the behavior is quite different. Because the transducer is positioned on the flat wall above the knuckle, the beam angle in the knuckle changes as the transducer is moved in the X direction. This means that the ray segments change in angle, and the Vee count can change dramatically over a short distance. In addition, the center ray does not always define the highest amplitude (Roberts et al., 2001), so the location of the indications does not always correspond to the center-ray analysis. Attempts to use the tool on SAFT-processed indications in the knuckle region were partially successful. Improvements will be made in follow-on work.

The implementing code is within the NormalViews project. Some code is in the previously existing module DataCursorDlg and the rest is in the new modules KnuckleBouncer and KnuckleSettingsNVDlg. Changes to the MaterialControl module, and further changes to DataCursorDlg, will be needed to integrate the knuckle ray tracer into the rest of the SAFT program without affecting its operation on non-knuckle geometries.

8.5 Terminology

Bounce: the reflection of the ray from a surface; the ½-V multiple.
Flaw: An unintentional discontinuity that has the potential to compromise the tank's integrity
Indication (of a flaw): The response or evidence of a flaw from the application of nondestructive evaluation. For ultrasonic testing, a coherent packet of ultrasonic energy that is characterized as originating from a flaw.
Transition: the change in angle from flat to curved region.
Transition zone: the region in which the sound moves from the wall into the knuckle. In a ray-tracing model, the bounce from flat to curved, for a given beam angle and transducer position.
V Path or **Vee Path**: Designation for the distance traveled by the sound wave from the transducer (on O.D. surface) to the first bounce (I.D. surface) and then back to the O.D. surface forming a V in the part.

9 FY01 Test Results

9.1 Flaw Detection

The SAFT system is operated in the pulse echo (P. E.) mode for defect detection. Ten percent deep notches were machined into mockup 3 at axial locations of minus 102 mm (4.0 in.) from the first knuckle weld and at positive 76, 249, 376, 521, and 965 mm (3.0, 9.8, 14.8, 20.5, and 38 in.). Note that second knuckle weld is located at 483 mm (19 in.) so the last two notches are past the second weld. All of these notches were detected. The farthest notch is 483 mm (19 in.) beyond the second knuckle weld and located in the floor of the tank. Figure 9.1 shows a C-Scan or plan view of the SAFT data of the second knuckle and the floor notch 483 mm (19 in.) away.

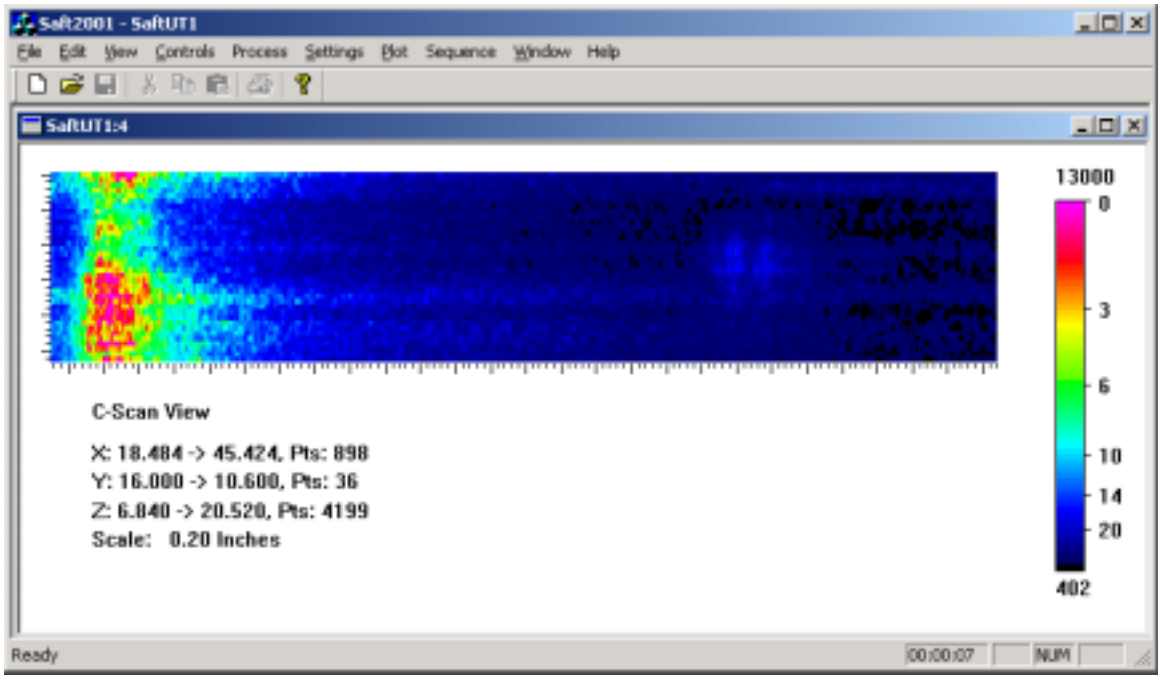

Figure 9.1. C-Scan or plan view of a P. E. image showing the second knuckle weld on the left and a ten percent through-wall deep notch 483 mm (19 in.) beyond the weld.

Figure 9.2 shows the floor notch after boxing it out of the first image for greater clarity. The notch is approximately 15 decibels lower in amplitude than the second weld.

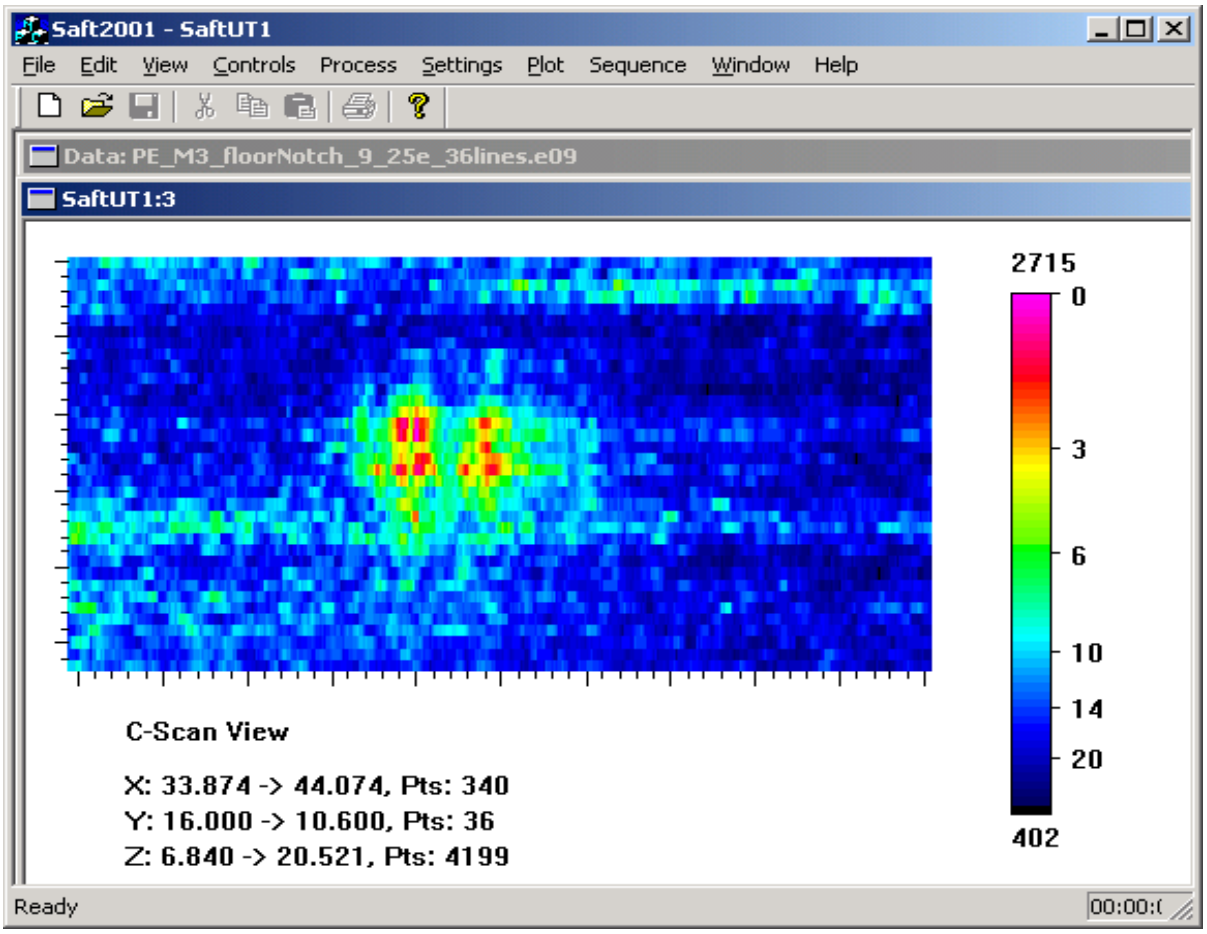

Figure 9.2. C-Scan view of the ten percent through-wall deep notch, extracted from the image in Figure 9.1. The full circumferential length of the notch, vertical direction in the Figure, was not imaged.

A series of saw cuts that varied in depth from ten to seventy percent through-wall were machined on the inside diameter (ID) in the second mockup. All of these defects were detected. Two outside diameter (OD) saw cuts at depths of twenty and forty percent through-wall were also machined in mockup two. These OD saw cuts were also detected. Figure 9.3 shows the C-Scan view of the two OD and nearest two ID saw cuts.

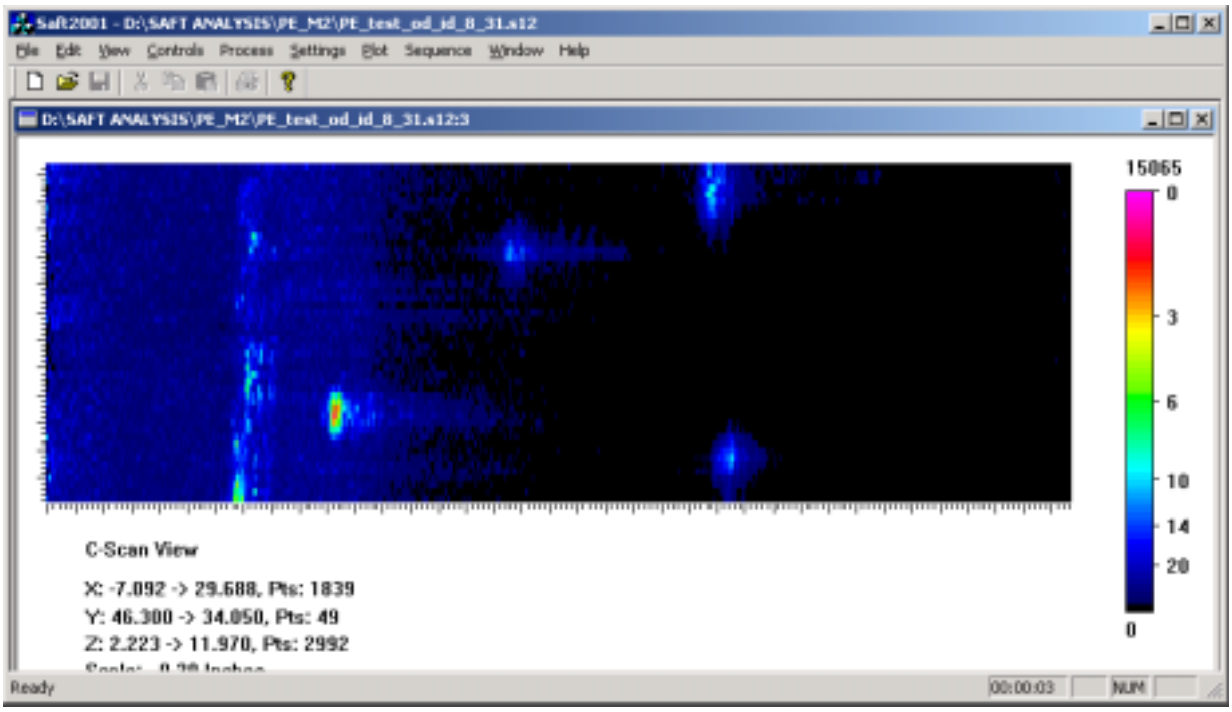

Figure 9.3. C-Scan view of the first knuckle weld and four saw cuts. Left to right are the weld, a 10 percent deep ID saw cut, a 20 percent deep OD saw cut, a 40 percent deep OD saw cut, and a 25 percent deep ID saw cut.

To detect both the second weld and the first weld in the same image, a higher gain setting was necessary than the gain setting used in the detection of the saw cuts in mockup 2. Figure 9.4 shows both the first and second knuckle welds from mockup 3 taken at a gain

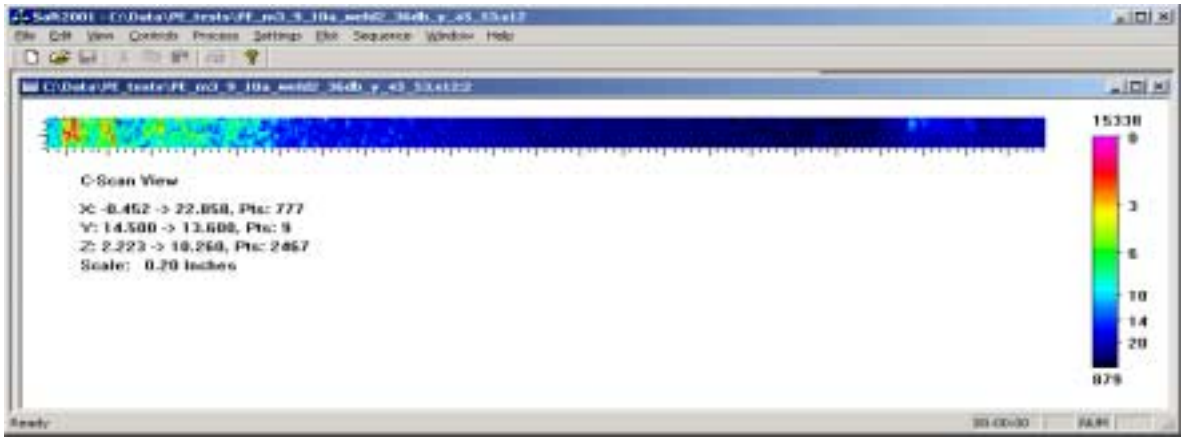

Figure 9.4. C-Scan view of both the first and second knuckle welds from mockup 3.

setting of 36 dB. The saw cut data was acquired with gain settings typically between zero and sixteen dB. Figure 9.5 shows the second weld after extraction with the box

function from the image in Figure 9.4. The second weld is approximately nine decibels lower in amplitude than the first weld in these SAFT processed images.

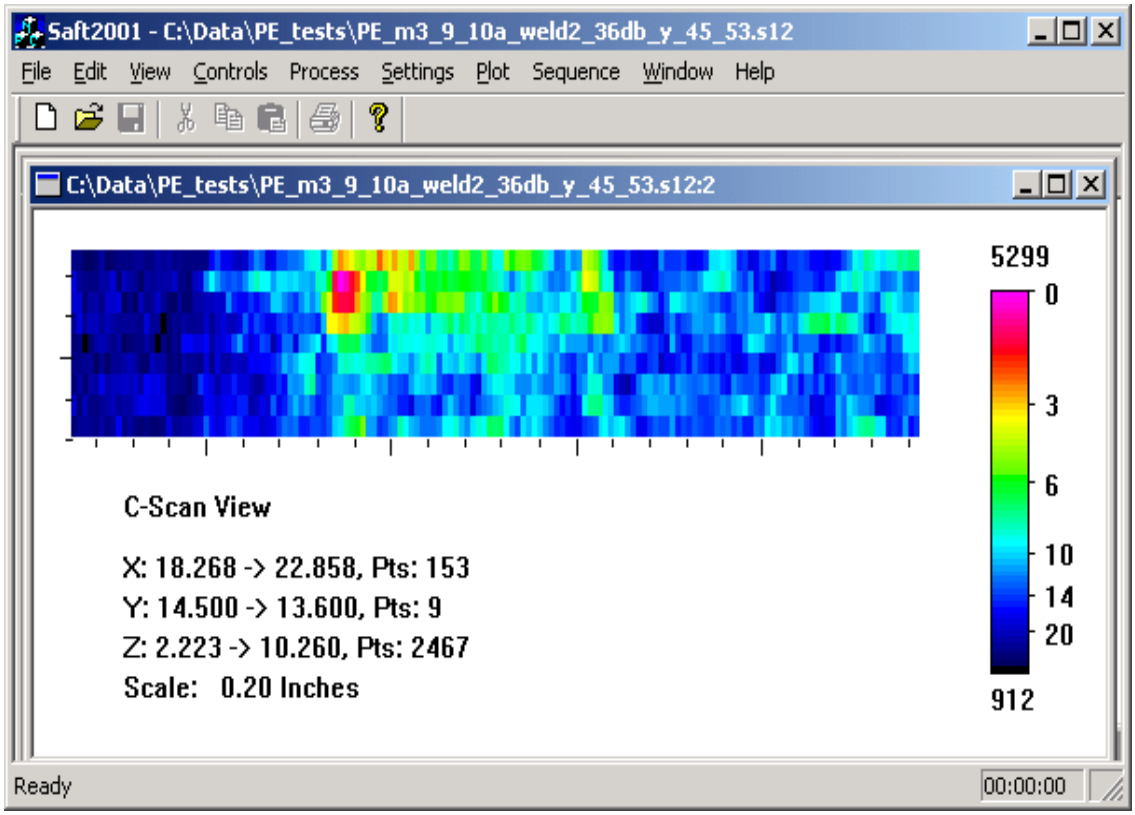

Figure 9.5. C-Scan view of the second knuckle weld, extracted from the image in Figure 9.4.

The pulse echo detection system was operated with a 127 to 152 mm (5 to 6 in.) sweep in the scanning or axial direction and a 305 mm (12 in.) circumferential path. Four lines of data were acquired per minute at a 5.1 mm (0.20 in.) increment between scan lines. The time required to collect a foot of detection data was fifteen minutes. SAFT processing time was nominally five minutes, depending on process settings. This scanning pattern insured that the direct beam of the transducer covered both the ID and OD surfaces of the knuckle region. The time window of the sampled data must also be appropriately set. Later testing showed that all of the saw cuts were detected by merely moving the transducer in a circumferential line. More testing should be done to verify these results but there is the potential to greatly increase the time spent in the detection mode of operation.

9.2 Flaw Sizing

Tandem SAFT or T-SAFT provides a means for sizing the depth or through-wall dimension of vertically oriented planar defects. A transmitting and receiving transducer are simultaneously scanned, in tandem, in the region of interest.

The peak response from the corner trap of a flaw is first located with pulse echo ultrasonic data. This is illustrated in Figure 9.6 where a single pulse-echo transducer is positioned to receive the strong corner response. For tandem data acquisition the two tandem transducers are positioned side by side at this peak response location. This location will produce a peak response in both the tandem and pulse-echo data. The transmit and receive transducers are moved 76 to 102 mm (3 to 4 in.) in opposite directions. The tandem data acquisition then begins by scanning the two transducers towards each other, up to the mid-point of the scan, and continuing away from each other, to the end of the scan line as shown in Figure 9.7. Next the pair of transducers returns to their start positions, are both incremented circumferentially, and start the next scan line. In this way tandem data can provide length as well as depth information.

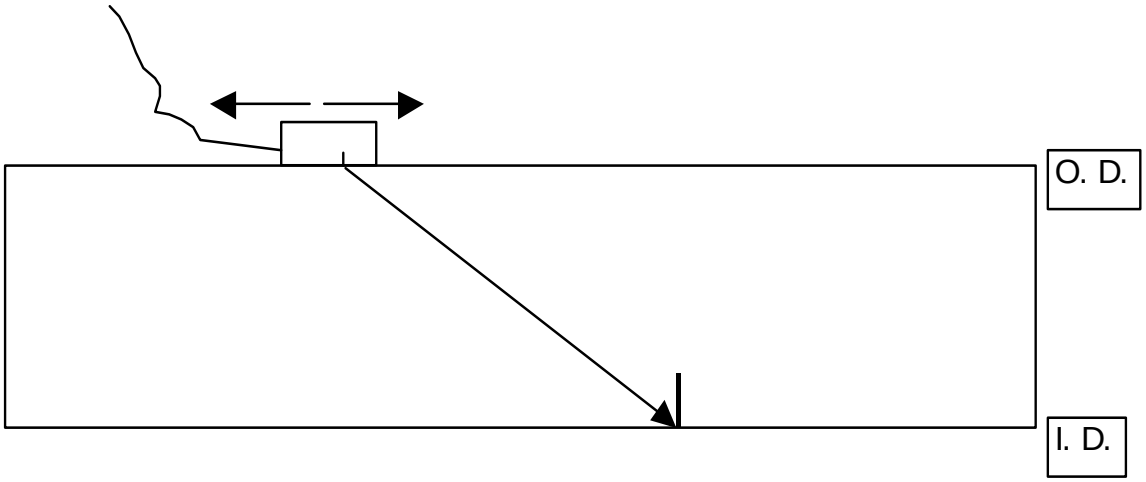

Figure 9.6. Side view of a transducer positioned to receive the strong corner trap signal from a flaw located on the inner diameter (ID) of the tank.

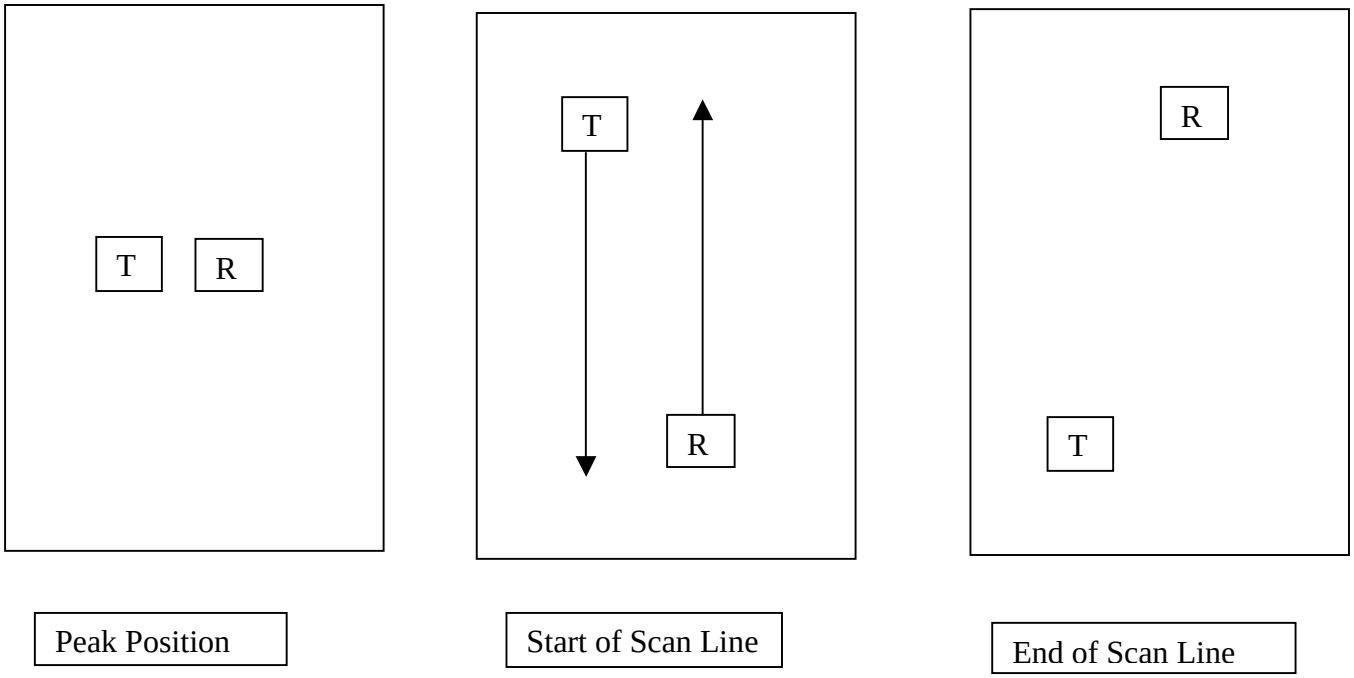

Figure 9.7. The T-SAFT setup and scanning motion is displayed. The left diagram shows the two transducers positioned to receive a strong corner trap signal from a defect. Both transducers are in position to start a scan line in the middle diagram. The position of the transducers at completion of a scan line is shown to the right.

To evaluate the T-SAFT sizing performance, a series of saw cuts were machined into the knuckle region of a tank mockup. These ten saw cuts varied from ten to seventy percent in through-wall depth. The location and size of these saw cuts are listed in Table 9.1.

Table 9.1. Saw cut Dimensions and Location in Mockup

Through Wall Depth (%)	True Depth mm (in.)	Axial Position mm (in.)	Starting Circumferential Position mm (in.)	Length mm (in.)
10	2.3 (0.092)	88.8 (3.5)	947.42 (37.3)	33.02 (1.3)
15	3.3 (0.13)	368.3 (14.5)	490.22 (19.3)	40.64 (1.6)
20	4.7 (0.185)	254.0 (10)	205.74 (8.1)	48.26 (1.9)
25	5.6 (0.219)	463.6 (18.25)	896.62 (35.3)	53.34 (2.1)
35	7.7 (0.304)	254.0 (10)	396.24 (15.6)	60.96 (2.4)
40	8.9 (0.35)	25.4 (1)	566.42 (22.3)	66.04 (2.6)
50	10.9 (0.431)	120.7 (4.75)	312.42 (12.3)	71.12 (2.8)
55	12.2 (0.482)	196.9 (7.75)	744.22 (29.3)	73.66 (2.9)
65	14.4 (0.569)	254.0 (10)	655.32 (25.8)	83.82 (3.3)
70	15.1 (0.595)	444.5 (17.5)	154.94 (6.1)	83.82 (3.3)

The knuckle region was inspected with pulse-echo ultrasound to first detect each of the saw cuts. Strong signals were received from each of the saw cuts and demonstrated the

excellent detection capability of the system on machined defects. As noted previously, the corner responses from the pulse-echo data for a particular defect determined the axial location for the tandem setup. Tandem data was acquired from each of the saw cut regions. Nine of the ten saw cuts were sized with T-SAFT. The results are shown in Table 9.2 and Figure 9.8. The error was calculated to be 1.2 mm (0.047 in.), well within the required 2.54 mm (0.1 in.).

Table 9.2. Tandem Depth Sizing Data

Through Wall Depth %	True Depth mm (in.)	Measured Depth mm (in.)	Difference	RMSE
10	2.3 (0.092)	3.81 (0.15)	-0.06	0.047
15	3.3 (0.130)	4.06 (0.16)	-0.03	
20	4.7 (0.185)	6.35 (0.25)	-0.07	
25	5.6 (0.219)	4.82 (0.19)	0.03	
35	7.7 (0.304)	6.09 (0.24)	0.06	
40	8.9 (0.350)	9.65 (0.38)	-0.03	
50	10.9 (0.431)	10.16 (0.40)	0.03	
55	12.2 (0.482)	12.19 (0.48)	0.00	
65	14.4 (0.569)	12.70 (0.50)	0.07	
70	15.1 (0.595)	Not Included (see page 83)		

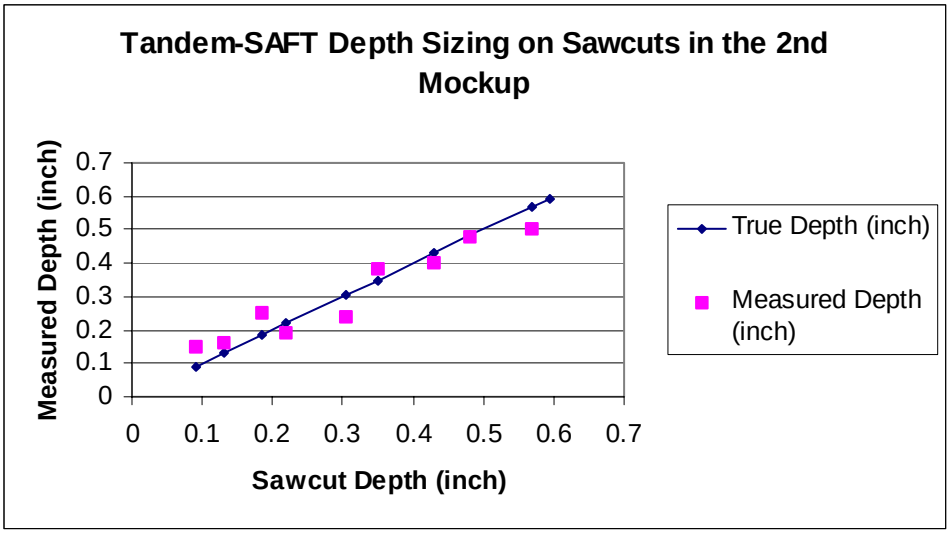

Figure 9.8. T-SAFT sizing results from saw cuts ranging in through-wall depth from ten to sixty-five percent.

Figure 9.9 shows a section of the mockup with the weld on the left and the transducer scanning left of the weld. A flaw is detected with ultrasound. The three possible views are show. First is the C-Scan or plan view. Then there are two B-Scan views, the side and end views. Both the C and B-Scan end view give circumferential length information. Depth information is determined from both B-Scan views. All three views are useful for detection and sizing. The views of a T-SAFT data volume obtained from the fifty percent through-wall deep ID saw cut is shown in Figure 9.10. The C-Scan or plan view is shown in the upper left. Circumferential length information is obtained from this image's vertical axis. Note that only half of the flaw was imaged, with the center of the flaw at the top of the image. The horizontal axis gives the axial position of the flaw. The B-Scan side view in the lower left shows multiple signals. Depth information is obtained from the signal with the greatest amplitude in the center of the scanned aperture. Lastly, the B-Scan end view is shown in the upper right. Both depth and length are obtained from the vertical and horizontal image axes respectively.

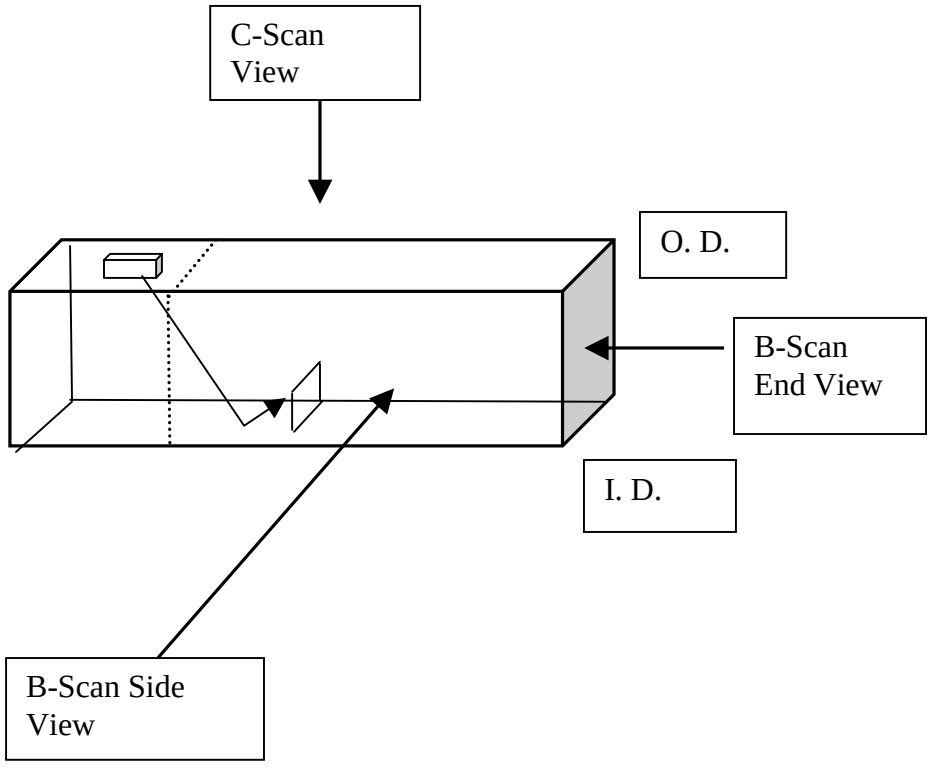

Figure 9.9. Three possible views of a flaw in the mockup SAFT data are shown. The transducer is scanning left of the weld and the part contains a flaw on the inner diameter surface.

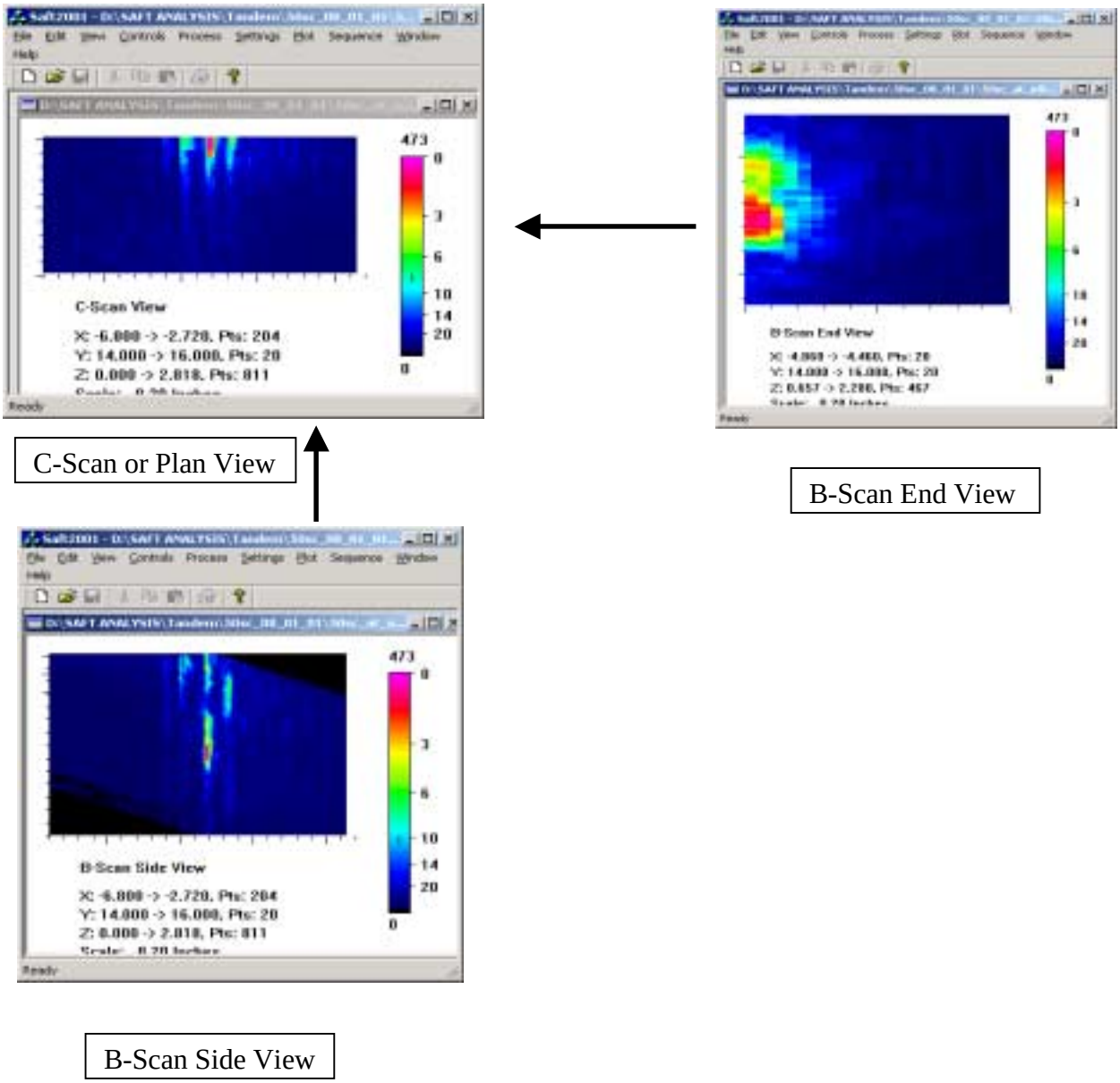

Figure 9.10. The three views of T-SAFT data from the 50% through-wall deep saw cut is shown. Depth sizing is obtained from either B-Scan view along the vertical axis in the image.

The T-SAFT data sizing is currently a manual operation. The user selects the signal of interest based on the largest amplitude in the central area of the file. Figure 9.11 shows B-Scan side view images from the thirty-five percent through-wall deep saw cut. The area of interest is extracted with a box command and is shown in the middle image. The depth sizing uses a six-decibel drop or half of the peak amplitude technique. The –6 dB points from the peak are located by clicking a cursor on the image and noting the depth or z-axis location. The through-wall flaw depth is found by taking half of the difference between the two 6 dB extremes. A clip level of -6 dB is displayed in the right image of Figure 9.11. This view may be helpful for sizing.

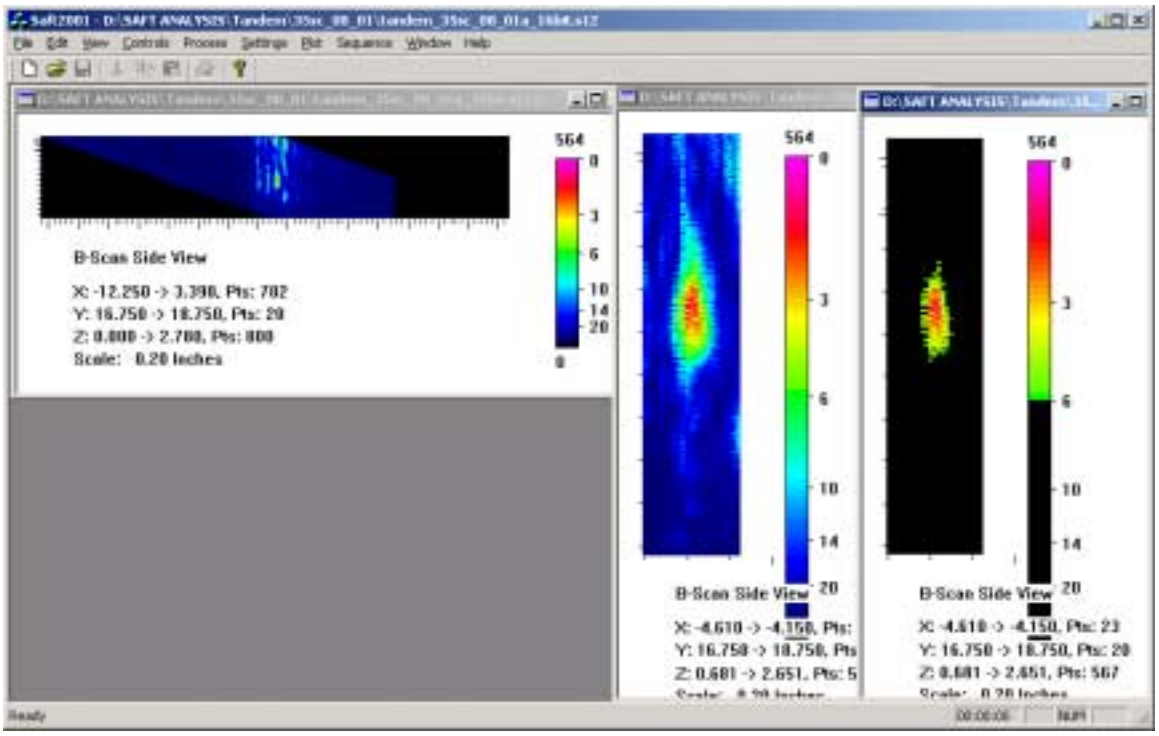

Figure 9.11. T-SAFT data from the 35% deep saw cut. The peak signal is extracted from the left image and shown in the middle. A clip threshold of –6dB is set in the right image.

Figures 9.12 through 9.17 show additional tandem SAFT data. Figure 9.12 shows the ten percent deep saw cut image. The Tandem technique requires that the signal of interest is located in the center of the scanned aperture. In most of the B-Scan side views there are multiple signals in the data file. These are from the numerous signals in the wave packet received from a flaw. Only those signals near the center of the data aperture are of interest. Figure 9.13 shows at least two vertical signals near the center of the image from the 20 percent deep saw cut. Signal on the edge of the aperture are ignored. The peak center signal was extracted for sizing and is shown in Figure 9.14. Figures 9.15, 9.16,

and 9.17 show the signals that were extracted and sized for the 40, 50, and 65 percent deep saw cuts respectively.

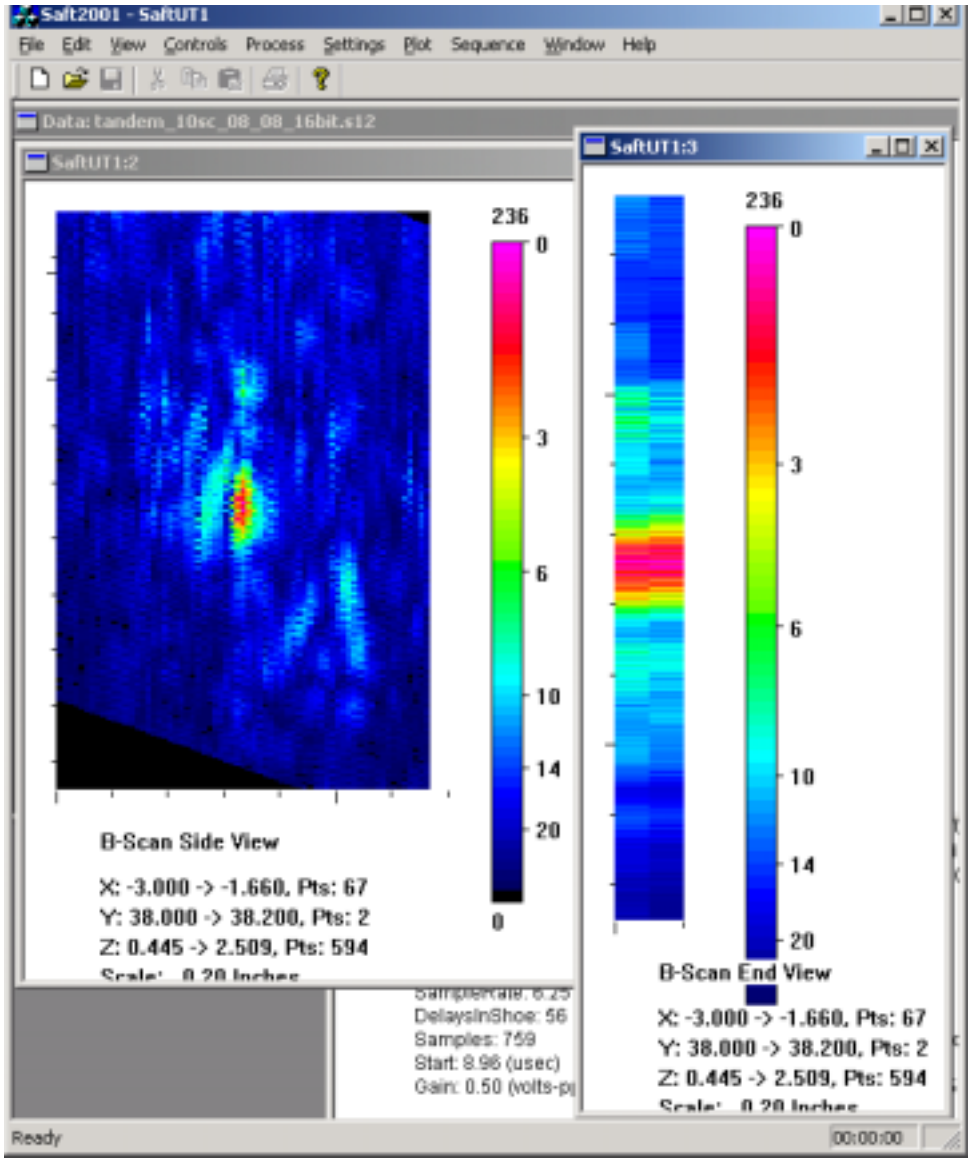

Figure 9.12. T-SAFT data from the 10% deep saw cut. Only two lines of data were acquired.

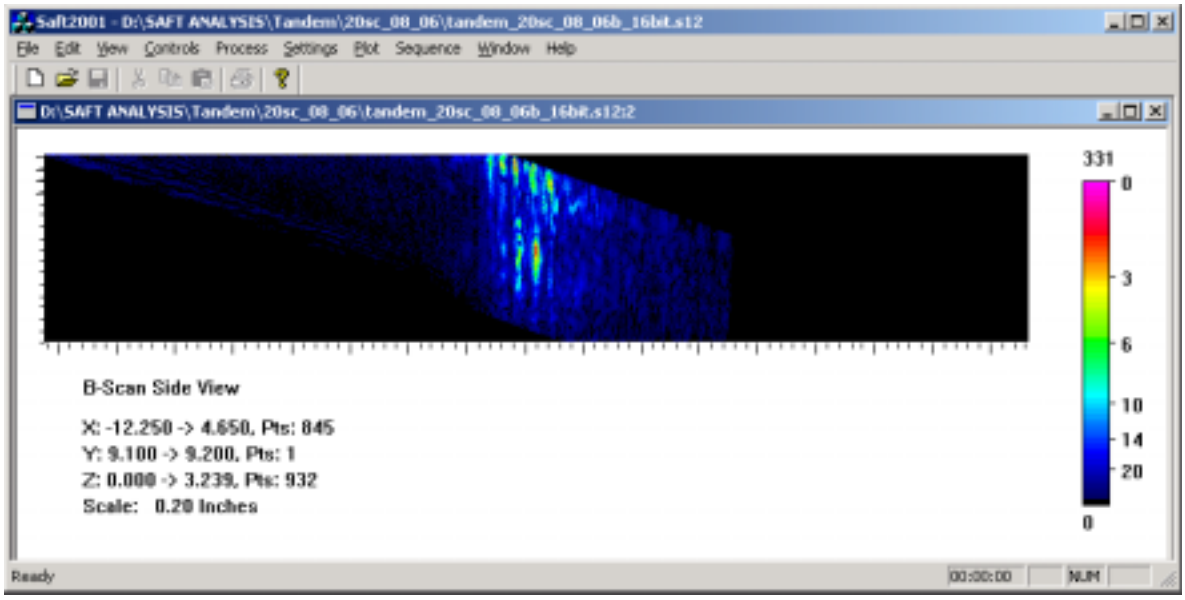

Figure 9.13. T-SAFT data from the 20% deep saw cut.

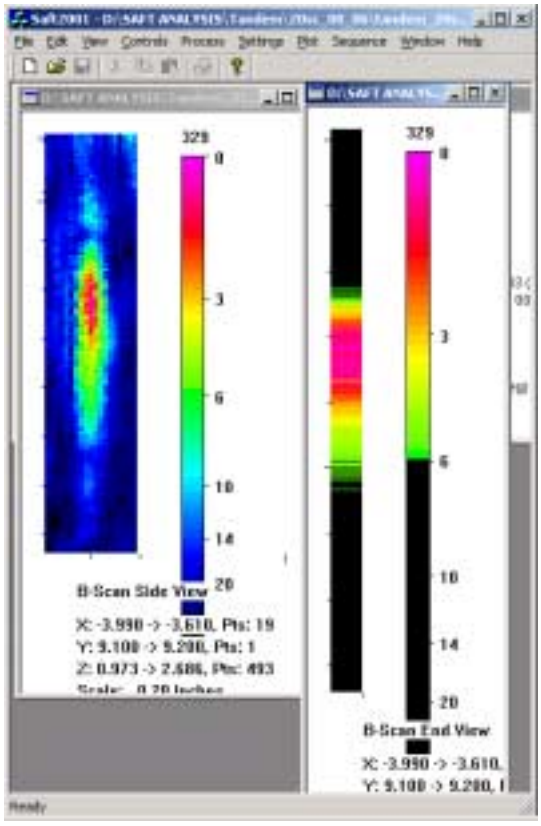

Figure 9.14. T-SAFT data from the 20% deep saw cut extracted from Figure 9.13 with the box feature. The clip feature results are shown on the B-Scan end view at right.

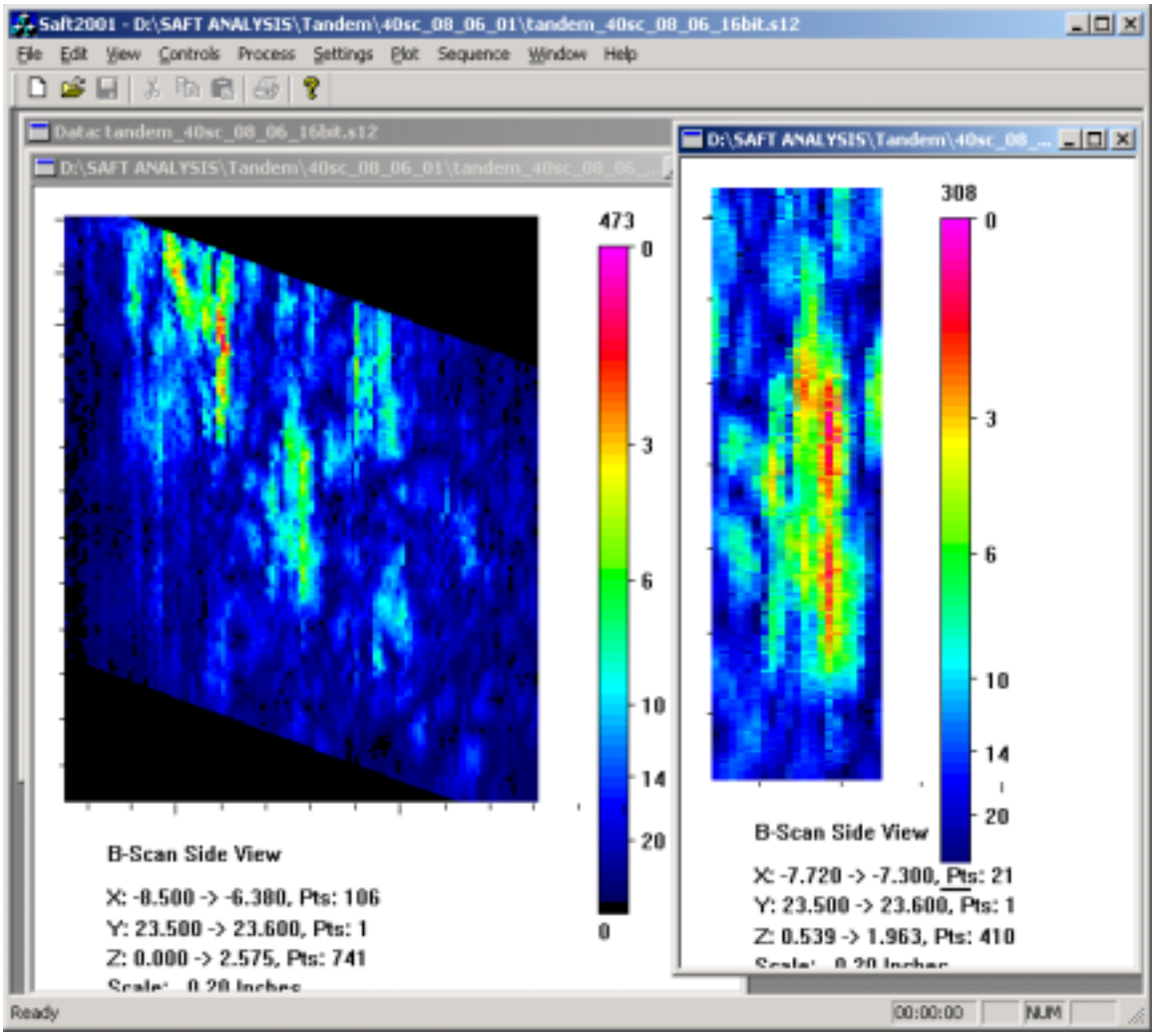

Figure 9.15. T-SAFT data from 40% deep saw cut showing many signals and the peak signal extracted on the right.

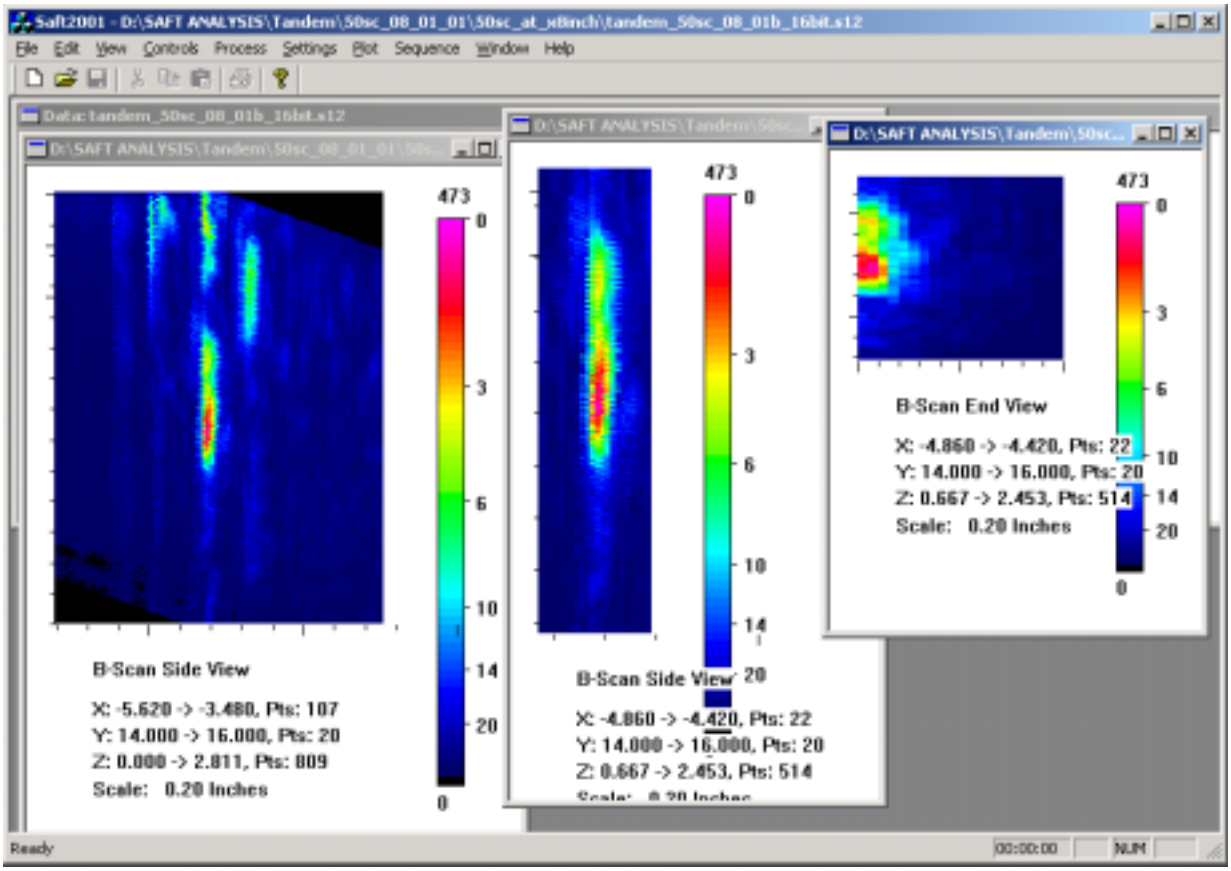

Figure 9.16. T-SAFT data from the 50% deep saw cut and the peak signal extracted in the middle and right images.

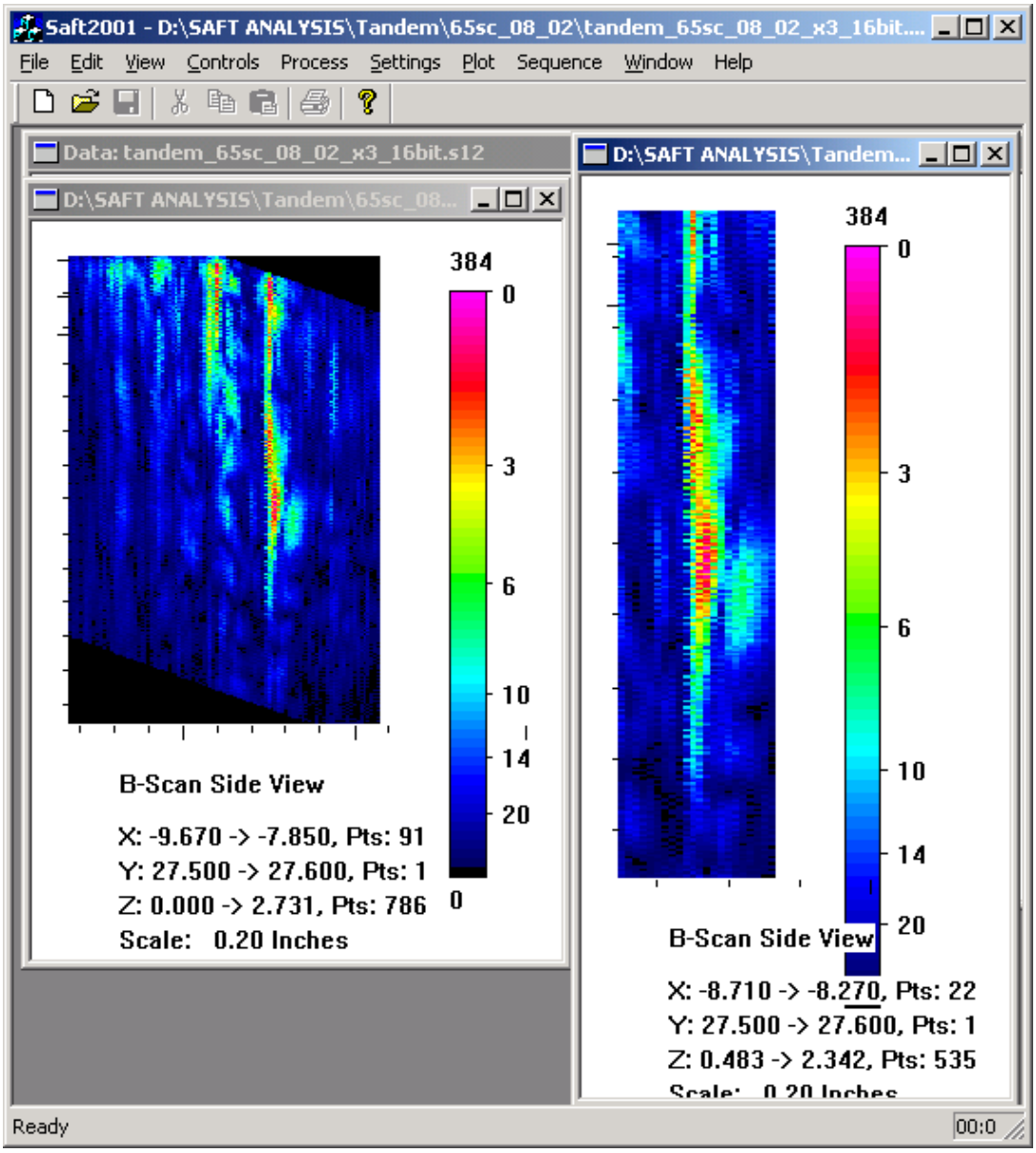

Figure 9.17. T-SAFT data from the 65 % deep saw cut and the extracted peak signal.

10 Modeling the Empirical Data

10.1 Model Development

This section describes the development of a computer model to aid in the interpretation and design of the T-SAFT curved shell inspection. Section 10.1.1 describes the formulation and the underlying reasoning of the model, along with an examination of the underlying causes of characteristic signal features. Section 10.1.2 presents a study of crack responses for typical experimental configurations.

10.1.1 Model Formulation

The model is comprised of three components, associated with i) the functioning of the transducer/wedge assembly as a transmitter/receiver, ii) the propagation of ultrasound between the point of transducer contact and the location of the flaw, and iii) the signal response of the measurement due to scattering by a crack. These issues are discussed individually.

10.1.1.1 Modeling of transmission/reception by the wedge transducer

In modeling transmission/reception by the wedge transducer, it was noted that transducer-to-flaw distances of 607 to 914 mm (2 to 3 ft.) are being considered. Under these conditions, it is argued that use of a far-field approximation to express the radiated field is appropriate. For a transducer/wedge assembly as used in this project, the far-field approximation represents the transducer as a point radiator with an angle-dependent radiation pattern. Figure 10.1 depicts a wedge transducer radiating to an unbounded steel half-space. Use of the far-field approximation is unequivocally valid when modeling propagation in the flat plate. In the case of the flat plate, the beam displays a geometrical divergence with ray distance equivalent to that displayed in the semi-infinite half-space. In the case of the curved shell, beam focusing can occur, as shall be seen later in this report. In regions of focusing, the far-field approximation is viewed with less confidence. At this point in the model development, the potential for error in regions of focusing is being noted, and future studies will determine if more elaborate schemes for modeling the transducer radiation/reception are required.

To simplify the model, the transducer radiation pattern is approximated to be in the form of a truncated cosine-squared function. As such, the model attempts to predict the transmission/reception of the main lobe of the transducer radiation pattern. Using this model, the radiation pattern is parameterized by two parameters, controlling the angular width of the aperture in the ‘in-plane’ and ‘out-of-plane’ directions, where the plane being referred to is the symmetry plane of the transducer, also the plane of the diagram in Figure 10.1(a). This plane is defined by the central axis of the transmitted beam, and the normal to the surface to which the transducers are in contact. The angular dependence is written

$$A(\theta_1,\theta_2) = F((\theta_1-\theta_{10})/\Delta\theta_1)\,F(\theta_2/\Delta\theta_2)$$
$$F(x) = \cos^2(2x/\pi), \quad |x|\le 1$$
$$= 0, \quad |x|>1 \tag{1}$$

where subscripts 1, 2 refer to in-plane and out-of-plane angular directions, respectively, θ_{10} is the transmission angle of the wedge in the steel, and half-width angles $\Delta\theta_1$, $\Delta\theta_2$ control the width of the angular aperture in the in-plane and out-of-plane directions. The angles are defined as follows. Consider a position vector $\underline{x}$ in 3 dimensions. The angle θ_2 is the elevation of this vector with respect to the transducer symmetry plane ($\underline{x}$ is parallel to the plane when θ_2=0). The angle θ_1 is the angle between the projection of $\underline{x}$ onto the transducer symmetry plane, and the surface normal vector. The parameters θ_{10} , $\Delta\theta_1$, $\Delta\theta_2$ can be obtained directly from experiment, by, say, comparing model predictions to experiment for reflection from a corner trap as a function of transducer position. Alternatively, these parameters could be extracted from results generated by more rigorous computer models of the transducer/wedge assembly. An in-plane radiation pattern centered at a 70-degree shear transmission angle is shown in Figure 10.2, having a 20-degree total aperture angle. The –6dB total aperture angle for this pattern is 10 degrees. This beam aperture is typical of the transducers being used in the corresponding experiments.

The transducer's radiation pattern is, of course, a frequency dependent function. An assumption is made that the radiation pattern at the center frequency of the transducer is not significantly different than that observed when monitoring the transducer broadband response. The model propagates a single frequency wave field at the transducer center frequency. Broadband responses are then approximated assuming the transducer radiation pattern is independent of frequency. This approximation is made to improve computational efficiency: is not an essential feature of the model. A more rigorous inclusion of the radiation pattern frequency dependence can be undertaken if needed.

In the current work, attention is restricted to shear wave transducers, that is, transducer/wedge systems that transmit vertically polarized shear (SV) waves at angles well beyond the critical angle for compressional (L) wave transmission. The shear wave field is represented by a single scalar displacement potential ψ. The field transmitted into a semi-infinite steel half space at a position $\underline{r}$ away from the transducer position is therefore expressed as a function of distance $r = |\underline{r}|$ and angle θ_1, θ_2 as

$$\psi(r,\theta_1,\theta_2) = A(\theta_1,\theta_2)\,r^{-1}\exp(i\,k_T\,r) \tag{2}$$

where k_T is the shear wave number given by $k_T = \omega/c_T$, where ω is time harmonic frequency and c_T is shear wave speed. To leading order in k_T, particle displacement components u_i, i=1,2,3, are expressed

$$u_i = i\,k_T\,d_i\,\psi \tag{3}$$

where $\underline{d}$ is a unit vector perpendicular to $\underline{r}$, and co-planar with the surface normal $\underline{n}$, with $\underline{n}\cdot\underline{d}>0$. Stress fields τ_{ij} are obtained by application of Hooke's law

$$\tau_{ij} = \lambda \partial_k u_k + \mu (\partial_j u_i + \partial_i u_j) \quad (4)$$

where λ, μ are the Lame' constants of steel. Should the use of this simple form for the radiation pattern prove inadequate at some future time, more exact expressions for the radiation pattern can easily be employed.

10.1.1.2 Ultrasound propagation in shell

Ray tracing is used to model propagation from the transducer to the flaw. To a first order approximation, the parameter that determines the adequacy of ray methods is the ratio of wavelength to the characteristic dimension of any reflecting objects. For the propagation problem at hand, the characteristic dimension is the radius of curvature of the shell wall. Since this dimension is several orders larger than the wavelength, ray theory should provide adequate predictions. It is noted that the thickness of the shell wall does not enter into this consideration: an exact model of plate wave propagation can be developed by the summation of individual wall reflections, regardless of wall thickness.

Discussion is first limited to 'in-plane' ray propagation, with ray geometry and field amplitude characteristics being examined as if the problem were two-dimensional in nature. Extension to the full three-dimensional problem will then follow.

An example problem is used throughout this section to illustrate the functioning of the model. A shell made of 24 mm (15/16 in.) thick steel is considered. Ray tracing results are shown for a planar shell in Figure 10.3. Rays transmitted at 60, 70, and 80 degrees are shown. Ray tracing in a curved shell having a 305 mm (12 in.) radius of curvature is shown in Figure 10.4, again for angles of 60, 70, and 80 degrees. The 60-degree ray in Figure 10.4 multiply reflects between the shell walls, similar to the propagation in the planar shell wall. It is significant to note that, at 70 degrees, the ray in the curved shell propagates near grazing incidence on the inner shell wall, and that at 80 degrees, the ray never interacts with the inner shell wall. It is also significant to note that all ray reflections in the 20-degree angular range considered remain beyond the critical angle for shear-to-compressional wave mode conversion, that is, only shear waves propagate in the shell for the aperture angles of interest. This fact significantly simplifies the model formulation.

An exception to the criteria for applicability of ray theory is the occurrence of grazing incidence on a convex surface, which gives rise to a diffracted field that penetrates into the resulting 'shadow' region. Such a case is seen in the grazing incidence on the inner shell wall observed in the 70-degree ray in Figure 10.4. To predict diffracted fields, 'first order' ray methods must be supplemented with the Geometrical Theory of Diffraction (GTD). Inclusion of GTD represents a significant complication of the modeling effort. It is argued that diffraction effects need not be rigorously modeled to obtain reasonable predictions of transducer output signals, because the T-SAFT measurement to be

employed is designed to capture specular reflections as the dominant contributor to the output signal. The ray methods employed here should provide reasonable predictions of the contributions from these specular reflections. Inclusion of GTD could be undertaken at a later time if it becomes evident that it is needed.

The determination of the field amplitude along the propagating rays, or 'ray amplitude', will now be discussed. In 'first order' ray theory, the amplitude of the field is proportional to the square root of the area circumscribed by a 'tube' of rays. This relation can be seen to follow directly from the conservation of energy carried within such a 'flux tube'. For fields that diverge with distance, such as seen in transmission in the planar shell of Figure 10.3, this relation works well. In situations where focusing occurs, however, this relation breaks down, as it predicts infinite field amplitudes at points where neighboring rays intersect. Such a case arises in connection with rays that interact only with the outer shell wall. Accurate prediction of focused field amplitudes requires a more rigorous examination of the underlying mathematics.

A simple *ad-hoc* approximation for prescribing field amplitude along the ray is to utilize the field amplitude of an appropriately related gaussian beam. For example, consider the angular aperture function displayed in Figure 10.2. A corresponding gaussian beam profile could be prescribed as, say, that having the same profile curvature at the center of the beam as the cosine-squared profile. This criterion leads to a gaussian coefficient

$$\alpha = \left(\frac{\pi}{k_T \, 2\Delta\theta} \right)^2 \tag{5}$$

The variation in amplitude resulting from field divergence/convergence is thereby expressed as that of the on-axis response of the corresponding gaussian beam under the paraxial approximation

$$D = (1 + i\, z / (2 k_T \, \alpha))^{-1/2} \tag{6}$$

where z is the distance from the point of focus, or 'focal distance'. An appropriate focal distance z is determined by examining the distance between neighboring rays. For example, in a semi-infinite half-space as depicted in Figure 10.1, two rays emerging from the transducer position with an angular separation $\Delta\theta$ will have a separation Δl expressed as a function of distance as

$$\Delta l = z \, \Delta\theta \tag{7}$$

Therefore, when considering two rays at some point in the shell which were initially launched at a relative angle $\Delta\theta$, it is reasonable to prescribe the distance z to be

$$z = \Delta l / \Delta\theta \tag{8}$$

where Δl is the perpendicular distance between the two rays. This value of z would then be used in eq.(6) to determine the ray amplitude at that point. Note that this distance does not represent the distance to the point of intersection of the neighboring rays. Rather, it simply provides the parameter to be used in the gaussian expression for ray amplitude. For example, cases of reflection can arise for which the neighboring rays are oriented parallel. The distance to the intersection of these parallel rays is infinite. However, the amplitude is finite and constant along these rays. Eq.(6) provides a simple means for estimating the amplitude along the rays.

The simple 'equivalent gaussian beam' approach to prescribing ray amplitude yields a reasonable expression for the ray amplitude in the case of a 'point focus', that is, a case where all the rays over the transducer aperture pass through a single point. For example, if the rays in Figure 10.1 (a) were reflected from a cylindrical surface with center coinciding with the transducer position, all the in plane reflected rays would pass through the transducer position. Eq.(6) would provide a reasonable estimate of the field amplitude in this case. However, it is common for focusing to occur over an extended "caustic surface", where adjacent pairs of neighboring rays intersect at neighboring points on the caustic surface. In such a case, this ad-hoc means of prescribing ray amplitudes will over-estimate the field amplitude. A more accurate estimate of field amplitude requires a closer examination of the ray geometry.

An example is considered which demonstrates a typical focusing caustic encountered in the curved shell geometry. A key step in the model operation is to determine the incident ultrasonic field over the perpendicular cross-section of the shell at the position of the flaw. The perpendicular cross-section is generated by the plane perpendicular to both the inner surface of the shell wall, and the radial-axial plane of the tank geometry. The planar cracks assumed in the current modeling effort are specified to lie in this cross-sectional surface, referred to at times as the 'flaw plane'. In the example at hand, it is desired to know the field over the perpendicular cross-section at the junction of the curved and straight shell segments on the far side of the curved shell section, that is, at the junction of the knuckle and tank bottom. The ray tracing shown in Figure 10.4 corresponds to this case. Figure 10.5 plots the position of the in-plane ray intersection on the cross-sectional surface as a function of ray angle, where s=0mm corresponds to the inner tank wall, and s=24mm (15/16 in.) corresponds to the outer shell wall. The 'zig-zag' pattern seen over the range of 60.0 to 69.6 degrees is characteristic of rays multiply reflecting between the inner and outer shell walls. The shape of the curve in the angular range between 69.6 and 80.0 degrees is characteristic of rays which are multiply reflecting from a single concave surface, i.e. a "whispering gallery" mode of propagation. As previously implied, first-order ray theory predicts the field amplitude as inversely proportional to the square root of the distance between neighboring rays, where neighboring rays are defined as rays emerging from the transducer point at angles differing by a small angular increment $d\theta$. It is evident, then, that the distance between neighboring rays is proportional to the slope $ds/d\theta$ of the curve $s(\theta)$ plotted in Figure 10.5. The crossing of neighboring rays, i.e. focusing, occurs when the slope of the curve vanishes, as seen at θ =72.6 and θ =78.3 degrees. (The abrupt changes in slope seen at s=0mm and s=2.38mm indicate points of wall refection, and do not indicate

focusing. Also, the abrupt change in slope seen at θ =69.6 degrees indicates the shadow boundary cast by grazing incidence on the inner shell wall. Again, this is not a point of focusing.) Rays intersecting the cross-sectional surface for θ between 69.6 and 76.4 degrees are plotted in Figure 10.6. Note the surface formed by the points of ray intersection: this surface is referred to in ray theory as a 'caustic surface', or a 'focusing caustic'. It is seen that the caustic surface intersects the cross-sectional surface at s=6.75mm, corresponding to the vanishing of ds/dθ at θ =72.6 degrees in Figure 10.5.

It is noted that, although the ray theory expression for amplitude is invalid in the vicinity of focusing, the expression attains validity at a sufficiently large distance from the point of focus (assuming intersecting rays are not co-linear). This observation suggests an algorithm for obtaining an acceptable expression of ray amplitude in regions of focusing. This algorithm constructs an "equivalent" radiating aperture that, when analyzed using first-order asymptotic analysis, yields the erroneous prediction of first-order ray theory. The field in the focal zone is then obtained by a more rigorous asymptotic analysis of radiation by the equivalent aperture. An approach that has been tested constructs the equivalent aperture by "back propagating" in the direction of the ray segments in Figure 10.6 a distance equal to the total path length traversed by each ray between the transducer and cross-sectional plane, but as if the rays were propagating in an unbounded steel medium. The upper ends of these back-propagated ray segments define the geometry of the equivalent radiating aperture. This equivalent aperture formed by back propagation is depicted in Figure 10.7. The field on the cross-sectional plane is then expressed using a Green function boundary integral formulation over the surface of the radiating aperture. This boundary integral is evaluated using phase integral asymptotic analysis (saddle point, or stationary phase analysis). For sake of discussion, assume that positions on the radiating aperture are parameterized as $\underline{x}(q)$. Formally written, this analysis represents the wave field as an integral of the form

$$\psi(\underline{x}^s) = \int A(q) \exp(i k_T r(q)) \, ds(q) \qquad (9)$$

where A is an amplitude factor involving both the amplitude of the wave field on the radiating aperture and the amplitude of the Green function, and r(q) is the distance between points on the radiating aperture $\underline{x}(q)$ and the point on the cross-sectional surface $\underline{x}^s$ at which the field is to be evaluated. First order ray theory is obtained by approximating r(q) by a second order polynomial expansion about the point at which the ray emanating from the point $\underline{x}^s$ intersects the aperture surface. This approximation, along with the assumption that the amplitude term A(q) is constant about the expansion point, leads to a simple analytic expression for the field amplitude, that being the first-order ray theory expression for ray amplitude. The singular prediction of ray amplitude occurs when the second-order expansion coefficient of r(q) vanishes. A more rigorous analysis approximates r(q) by a third-order polynomial expansion rather than a second order expansion. This more rigorous analysis, referred to as a "uniform" asymptotic expansion, produces a bounded prediction of ray amplitude when the second order expansion coefficient vanishes, assuming that both the second order and third order expansion coefficients do not simultaneously vanish.

Results comparing three methods of computing ray amplitude are presented in Figure 10.8. This plot shows the predicted field amplitude on the cross-sectional surface as a function of initial ray transmission angle θ, where θ ranges from 69.6 to 76.4 degrees. The singular prediction of first-order ray theory at the focusing caustic is evident. The amplitude predicted by the higher-order asymptotic analysis, in contrast, is well behaved at the focusing caustic. Also compared is the prediction made by the 'equivalent gaussian beam' approximation, which is seen to substantially over-estimate the amplitude of the field at the focusing caustic.

In the example considered above, the 'equivalent aperture' algorithm is effective in correcting the singular ray amplitude predicted by first-order ray theory. However, attempts to apply this approach in a general fashion have run into difficulties. For example, the algorithm fails in situations where neighboring rays are nearly parallel. For this reason, application of the 'equivalent aperture' must be carefully monitored, leading to a less-than-robust algorithm. Current work is examining alternative approaches to overcome the pathologies of first-order ray theory, to be test-implemented in the future. The 'equivalent gaussian beam' approximation, on the other hand, performs quite robustly, albeit with its known over-estimation of field amplitudes at focusing caustics. The solution to this problem adopted for the time being is to employ an 'equivalent gaussian beam' approach in which the beam width parameter is adjusted to obtain agreement between the gaussian beam response profile and the uniform asymptotic expansion response profile observed in Figure 10.8. The reasoning behind this approach is that the focusing caustic observed in Figure 10.6 is typical of the focusing geometry to be encountered generally by the model. As work unfolds, the significance of the error inherent in this approximation will become apparent.

Another factor contributing to ray amplitude is the reflection coefficient encountered at the shell wall. The reflection coefficient at the outer shell wall is assumed to have a unit complex modulus, implying that energy loss due to coupling to the surrounding air is negligible (there is a phase shift associated with total reflection beyond the L-wave critical angle). The magnitude of the reflection coefficient at the inner shell wall, however, will be less than 1, due to coupling into liquid talk contents. For 70-degree shear wave incidence on a steel/water interface, the reflected shear wave will experience a 7.86 percent reduction in amplitude. The ray propagating at 65 degrees in the example at hand reflects from the inner shell wall four times between the transducer and cross-sectional surface. This implies a reduction in ray amplitude by a factor of .713 due to leakage into water. It is interesting to note that the rays that interact only with the outer shell wall do not sense the liquid loading of the inner tank wall.

Discussion to this point has primarily focused on the 'in-plane' ray propagation, with field amplitude characteristics being examined as if the problem were 2D in nature. Experimental interest, of course, is in a three dimensional problem. Determination of the wave field in three dimensions involves a relatively simple enhancement of the 2D problem.

Figure 10.4 depicts rays in the radial-axial plane of the cylindrical tank structure (in-plane rays). To model propagation of rays not contained in this plane (the 'out-of-plane' rays depicted in Figure 10.1 (b)), the curvature of the tank wall in the circumferential direction is ignored. In other words, for practical purposes, the diameter of the storage tank can be considered infinite. Under this assumption, the ray tracing of in-plane rays represents the projection of the out-of-plane rays onto the radial-axial plane. This fact greatly simplifies the analysis, since the ray geometry in three dimensions can be inferred from the two-dimensional ray tracing employed in Figure 10.4. In what follows, the radial-axial plane of the tank is also referred to as the symmetry plane, consistent with the fact that the symmetry plane of the transducer is aligned with the radial-axial plane of the tank in the experimental configuration.

In the preceding discussion concerning 2D 'in-plane' propagation, the ray amplitude at a point on the cross-sectional surface is expressed as a function of angle θ as

$$\psi(\theta) = A(\theta)\, D(\theta) \exp(i\, k_T\, p(\theta)) \tag{10}$$

where θ is implicitly understood to be the in-plane angle θ_1, $A(\theta)$ is implicitly understood to mean $A(\theta_1,0)$ in eq.(1), and the path length $p(\theta)$ is implicitly understood to mean $p(\theta_1,0)$. The factor $D(\theta)$ expresses the variation of ray amplitude due to ray divergence/convergence in the two-dimensional propagation problem. In what follows, the in-plane ray path length $p(\theta_1,0)$ will be denoted $p_0(\theta_1)$. It is desired to determine the field at points on the cross-sectional surface containing possible cracks. Position on this surface is expressed by the distance s from the inner shell wall (as depicted in Figure 10.5, and the distance y perpendicular to the symmetry plane. The relation between out-of-plane distance y and angle θ_2 is seen to be

$$y = p_0(\theta_1) \tan(\theta_2) \tag{11}$$

The path length to points on the cross-sectional surface, expressed as a function of θ_1, θ_2, is seen to be

$$p(\theta_1, \theta_2) = p_0(\theta_1) / \cos(\theta_2) \tag{12}$$

It follows that the field at points on the cross-sectional plane can be conveniently expressed as a function of aperture angle as

$$\psi(\theta_1, \theta_2) = A(\theta_1, \theta_2)\, D(\theta_1)\, p^{-1/2}(\theta_1, \theta_2) \exp(i\, k_T\, p(\theta_1, \theta_2)) \tag{13}$$

An issue that raises a bit more complexity in the problem is the rotation of the shear polarization upon reflection in the curved shell section. For the in-plane rays, the shear polarization remains everywhere SV (vertically polarized). However, for the out-of-plane rays, the polarization changes slightly with each reflection from the curved shell, that is, the incident polarization vector has a small tangential SH (horizontally polarized) component at the reflecting surface when the surface normal at the point of reflection is

not parallel to that of the previous reflection. Work to date indicates that the consequence of this effect is not significant, and that approximating the polarization to be pure SV at all reflecting surfaces yields reasonable results for the angular apertures of interest.

10.1.1.3 Flaw Signal Prediction

The third component of the measurement model is the prediction of the transducer output signal in response to cracks initiating on the inner or outer tank wall. A planar crack is assumed to lie in the perpendicular cross-sectional surface of the shell, as previously defined. The crack is assumed to be either half-elliptical or rectangular in shape, characterized by width w and height h, as depicted in Figure 10.9.

Transducer output voltages are evaluated by application of Auld's reciprocity theorem (B.A. Auld, 1979). This theorem states that the output voltage from the receiving transducer due to scattering by the crack can be evaluated provided that 1) the wave field on the surface of the crack created by the transmitting transducer is known, and 2) the wave field that would exist in the absence of the crack is known over the surface occupied by the crack in the case where the receiving transducer is used as a transmitter rather than receiver. The mathematical expression of Auld's reciprocity is

$$v(\omega) = C \int_S u_i(x,\omega)\, \tau_{ij}^{re}(x,\omega)\; n_j(x)\, dx \qquad (14)$$

where $v(\omega)$ is the output voltage in the frequency domain, C is a multiplicative factor depending on, among things, the transduction efficiency of the transducers, S denotes the surface of the crack, $u_i(x,\omega)$ are the vector components of the particle displacement on the crack face caused by the transmitting transducer, $\tau_{ij}^{re}(x,\omega)\, n_j(x)$ is the traction on the plane of the crack face that would exist in the absence of the crack if the receiver were used as a transmitter, and $n_j(x)$ is the unit normal vector on the crack face. Fields from the transmitting and receiving transducers are propagated to the cross-sectional surface containing the crack using the previously discussed ray tracing methods. The field on the crack face generated by the transmitting transducer is determined by applying a first-order ray theory reflection on the crack face. No attempt is made to model field displacements arising from diffraction at the crack tip or root, such as diffracted Rayleigh waves. In this sense, the model is seen to be a 'physical optics', or 'Kirchhoff' approximation.

As previously mentioned, the wave field is propagated as if the transducer radiation pattern and resulting field amplitude is frequency independent, and corresponds to that of the transducer center frequency. That is, the complex moduli $|u_i(x,\omega)|$, and $|\tau_{ij}^{re}(x,\omega)|$ are independent of frequency, and equal to that generated at the transducer center frequency. Frequency dependence of these quantities is seen only in the phase factors $\exp(i\, \omega/c_T\, p(\theta_1,\theta_2))$. As previously mentioned, this assumption provides a considerable improvement in computational efficiency, but it is not essential. A more complete consideration of the field frequency dependence can be employed in the future should it be needed.

Referring to Figure 10.5, it is seen that the mapping of transmitted ray angle onto the cross-sectional surface is not a one-to-one mapping. For example, referring to Figure 10.5, it is seen that there are nine rays that intersect the cross-sectional surface midway through the shell (s=11.9mm). Therefore, carrying out the integration of eq.(14) requires first summing all contributing rays at each position on the flaw surface, to construct the total wave field at each position. Following this step, the evaluation of the Auld's reciprocity integral involves a straightforward numerical quadrature applied over the face of the crack. When considering reflection from a plate edge, the integration in the out-of-plane direction in eq.(14) is evaluated using a stationary phase expansion about the in-plane position.

The frequency response of the transducer is assumed in the form

$$F(\omega) = \cos^2\left(\frac{(\omega-\omega_0)}{\Delta\omega}\frac{\pi}{2}\right) \quad , \quad |\omega-\omega_0| \le \Delta\omega$$
$$= 0 \quad , \quad |\omega-\omega_0| > \Delta\omega \qquad (15)$$

where ω_0 s the transducer center frequency, and $\Delta\omega$ is the half-bandwidth of the transducer. For the numerical results presented here, the half-bandwidth is set equal to the center frequency ω_0. Computation of time domain signals follows from fast Fourier transformation (FFT) of the frequency domain response computed by eq.(14).

This section of the report closes with a detailed look at the signal reflected from the edge of both flat and curved plate sections. The plate edge is treated as a 100% through-thickness crack of infinite width.

Results for a flat plate are considered first. A single transducer used in pulse-echo mode is positioned at a distance 483 mm (19 in.) from the plate edge, equal to the distance used in the curved plate example depicted in Figure 10.4. The received signal from the plate edge is shown in Figure 10.10. It is seen to consist of multiple signal components, corresponding to the multiple ray paths that intersect any given position on the cross-sectional surface. To understand the origin of these signal components, key ray path characteristics are examined. A plot of the in-plane ray intersection position versus ray transmission angle is shown in Figure 10.11, corresponding to the curved shell result of Figure 10.5. It is seen that eight rays intersect the center of the cross-section. A plot of ray path length versus ray transmission angle is shown in Figure 10.12, showing that the ray path length decreases monotonically with increasing ray transmission angle. A plot of ray amplitude on the cross-section versus ray transmission angle is shown in Figure 10.13, which is quite similar to the angular aperture function of the transducer. From Figures 10.12 and 10.13, it is seen that the earliest and latest signals arriving to and from the crack are from the largest and smallest transmission angles, respectively. Therefore, based on this observation alone, one would expect up to 15 signal components, with the largest signals being received in the in the center of the signal train. In addition to dependence on the ray amplitude shown in Figure 10.13, the amplitude of the signal components will depend on the relative orientation of ‘receiver” and ‘transmitter’ rays on the cross-sectional surface. That is, whether the ‘receiver’ ray is well oriented to receive a ‘transmitter’ ray reflected from the surface, with optimum orientation being parallel.

These conditions are depicted in Figure 10.14. It is evident that about half the receiver-transmitter ray combinations will be well oriented for signal reception. The predicted signal in Figure 10.10 is entirely consistent with these expectations.

Results are next considered for the curved shell section. Again, a single transducer used in pulse-echo mode is positioned at a distance 483 (19 in.) from the plate edge, corresponding to the diagrams of Figure 10.4. The received signal from the plate edge is shown in Figure 10.15. As in Figure 10.10, it is seen to consist of multiple signal components, corresponding to the multiple ray paths that intersect any given position on the cross-sectional surface. Significant differences are seen the shape of the wave train envelope, however, when compared to the signal received in the flat plate. To understand the features of this signal train, plots of ray path length and ray amplitude as a function of angle are examined, shown in Figures 10.16 and 10.17, respectively. Referring to Figure 10.5, its is seen that between 7 to 11 rays intersect a given point on the cross-sectional surface, depending on the position of the point. Referring to Figure 10.16, it is seen that the shortest travel time occurs for the rays transmitted around 70 degrees, corresponding to the occurrence of tangential incidence on the inner shell wall. Figure 10.17 indicates that, at the earliest arrival time (69.6 degrees), the ray amplitude is relatively small, but that the largest ray amplitudes occur a short time later around transmission angles of 72.6 degrees, corresponding to the occurrence of the focusing caustic. Note that in this case, the ray amplitude versus transmission angle is substantially different in nature than the angular aperture function. Combining these observations, it is expected that the wave train will consist of up to 20 components, with approximately half of those being of appreciable amplitude. It is expected that the earliest signals will have relatively small amplitudes, but that the largest amplitude signals will follow shortly thereafter. Again, the predicted signal in Figure 10.15 is entirely consistent with these expectations.

The signals predicted by the model display a good qualitative resemblance to the experimental data, and serve to explain the origin of observed signal characteristics. The following section of the report presents a more detailed analysis of crack signals for typical experimental configurations.

10.1.2 Model Application to Crack Signal Analysis

An application of the model to the analysis of crack signals in an experimental geometry typical of the T-SAFT shell inspection is presented. A 3.5 MHz 12.7 mm (0.5 in.) diameter transducer mounted on a wedge designed for transmitting 70-degree shear waves in steel is assumed. In the first three examples, a 24 mm (15/16 in.) thick tank wall is assumed, with a 305 mm (12 in.) radius knuckle. The transducer is in contact with the shell just above the knuckle region. Cracks are assumed located at the transition between the knuckle and tank bottom, oriented within the cross-sectional surface as previously defined. Cases for cracks growing out of both the inner and outer shell walls are considered. In both cases, cracks are assumed to be rectangular in profile, with dimensions 25.4 mm (1 in.) wide by 4.8 mm (0.1875 in.) deep, corresponding to a 20% through-wall crack depth. It is assumed that both the inner and outer shell wall are

exposed to air, to simulate the conditions of the experimental test section being used for the inspection development.

Signals are first examined using a single transducer in a pulse-echo mode. The signal is shown in Figure 10.18 for the crack on the inner wall, for a transducer positioned 9.9 mm (0.39 in.) from the wall-knuckle transition. This is the same transducer and flaw plane location assumed in the edge-reflection example discussed in the previous section. When compared to the signal of Figure 10.15 for the reflection from a plate edge, it is seen that the signal train envelope for the crack is substantially different. To understand the origin of the signal components in Figure 10.18, rays intersecting the midpoint of the crack face are examined. Referring to Figure 10.5, and noting that the 20% through-wall crack on the inside shell wall extends from s=0.0mm to s=4.76mm, it is seen that that there are 7 rays from the transmitter and receiver (one in the same transducer for the pulse-echo measurement) which intersect the midpoint on the crack at s=2.38mm. A subset of the various combinations of transmitter and receiver ray paths will contribute significantly to the crack signal, determined by the relative ray orientation as depicted in Figure 10.14.

The ray paths contributing significantly to the 5 dominant signal components numbered in Figure 10.18 are plotted in Figure 10.19. These diagrams depict how the signal results from a series of “corner trap” reflections at the crack face and inner shell wall. Upon examination, it appears that the signal is comprised of combinations of three categories of ray paths. In Figure 10.19 (a), it is seen that the rays undergo four wall reflections between the transducer and the vicinity of the flaw (the “corner trap” inner wall reflection near the flaw is not being counted). These rays contribute to signal component 1. In Figure 10.19 (d), the rays undergo 6 reflections, contributing to signal component 3. In Figure 10.19 (f), the rays undergo 8 reflections, contributing to signal component 5. Signal components 2 and 4 are seen to be comprised of different combinations of these ray path types. Signal component 2 is generated by ray path pairs in which one ray undergoes 4 reflections, and the other ray undergoes 6 reflections. Signal component 4 is generated by ray path pairs in which one ray undergoes 6 reflections, and the other ray undergoes 8 reflections. Looking in more detail, it is seen that these “mixed ray path” signal components in turn consist of two different types of ray interactions.
Figure 10.19 (b) depicts the case where, upon reaching the “corner trap”, the ray undergoing 4 reflections first hits the inner shell wall, then the crack face, whereas the ray undergoing 6 reflections first hits the crack face, then the inner shell wall. Figure 10.19 (c) depicts the opposite case, that is, the ray undergoing 6 reflections first hits the inner shell wall, then the crack face, whereas the ray undergoing 4 reflections first hits the crack face, then the inner shell wall. It is noted that these two cases result in signals having slightly different arrival times, resulting in an extended multiple-pulse transient response. Figure 10.20 (a) shows an expanded view of signal component 2.
Figure 10.20 (b) individually plots the two contributions to Figure 10.20 (a) from the ray paths in Figures 10.19 (b) and 10.19 (c). The six ray diagrams shown in Figure 10.19 represent the main contributors to the signal train. The analysis can be continued to examine numerous more combinations, which contribute to the smaller signal components distributed throughout the wave train.

The signal from the crack on the outer shell wall is considered next, shown in Figure 10.21. Noting that the crack extends from s = 19.04 mm to s = 23.81 mm in Figure 10.5, it is seen that up to 9 rays intersect points on the crack face. The ray paths contributing most significantly to the five numbered signal components in Figure 10.21 are plotted in Figure 10.22, which shows rays intersecting the mid point on the crack face. Again, the ray paths can be grouped into categories determined by the number of wall reflections between the transducer and crack vicinity. Figure 10.22 (a) depicts ray paths involving two reflections on the outer shell wall. Note that these rays do not interact with the inner shell wall. Of the contributing signal paths, this path is the shortest, resulting in the signal component 1. Figure 10.22 (c) depicts ray paths involving five reflections, contributing to signal component 3. Figure 10.22 (e) depicts ray paths involving 7 reflections, contributing to signal component 5. Signal components 2 and 4 result from combinations of these ray paths, as depicted in Figures 10.22 (b) and 10.22 (d), respectively.

It is evident that the signal trains obtained from cracks on the inner and outer shell wall have distinctively different features. This fact presents a possibility for discriminating between inner and outer wall cracking. Whether or not such a distinction could be performed in actual practice will depend on the degree to which the experimental configuration can be calibrated and controlled. For example, features of the wave train will depend, to a greater or lesser extent, on the uniformity of the shell wall geometry, the exact position of the probe, and the quality of the ultrasonic coupling of the transducer wedge to the shell wall. Upcoming work needs to examine the needed accuracy in the *a priori* knowledge of these factors, to determine if use of differences in signal features as observed in Figures 10.18 and 10.21 would be practical for flaw characterization.

Results are next compared for a two transducer “pitch-catch” measurement, as used in collection of T-SAFT data. In this example, a first transducer is positioned 76.2 mm (3.0 in.) from the tank wall-knuckle transition. A second transducer is positioned 9.9 mm (0.39 in.) from the tank wall-knuckle transition, as in the previous example. As before, 20% through-wall crack is assumed, positioned on the inner tank wall at the knuckle-tank bottom transition. The predicted signal in this case is plotted in Figure 10.23. The ray paths associated with numbered signal components in Figure 10.23 are plotted in Figure 10.24. Again, it is seen that the various component signals are associated with different combinations of ray paths. Figure 10.24 (a) depicts a ray path pair contributing to the signal component 1 in which both rays undergo 4 reflections between the transducers and the vicinity of the crack. Figure 10.24 (b) depicts a ray path pair contributing to the signal component 2 in which the rays undergo 6 and 4 reflections, respectively. Figure 10.24 (c) depicts a ray path pair contributing to the signal component 3 in which both rays undergo 6 reflections. Figure 10.24 (d) depicts a ray path pair contributing to the signal component 4 in which the rays undergo 8 and 6 reflections, respectively. Figure 10.24 (e) depicts a ray path pair contributing to the signal component 5 in which the rays undergo 10 and 4 reflections, respectively. Figure 10.24 (f) depicts a ray path pair contributing to the signal component 6 in which the rays undergo 10 and 6 reflections, respectively. Figure 10.24 (g) depicts a ray path pair contributing to the signal component 7 in which the rays undergo 10 and 8 reflections, respectively. There are

numerous other combinations that contribute to the complex structure of the signal train, as can be inferred from these examples.

A final example is presented, in which the computational model is used to generate a B-scan data set, as collected in scanning experiments. A shell thickness of 22.2 mm (7/8 in.) is assumed. A crack is positioned in the knuckle region on the inner shell wall at a distance of 254 mm (10 in.) from the tank wall-knuckle transition. The crack is elliptical in profile, and has a width of 82.3 mm (3.24 in.), and depth of 14.4 mm (0.568 in.), corresponding to a 65% through-wall crack. The transducer characteristics are assumed the same as in the preceding examples. The transducer is scanned on the shell wall from a distance of 335 mm (13.2 in.) to 173 mm (6.8 in.) from the wall-knuckle transition. The computed signal data is presented in a B-mode image format, where the horizontal direction indicates scan position, the vertical direction indicates time (increasing downward), and pixel intensity or color indicates rectified signal amplitude. The computed B-mode image is presented in Figure 10.25. The corresponding experimental B-mode image, from which the parameters for the computation were derived, is presented in Figure 10.26. The two images display a qualitative resemblance, in that signal packet arrival times and complexity of structure are similar. The result indicates that the model is addressing the relevant physics of the problem. When compared in close detail, however, a substantial difference is seen in individual waveforms at nominally the same scan position. This is to be expected at this stage of the work, since calibration experiments to determine precise model inputs have yet to be performed. A task to rigorously calibrate the model to experiment is the next step in the work.

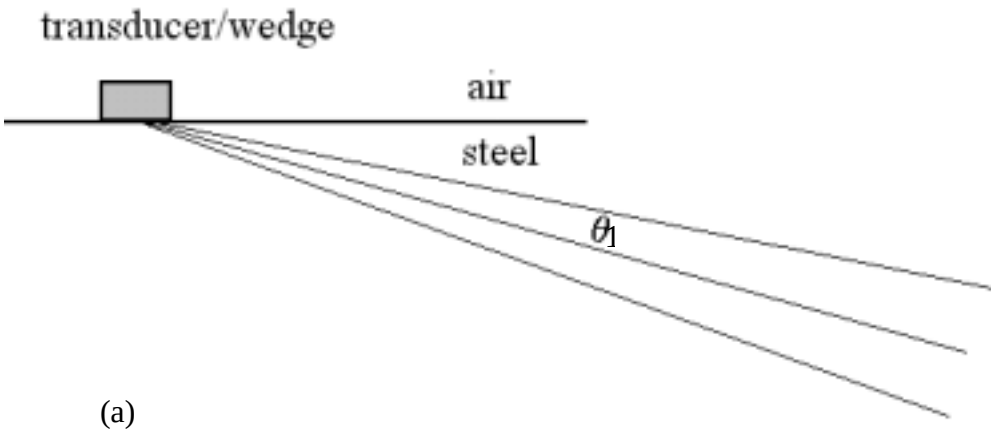

(a)

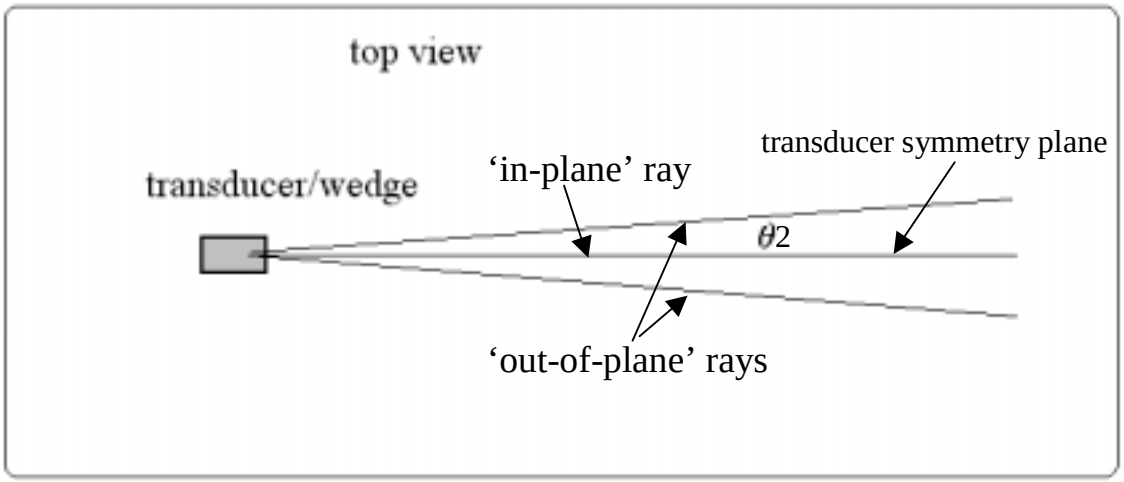

(b)

Figure 10.1. Radiation by transducer into steel half-space represented a angle-dependent point source.

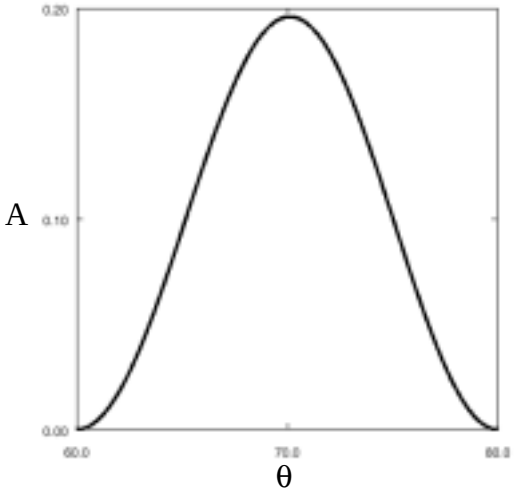

Figure 10.2. Angular aperture function.

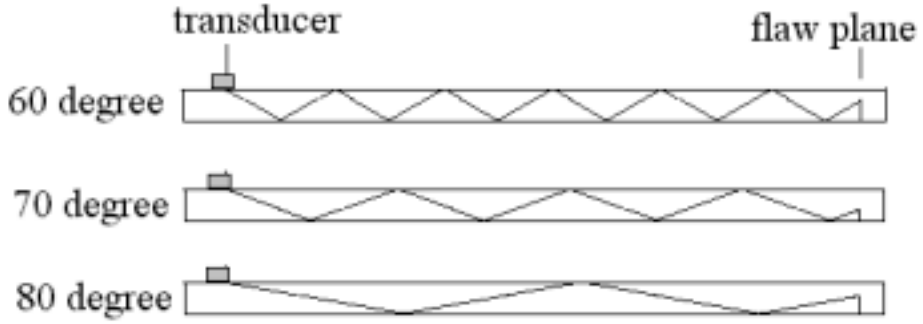

Figure 10.3. In-plane ray propagation in flat shell section.

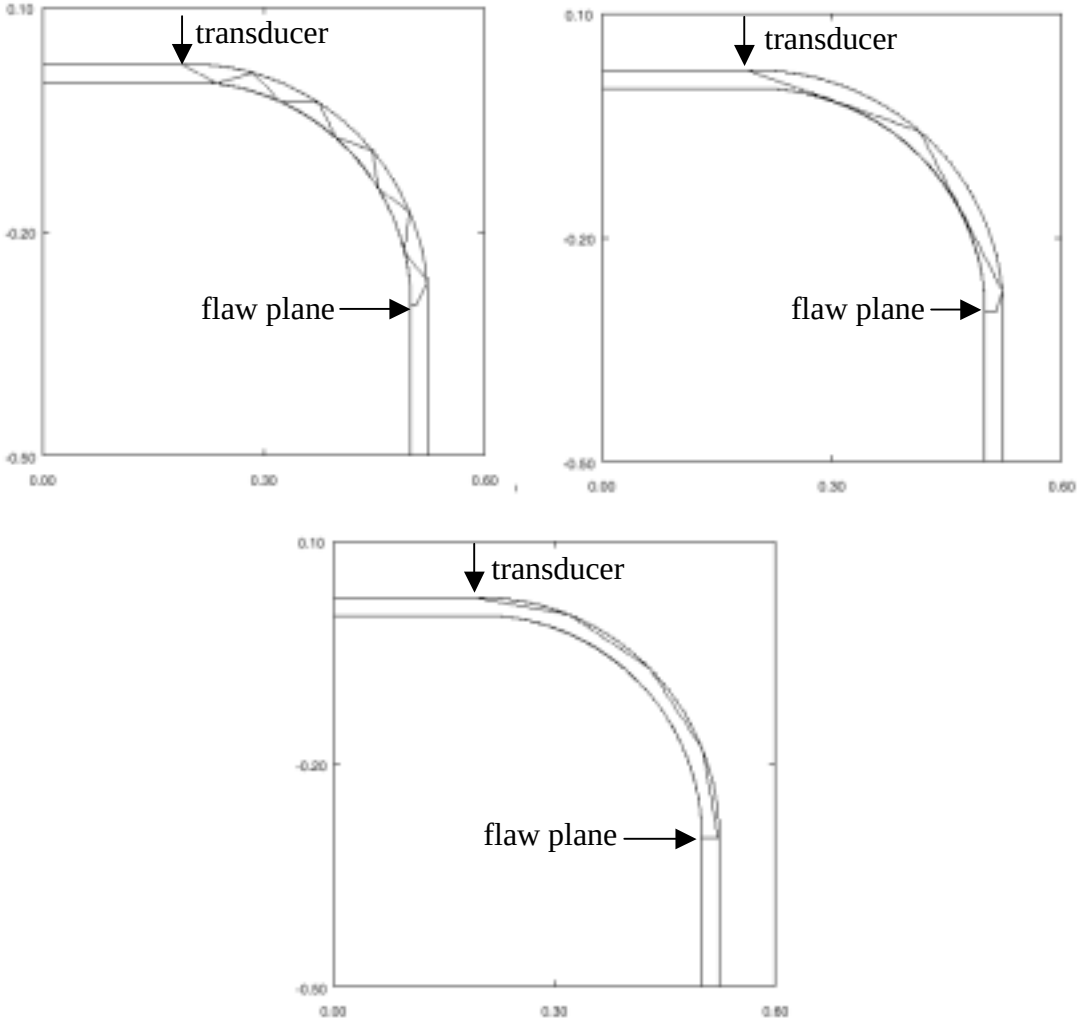

Figure 10.4. Ray propagation in curved shell section: (a) 60-degree, (b) 70-degree, and (c) 80-degree.

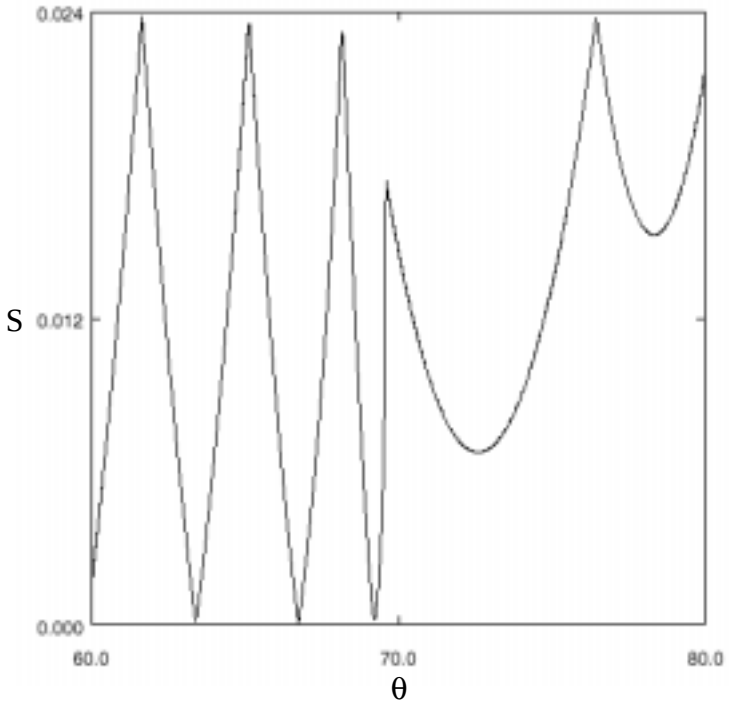

Figure 10.5. Ray intersection position s on shell cross-section versus transmission angle θ.

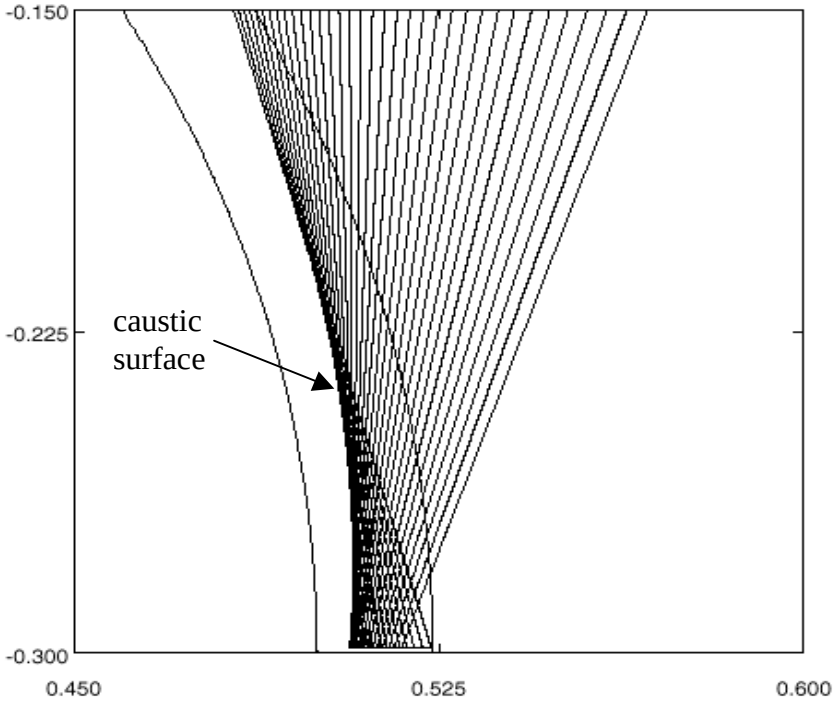

Figure 10.6. Caustic surface formed by focusing of rays transmitted at 69.6 < θ < 76.4-degrees.

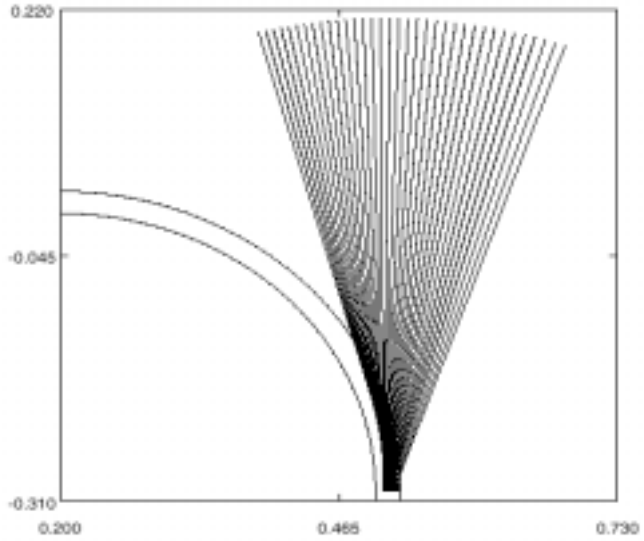

Figure 10.7. Equivalent aperture surface formed by back-propagation of rays in Figure 10.6.

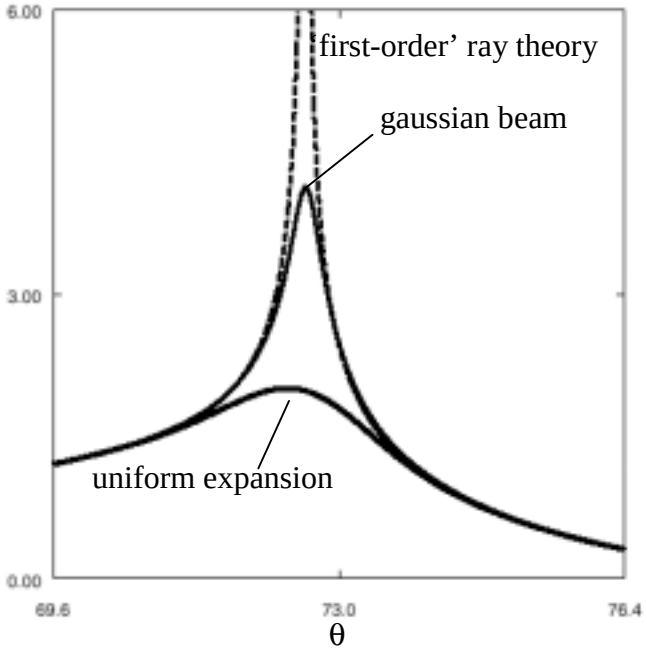

Figure 10.8. Ray amplitude on shell cross-section as function of transmitted ray angle.

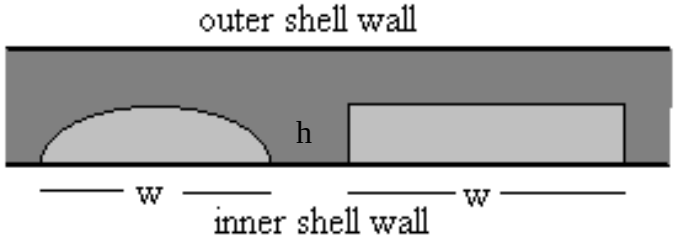

Figure 10.9. Crack geometry in the perpendicular cross-sectional surface of the shell.

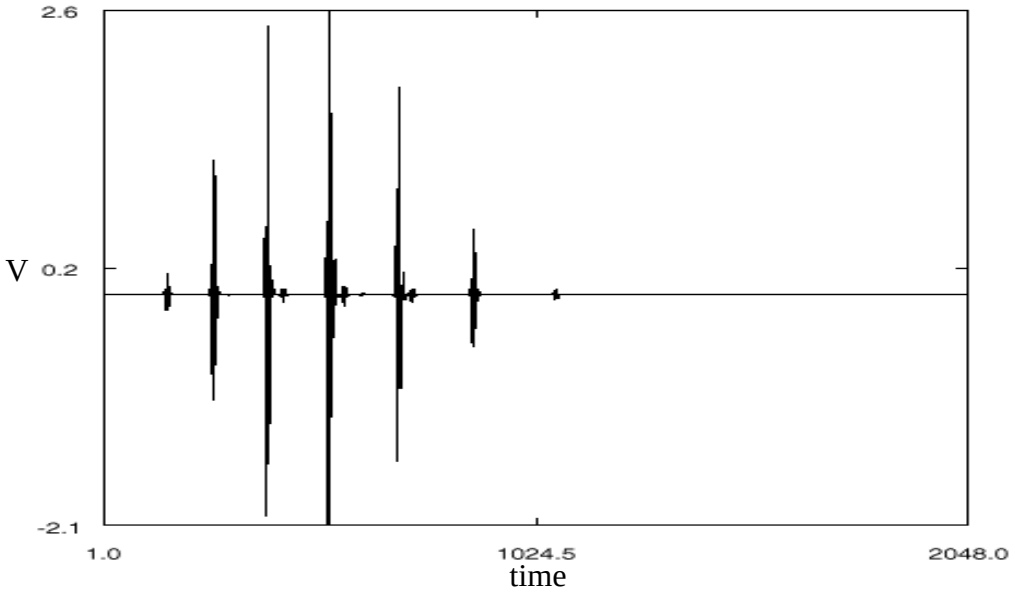

Figure 10.10. Signal reflected from edge of flat shell section at a distance of 483 mm (19 in.). Width of horizontal axis is 73.1 microsec.

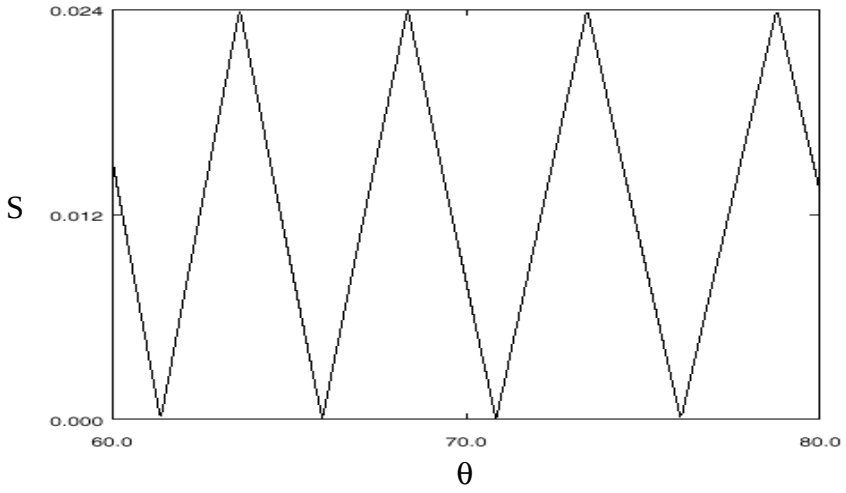

Figure 10.11. Ray intersection position s on shell cross-section versus transmission angle θ.

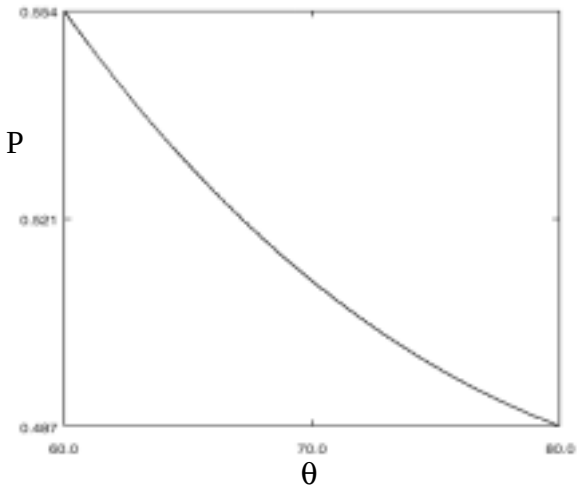

Figure 10.12. Ray path length p versus transmission angle on cross-section for flat shell.

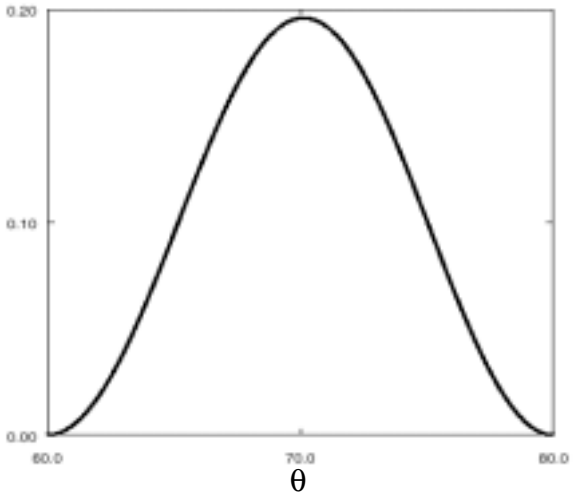

Figure 10.13. Ray amplitude |ψ| versus transmission angle on cross-section for flat shell.

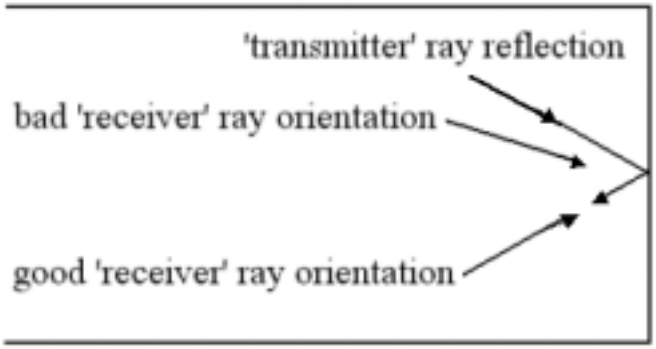

Figure 10.14. Relative orientation of ‘transmitter’ and ‘receiver’ rays at cross-sectional surface.

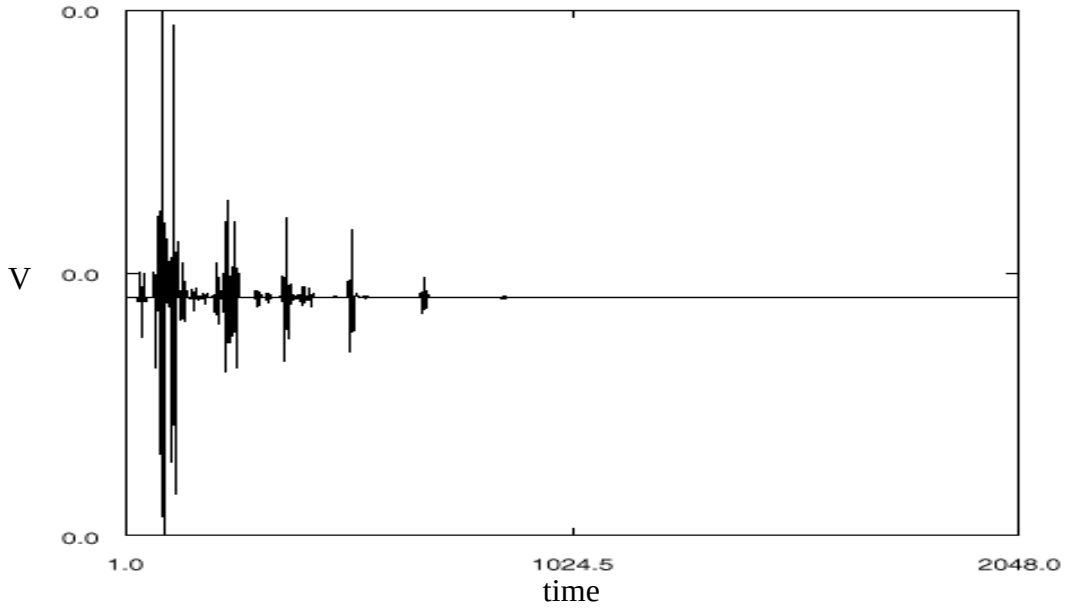

Figure 10.15. Signal reflected from edge of curved shell section at a distance of 483 mm (19 in.). Width of horizontal axis is 73.1 microsec.

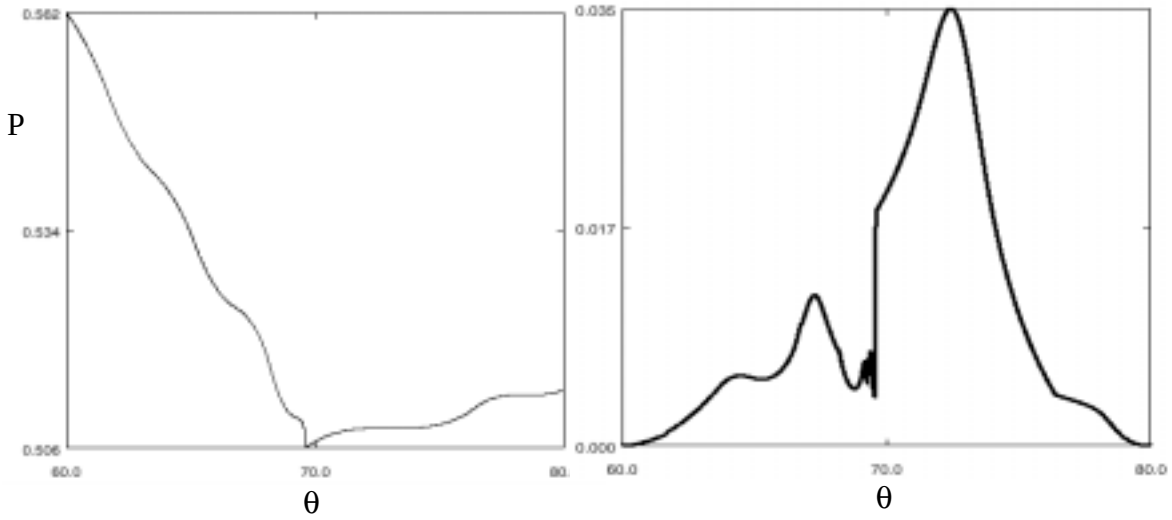

Figure 10.16. Ray path length p versus transmission angle on cross-section for the curved shell.

Figure 10.17. Ray amplitude |ψ| versus transmission angle on cross-section for the curved shell.

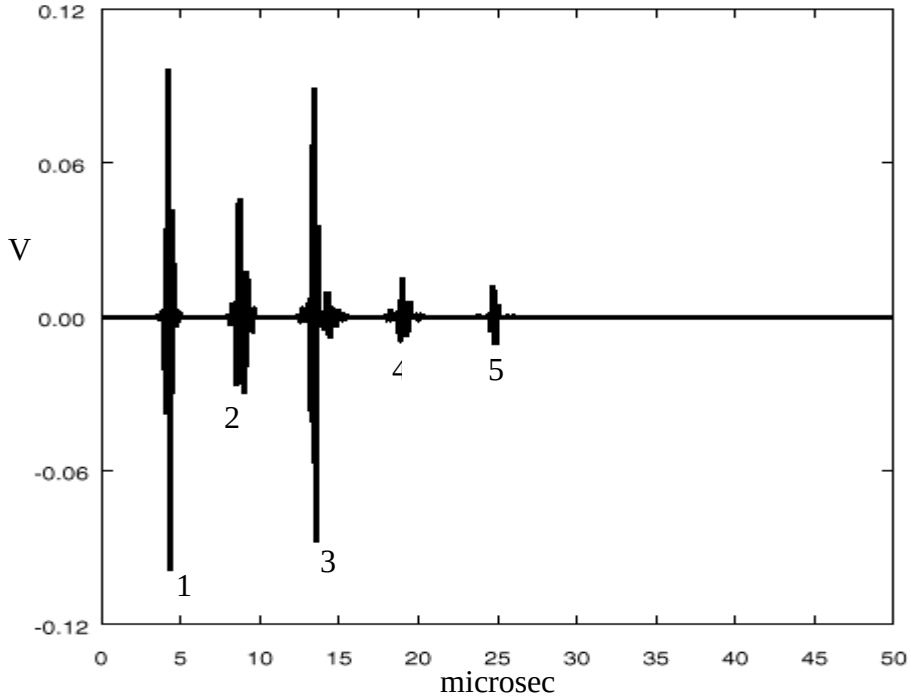

Figure 10.18. Wave train 20% through-wall crack on inside shell wall at knuckle-bottom transition. Plot begins at 328.18us past initial trigger.

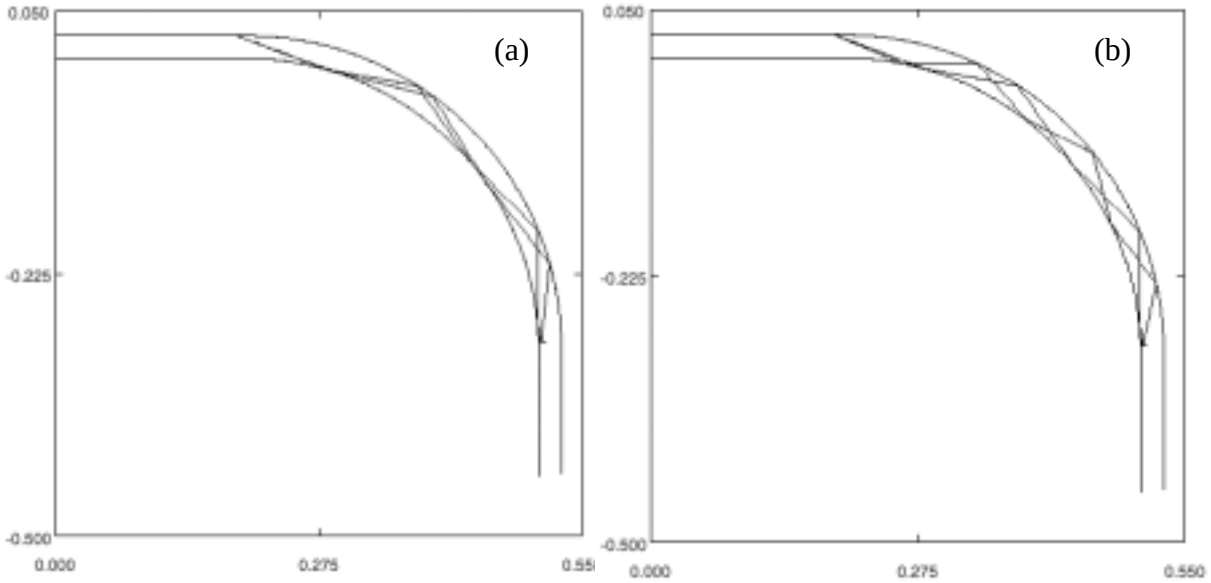

Figure 10.19. Ray path combinations contributing to the signal in Figure 10.18.

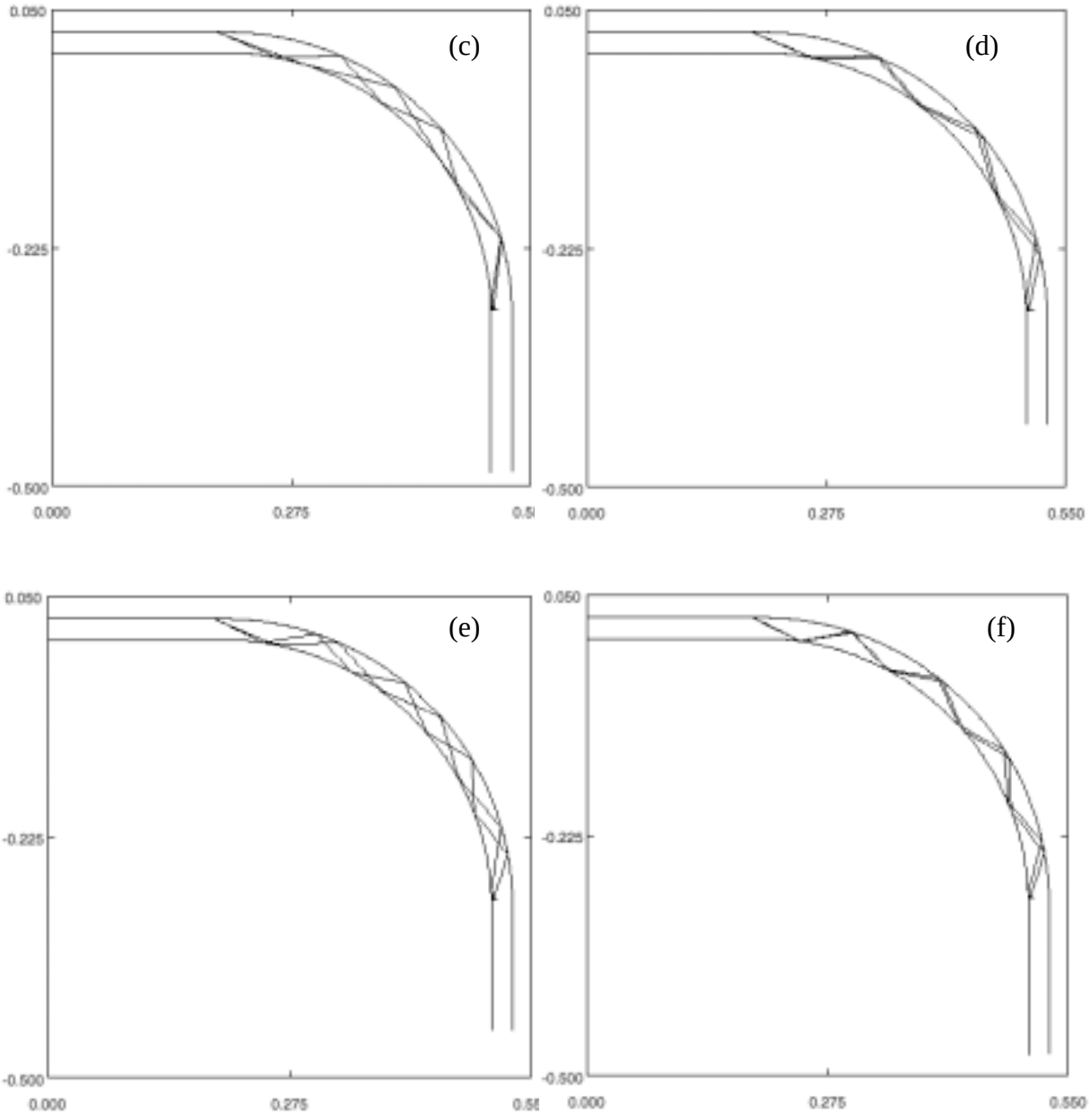

Figure 10.19. (cont.) Ray path combinations contributing to the signal in Figure 10.18.

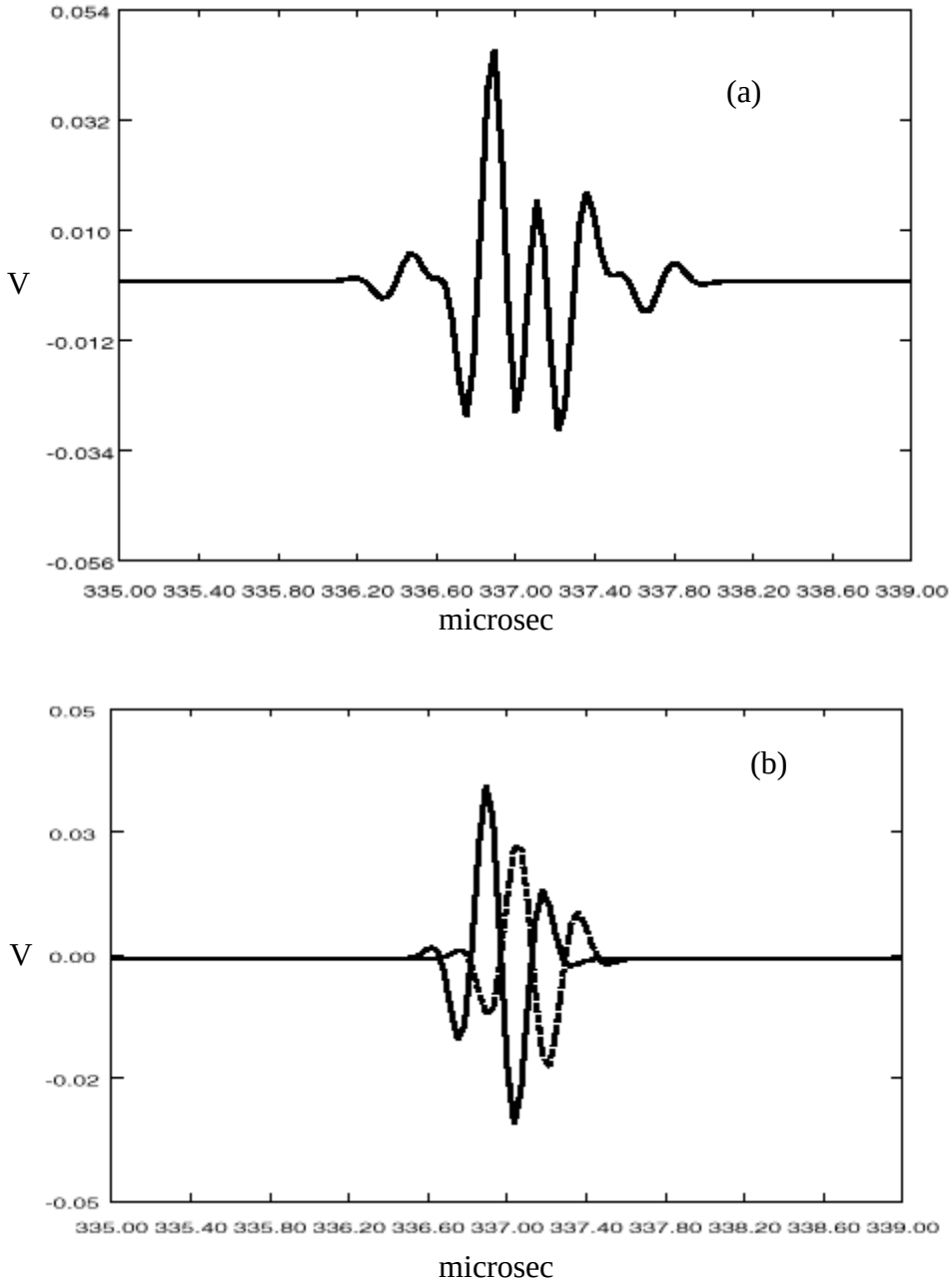

Figure 10.20. (a) Expanded view of signal component 2 in Figure 10.18, (b) signal contributions to signal in Figure 10.20a from ray paths of Figure 10.19b (—) and Figure 10.19c (---).

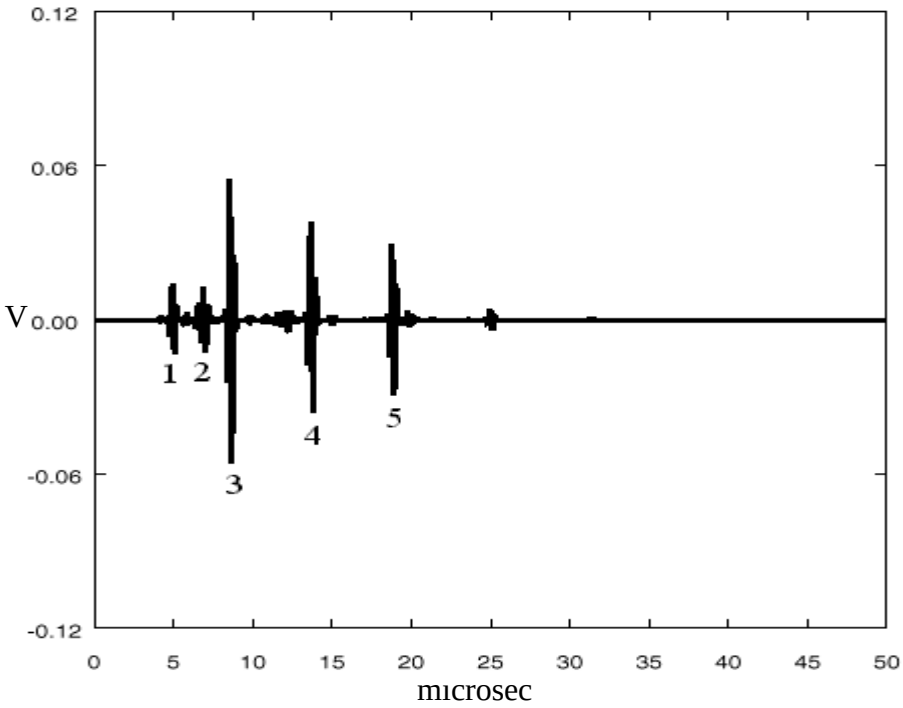

Figure 10.21. Wave train 20% through-wall crack on outside shell wall at knuckle-bottom transition. Plot begins at 328.18us past initial trigger.

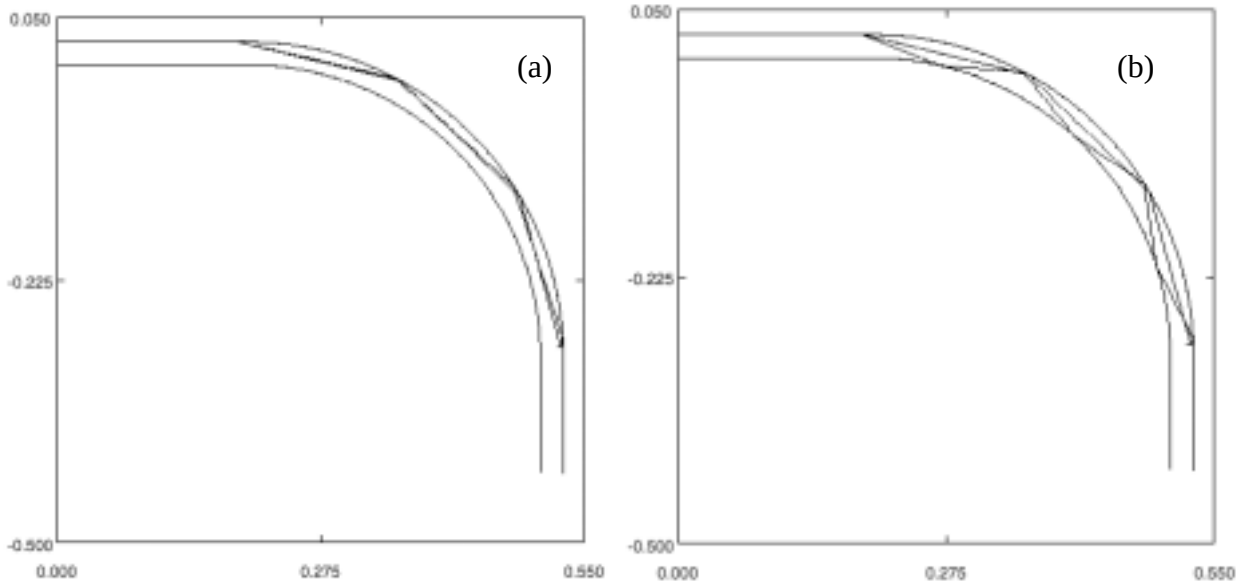

Figure 10.22. Ray path combinations contributing to the signal in Figure 10.21.

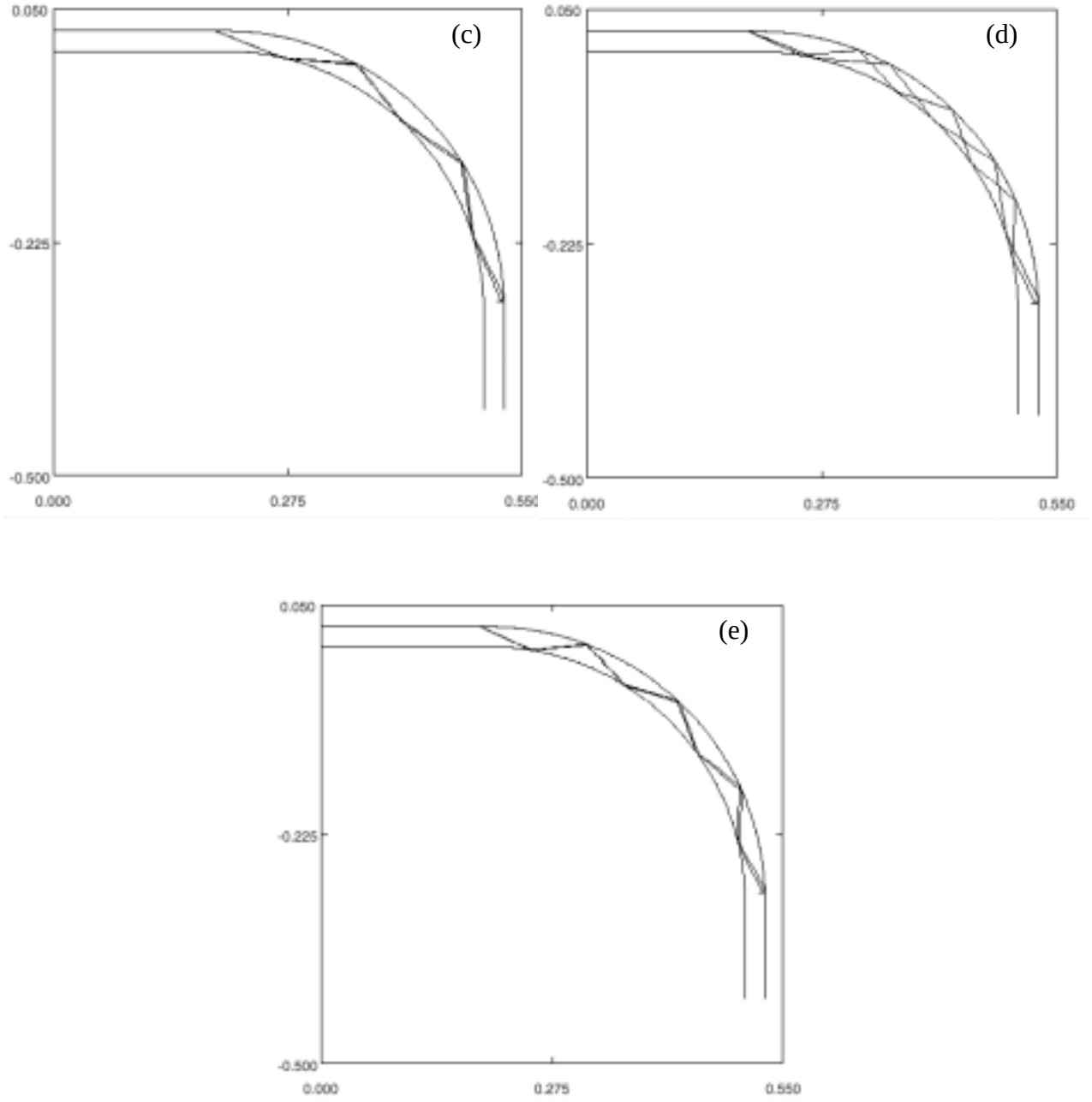

Figure 10.22. (cont.) Ray path combinations contributing to the signal in Figure 10.21.

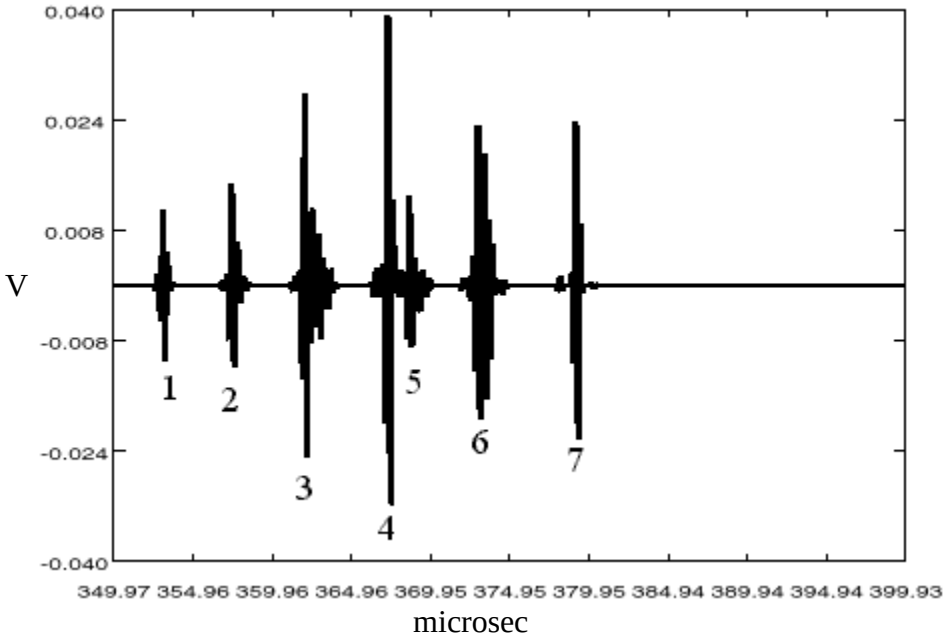

Figure 10.23. Wave train for 20% through-wall crack on inside shell wall at knuckle-bottom transition using separate transmitter and receiver.

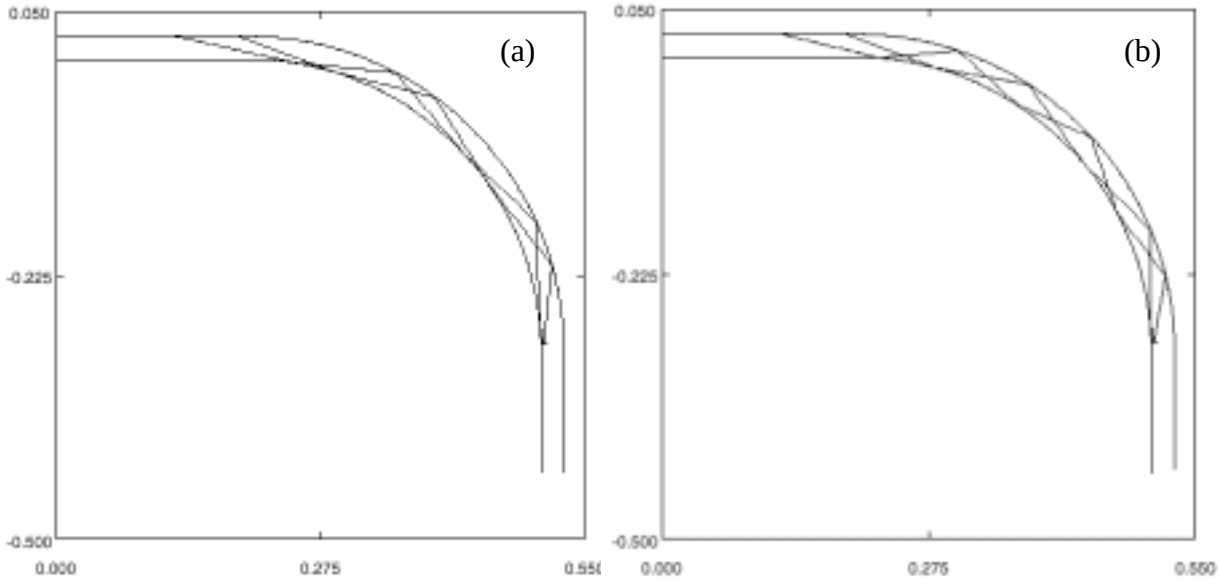

Figure 10.24. Ray path combinations contributing to the signal in Figure 10.23.

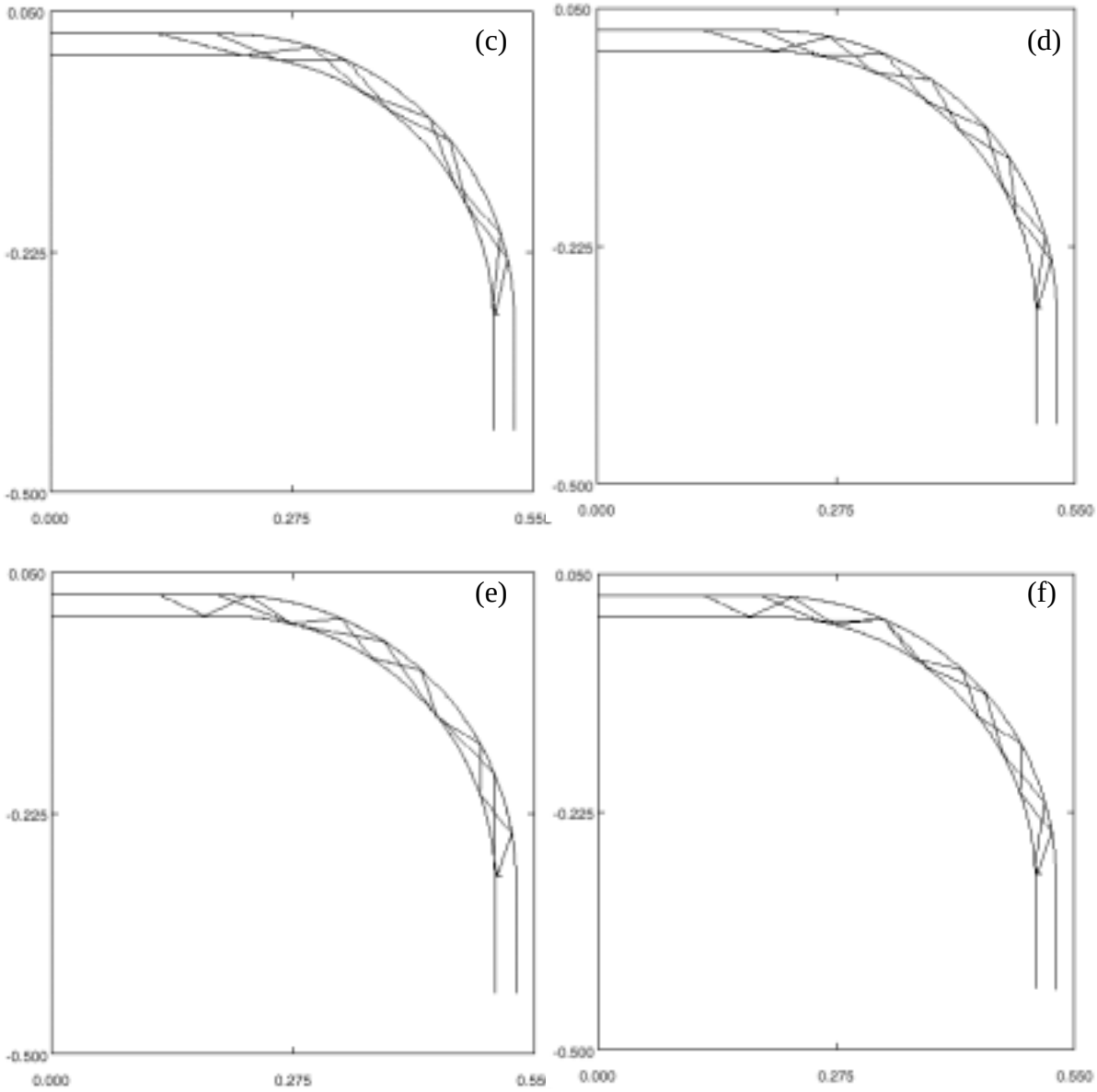

Figure 10.24. (cont.) Ray path combinations contributing to the signal in Figure 10.23.

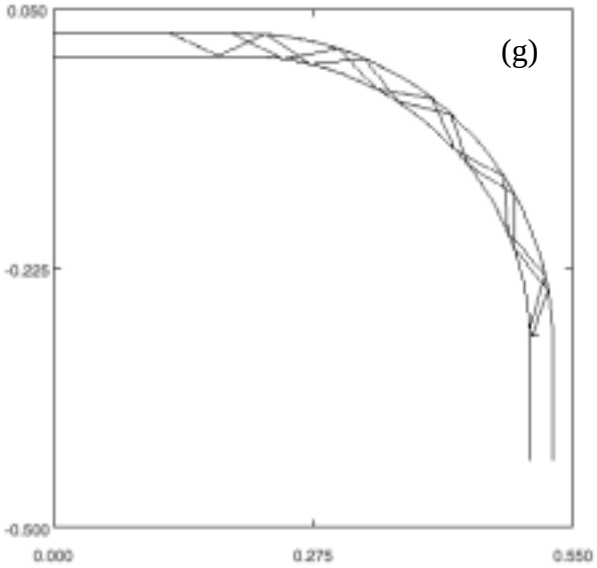

Figure 10.24. (cont.) Ray path combinations contributing to the signal in Figure 10.23.

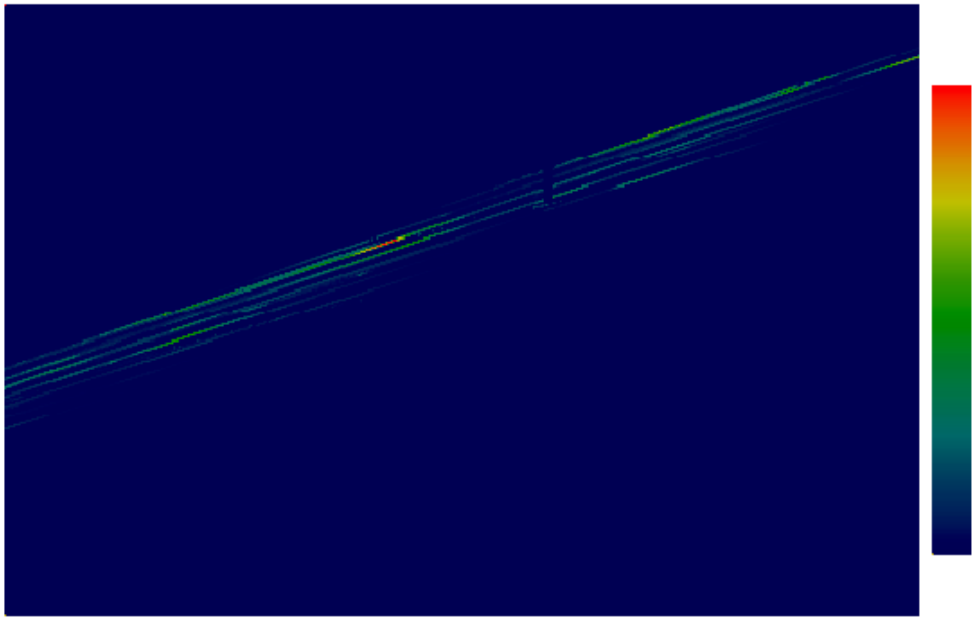

Figure 10.25. Computed B-mode image. Horizontal range from left to right –335 to –81 mm (–13.2 to –3.2 in.) Vertical range from top to bottom 213.8 to 528.72 microseconds.

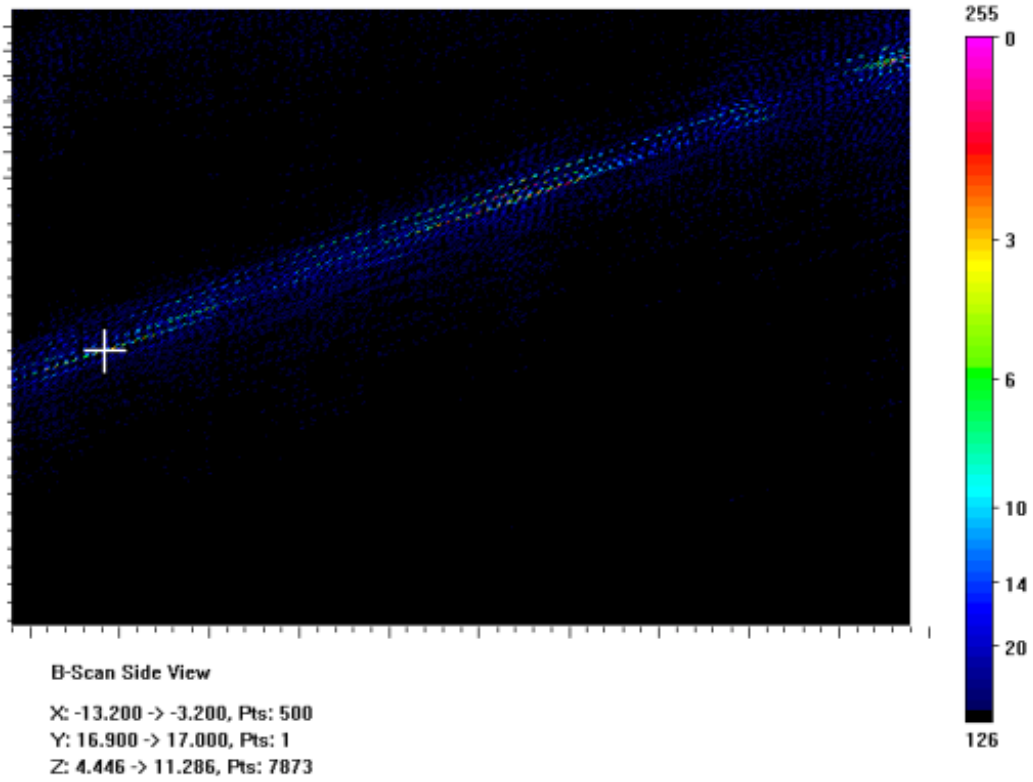

Figure 10.26. Experimental B-mode image. Horizontal range from left to right — 335 to –81 mm (–13.2 to –3.2 in.). Vertical range from top to bottom 213.8 to 528.72 microseconds.

11 FY01 Demonstrations

Two demonstrations were performed in FY01 to show the capability of the RONDE system. The first demonstration showed the RONDE deployment on a large tank mockup utilizing a deployment platform.

Figure 11.1. RONDE Being Deployed from Platform onto Tank Wall

Figure 11.1 shows the RONDE system deploying off the platform and onto the tank wall. The RONDE is driven down to the tank knuckle and positioned for scanning.

Figure 11.2 shows an NDE operator positioning the RONDE system for scanning on the mockup knuckle region.

Figure 11.2. NDE Operator Positioning the RONDE System for Scanning the Knuckle

The second demonstration was performed on a small tank knuckle mockup to demonstrate RONDE's ability to scan the knuckle and provide detection and sizing of simulated flaws. Figure 11.3 shows visitors at the laboratory during the demonstration.

Figure 11.3. Al Pardini from PNNL Provides an Overview of the RONDE System to DOE-RL and PNNL Management.

Figure 11.4. TFA Safety Technical Integration Manager Mike Terry Views the RONDE System

12 Conclusions

The design, development, and initial testing of a prototype system to examine the knuckle region of a DST have been completed. Data gathered this year demonstrated the prototype system's capability utilizing a combination of pulse-echo SAFT and tandem-SAFT inspection methodologies to perform flaw detection, localization and sizing in the knuckle region and onto the tank floor at distances of up to 1067 mm (42 in.) from the transducer and greater. The preliminary studies using pulse-echo, 70° shear wave inspection modality coupled with SAFT processing were successfully demonstrated as an effective examination method for detection and localization of machined simulated flaws (saw cuts) over a range of depths 2 mm to 14.4 mm (0.08 in. to 0.57 in.), and over long path lengths, approximately 1067 mm (42 in.) and beyond. An evaluation of the tandem, 70° shear wave inspection modality coupled with tandem-SAFT processing was conducted on the various mockups and has provided a robust and effective method for sizing those indications detected and localized by the pulse-echo technique.

In support of the prototype system testing, three tank knuckle mockups were fabricated from carbon steel. The mockups contained a variety of machined defects that simulate cracks in the knuckle region as well as on the tank floor. These mockups proved invaluable in supporting the development effort. The mockups allowed PNNL researchers to test different system protocols in an effort to provide the best system configuration for characterization of the tank flaws.

Results of initial tests of the RONDE system exceeded PNNL's performance expectations. The entire set of simulated defects in all of the mockups were readily detected. PNNL sized all of the flaws located in the knuckle region. The sizing results are shown here. The RMS error associated with the sizing demonstration was 1.2 mm (0.047 in.), well within the Hanford requirements of 2.54 mm (0.10 in.).

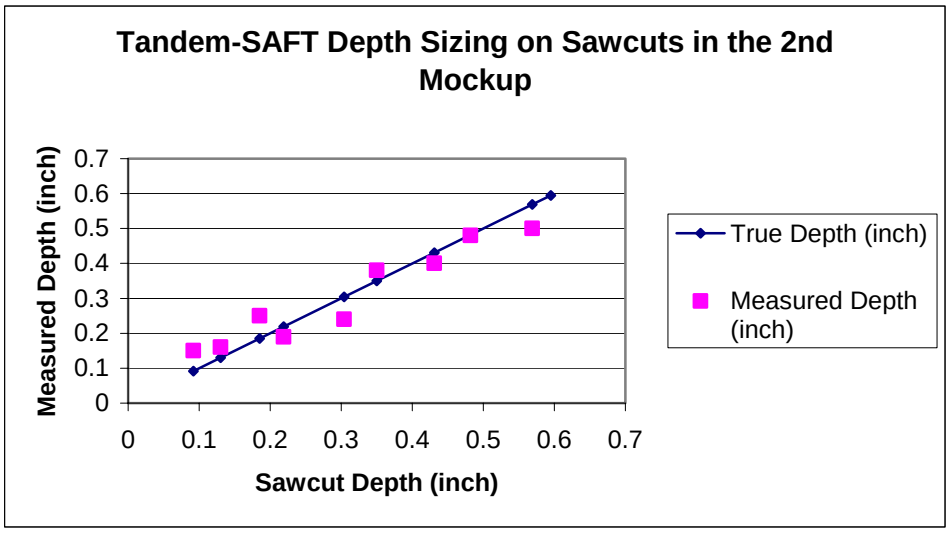

An area for further study is in sizing deep flaws near the second weld. From preliminary results, the seventy percent through-wall saw cut was not accurately sized due to complexities from both the large depth and the large axial distance around the knuckle. As the ultrasonic energy travels further around the knuckle it becomes more complex and has more signals in its wave packet. This occurs in large part due to the different wave modes, different V-paths or bounces, and beam spread due to the long part path and knuckle effects. To reach the second weld of the knuckle, the sound is on its ninth or greater bounce off the inner surface (9/2 V path). This long part path contributes to the multiple reflections. The large depth (70%) complexity is from the long walk in time associated with a deep flaw. Spatially, the signal is detected over a large region in the axial direction. However this long signal walk is broken up by the different modes or bounces from the same flaw resulting in an under sizing of the flaw. The flaw was sized at 9.4 mm (0.37 in.) deep. If a 9.4 mm (0.37 in.) depth is entered into Table 9.2, an RMSE of 2 mm (0.08 in.) is obtained. This is still within the required 2.54 mm (0.1 in.) sizing accuracy. PNNL plans to introduce 3 more deep (>70%) flaws into the mockup and ultrasonically examine these flaws in order to improve the sizing procedure and provide better sizing performance.

Preliminary length sizing data meets the 25.4 mm (1 in.) accuracy required. The ten and twenty-five percent through-wall saw cuts were ultrasonically sized at 40.6 and 45.7 mm (1.6 and 1.8 in.) respectively. The reported values in Table 9.1 are 33 and 53.3 mm (1.3 and 2.1 in.) respectively. Additionally two ten percent notches from the third or calibration mockup were ultrasonically sized at 45.7 and 35.6 mm (1.8 and 1.4 in.) long. The axial location of these two notches are 375 and 521 mm (14.75 and 20.50 in.) from the first weld. Note that the second notch is past the second weld by approximately 38 mm (1.5 in.). These notches were machined at 36 mm (1.4 in.) in total length.

13 FY 02 Plans

13.1 Acceptance Testing

Formal acceptance testing of the RONDE system will take place in the 2nd quarter of FY 02. Acceptance testing will demonstrate the RONDE's readiness for deployment into the annulus of a Hanford waste tank. An acceptance test plan will be written which will provide the guidelines for the test process. Testing will be performed on existing mockups.

13.2 Performance Demonstration Testing

Once the RONDE system has completed acceptance testing, it will be readied for the Performance Demonstration Test (PDT). A PDT tests the system's capability against a known flaw set. Prior to performing the PDT, selected NDE operators will be trained to operate the RONDE system. Once this training has been completed, the NDE operators will perform the PDT on a knuckle mockup that has real intergranular stress corrosion cracks (IGSCC) in it. The PDT is a blind test and PNNL will evaluate the NDE operator's capability to detect, locate, and size the IGSCC. PNNL has been contracted in FY02 to fabricate a knuckle mockup with real IGSCC.

13.3 Readiness Review

During the 2nd and 3rd quarters of FY02, the RONDE system will undergo a readiness review. CH2M Hill Hanford Group (CHG) will have the lead for coordinating this effort.

13.4 Deployment onto Hanford Waste Tank

It is anticipated that the RONDE system will be ready for deployment into the annulus of a DST in the 4th quarter of FY02.

14 References

Auld, B.A. 1979. *General Electromechanical Reciprocity Relations Applied To The Calculation of Elastic Wave Scattering Coefficients*, Wave Motion 1, pp.3-10.

Busse, L. J., H. D. Collins, and S. R. Doctor. 1984. *Review and Discussion of the Development of Synthetic Aperture Focusing Technique for Ultrasonic Testing (SAFT-UT)*, NUREG,CR-3625. U.S. Nuclear Regulatory Commission, Washington, D.C.

Hall, T. E., L. D. Reid, and S. R. Doctor. 1988. *The SAFT-UT Real-Time Inspection System - Operational Principles and Implementation,* NUREG/CR-5075. U.S. Nuclear Regulatory Commission, Washington, D.C.

Jensen, C. E., 2001. *Engineering Task Plan for the Ultrasonic Inspection of Hanford Double-Shell Tanks-FY2001,* RPP-6839, CH2M Hill Hanford Group, Inc., Richland, Washington.

Pardini, A. F., and A. A. Diaz. 2000. *Evaluation of SAFT/T-SAFT Technology for the Inspection of Hanford's Double Shell Waste Tank Knuckle Regions*, PNNL-13321, Pacific Northwest National Laboratory, Richland, Washington.

Pardini, A. F., and T. J. Samuel. 2001. *Functions and Requirements for the DST Knuckle Region Ultrasonic Scanning System*, PNNL-13436, Pacific Northwest National Laboratory, Richland, Washington.

Pfluger, D. C. 1994. *Double-Shell Tank Ultrasonic Inspection Plan*, WHC-SD- WM-AP-019, Westinghouse Hanford Company, Richland, Washington.

Pfluger, D. C. 1995. *Double-Shell Tank Ultrasonic Inspection Performance Specification*, WHC-S-4108, Westinghouse Hanford Company, Richland, Washington.

Roberts, R. A., A. F. Pardini, and A. A. Diaz. 2001. *A Model for High Frequency Guided Wave Inspection of Curved Shells,* Review of Progress in Quantitative NDE, Bowdoin College, Brunswick, Maine, July 29-August 3, 2001.

Shurrab, M. S., M. D. Thomson, J. R. Friley, M. R. Garnich, M. W. Rinker and F. A. Simonen. 1991. Parametric Studies to Support Inspection Criteria of the Hanford Site Double-Shell Waste Storage Tanks, WHC-EP-0508, Westinghouse Hanford Company, Richland, Washington.

Appendix A

Demonstration Test Plan

Remotely Operated Nondestructive Examination System

Demonstration Test Plan

Pacific Northwest National Laboratory
NDE Measurements Group
2400 Stevens Drive – Mail Stop K5-26
Richland, Washington 99352

Table of Contents

1.0 Item Identification

The system to be demonstrated is the Remotely Operated Nondestructive Examination (RONDE) system. The system includes the magnetic wheel crawler, ultrasonic scanning bridge, remote data acquisition electronics, data acquisition computer, and the data analysis computer.

2.0 General Description

The objective of this demonstration is to show that the RONDE system is operational and ready to perform the task of inspecting the knuckle region of the underground waste storage tanks at the Department of Energy's Hanford Site. The demonstration will not include radiation testing or all environmental testing. These factors were reviewed during the design phases of the development of the RONDE system and were deemed acceptable based on the published data on radiation and environmental components used in the design of the RONDE system. Upon completion of this Demonstration Test Procedure (DTP), the RONDE system will be made ready to undergo an Acceptance Test (ATP) and a performance demonstration test (PDT) to be qualified for inspecting Hanford's DST knuckles.

3.0 Demonstration Condition Limits

Conditions that could cause the demonstration to be aborted would be a loss of power in the test facility, or a complete failure of the RONDE system to perform its intended functions. If either of these occur, the demonstration will be aborted until the problems are resolved. Once resolved, the DTP will be repeated.

Instruments & Calibration

During the DTP the RONDE system will be inspecting various knuckle mockups. Simple sketches of the flaw indications will be provided to those witnessing the DTP for information only.

Facilities, Equipment, and Materials

The RONDE system shall be demonstrated on the large CH2M Hill Hanford Group (CHG) mockup located in the 300 area, as well as on smaller mockups located in PNNL's 2400 Stevens Robotics Laboratory, room 1444. The equipment and materials listed below are necessary to perform this demonstration:

RONDE system, including the magnetic wheel crawler, ultrasonic scanning bridge, remote data acquisition electronics, data acquisition and data analysis computers, and all interconnecting cables.

110VAC power source
Large CHG carbon steel knuckle mockup
Small PNNL carbon steel knuckle mockups
Miscellaneous (e.g. common tools, duct tape, etc)

4.0 Safety

The RONDE system is a completely enclosed ultrasonic scanning system, therefore no external wires or mechanical assemblies will be exposed as a shock hazard. All voltages on the scanning assembly are low voltage direct current. During the demonstration, the magnetic wheel crawler will be deployed on the large carbon steel mockup. The magnetic wheels are very powerful, therefore extreme caution should be used to avoid pinches to hands and fingers. The magnetic wheel crawler will be tethered to avoid falling to the ground in case the magnetic wheels become detached from the tank wall.

5.0 Maintenance & Failures

There are no components within the RONDE system that should require maintenance during the demonstration. If any component fails during the demonstration, and it can be replaced immediately without impacting the rest of the demonstration, then the demonstration shall continue. If the failure is catastrophic (component can not be readily replaced or needs to be reordered), then the demonstration shall be stopped and repeated at a later date.

The extent of the RONDE system demonstration test should be relatively short in duration, so no interruptions are anticipated.

6.0 Personnel Requirements

Battelle RONDE operations staff that have been so designated by the Battelle RONDE Project Manager shall perform the operation of the equipment.

7.0 Procedure

Appendix A of this document provides the step-by-step procedure for demonstration testing the RONDE system.

8.0 Disposition of Test Item(s)

Upon completion of the demonstration test, all test materials will remain in Battelle's Robotics Laboratory for future use. The RONDE system shall be readied for acceptance testing.

APPENDIX A

RONDE DEMONSTRATION TEST PROCEDURE STEPS

A-1.0 DEMONSTRATION TEST PROCEDURE

A-1.1 Demonstrate Deployment of RONDE System

1.1.1 Transport the RONDE system to the large double shell tank mockup.

1.1.2 Verify that all RONDE components are properly connected prior to energizing the system.

1.1.3 Place the RONDE magnetic wheel crawler and scanning bridge on the deployment platform.

1.1.4 Lower the deployment platform into the 24 inch riser and configure the platform for unloading the crawler.

1.1.5 Utilizing the RONDE joystick, drive the crawler off of the platform onto the primary tank wall of the mockup. Remove the deployment platform.

1.1.6 Using the RONDE joystick, drive the crawler into position for scanning the knuckle region of the primary tank.

1.1.7 Lower the deployment platform back into the 24 inch riser and configure the platform for loading the crawler.

1.1.8 Using the RONDE joystick, drive the crawler onto the platform for removal.

1.1.9 Remove the platform and RONDE magnetic wheel crawler and scanning bridge from the mockup.

A-1.2 Demonstrate Flaw Detection

1.2.1 Transport the RONDE system to the small mockup which has simulated flaws (i.e. sawcuts and notches).

1.2.2 Verify that all RONDE components are properly connected prior to energizing the system.

1.2.3 Place the RONDE magnetic wheel crawler and scanning bridge on the small mockup.

1.2.4 Using the RONDE joystick, drive the crawler into position for scanning the knuckle region.

1.2.5 Once in position, initiate a scan using the SAFT software.

1.2.6 Display the existing C-Scan plot of the data to demonstrate system capability to detect flaws.

1.2.7 Reset the scanning bridge to the starting position and prepare for TSAFT scanning.

A-1.3 Demonstrate Sizing

1.3.1 Using the coordinate information from the detection scan, position the scanner for TSAFT scanning.

1.3.2 Locate the flaw using the A-Scan display.

1.3.3 Change electronic settings for TSAFT.

1.3.4 Using the SAFT jog function, peak the A-Scan display.

1.3.5 Using the SAFT jog function, separate the two scanning transducers.

1.3.6 Initiate the TSAFT.

1.3.7 Display the existing C&B-Scan views of the data for sizing.

1.3.8 Initiate a 6 dB clip of the data and using the cursor measure the height of the flaw indication.

Appendix B

Operating Procedure (Draft)

CH2MHILL Hanford Group

Draft Operating Procedure

DRAFT

Remotely Operated Nondestructive Examination System

Operating Procedure

Prepared by:

Pacific Northwest National Laboratory
NDE Measurements Group
2400 Stevens Drive – Mail Stop K5-26
Richland, Washington 99352

Table of Contents

1.0 Item Identification

This procedure provides for the operation of the Remotely Operated Nondestructive Examination (RONDE) system. The system includes the magnetic wheel crawler, ultrasonic scanning bridge, remote data acquisition electronics, data acquisition computer, and the data analysis computer.

2.0 General Description

The RONDE system is composed of three main components:

- RONDE magnetic wheel crawler and scanning bridge
- Tank top electronics
- Control station

The diagram shown in Figure 2.1 provides the general layout of components at the tank farm. Approximately 100 ft. of multi-conductor cable separates the crawler/scanning assembly from the tank top electronics. Approximately 425 ft. separates the tank top electronics from the control station. This 425 ft. connection consists of a small multi-conductor cable and a single fiber optic cable with two fibers.

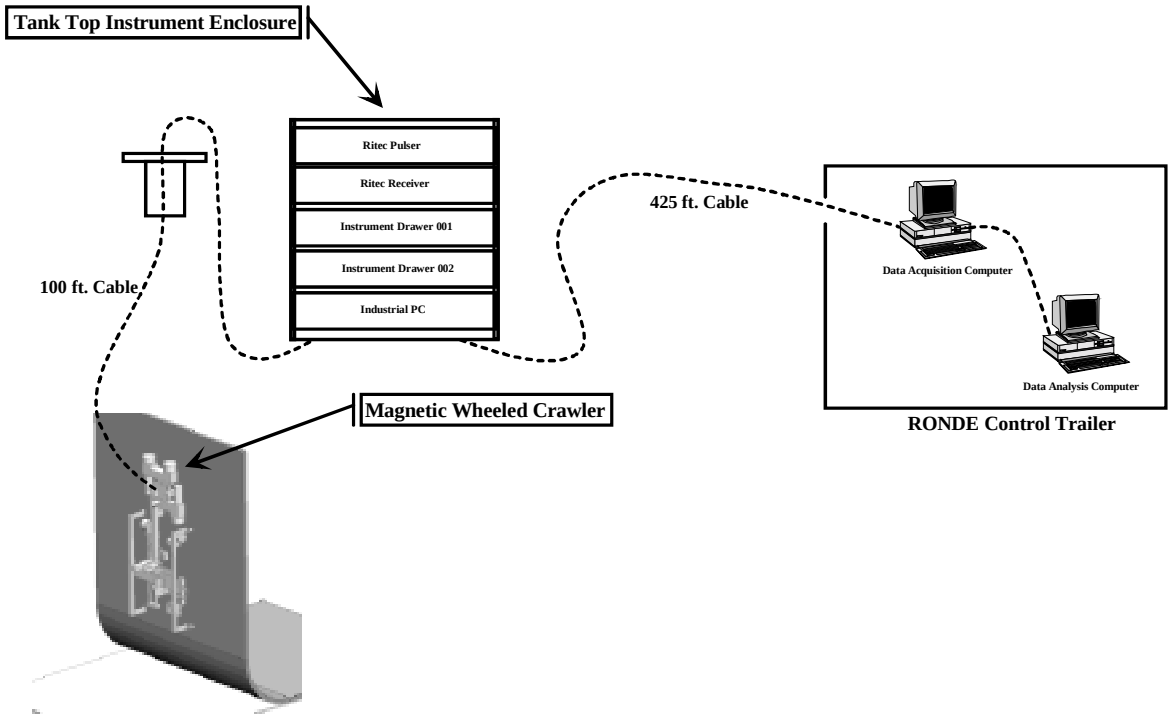

Figure 2.1 General Layout Diagram

3.0 Condition Limits

Conditions that could cause the RONDE system to not operate would be a loss of power at the tank farm, or a complete failure of the RONDE system to perform its intended functions. If either of these occur, the operation of the RONDE will be stopped until the problems are resolved. Once resolved, the operation of the RONDE will continue.

Instruments & Calibration

The RONDE system will require calibration for proper defect characterization. Utilizing the calibration standard, the RONDE transducers and associated electronics will be calibrated.

Facilities, Equipment, and Materials

Operation of the RONDE system will require 110 VAC power at the tank top as well as in the control station. Trained operators shall perform all necessary activities related to placing the RONDE into the tank annulus and deploying it to the knuckle region for inspection.

4.0 Safety

The RONDE system is a completely enclosed ultrasonic scanning system, therefore no external wires or mechanical assemblies will be exposed as a shock hazard. All voltages on the scanning assembly are low voltage direct current. The magnetic wheels are very powerful, therefore extreme caution should be used to avoid pinches to hands and fingers if crawler is placed near ferromagnetic materials. The magnetic wheel crawler will be tethered to avoid falling to the ground in case the magnetic wheels become detached from the tank wall.

5.0 Maintenance & Failures

Components within the RONDE system will require periodic maintenance. A maintenance schedule shall be followed to assure the RONDE will be capable of performing its inspection activities.

6.0 Personnel Requirements

CH2M Operations staff that have been properly trained shall perform the deployment of the RONDE system. Qualified and certified NDE staff (qualified and certified to the American Society for Nondestructive Testing – ASNT) shall perform all NDE related activities.

7.0 Procedure

Appendix A of this document provides the step-by-step procedure for deployment and operating the RONDE system.

APPENDIX A

RONDE Deployment and Operating STEPS

A-1.0 RONDE DEPLOYMENT AND RETRIEVAL PROCEDURE

A-1.1 Deployment of RONDE System

1.1.1 Transport the RONDE system to the double shell tank for inspection.

1.1.10 Verify that all RONDE components are properly connected prior to energizing the system.

1.1.11 Perform all necessary calibration of the RONDE equipment using calibrated standards.

1.1.12 Place the RONDE magnetic wheel crawler and scanning bridge on the deployment platform.

1.1.13 Lower the deployment platform into the 24 inch riser and configure the platform for unloading the crawler.

1.1.14 Utilizing the RONDE joystick, drive the crawler off of the platform onto the primary tank wall. Remove the deployment platform.

1.1.15 Using the RONDE joystick, drive the crawler into position for scanning the knuckle region of the primary tank.

1.1.16 Perform the inspection of the tank knuckle per the NDE inspection procedure.

1.1.17 Lower the deployment platform back into the 24 inch riser and configure the platform for loading the crawler.

1.1.18 Using the RONDE joystick, drive the crawler onto the platform for removal.

1.1.19 Remove the platform and RONDE magnetic wheel crawler and scanning bridge from the mockup.

A-2.0 RONDE OPERATING PROCEDURE

2.1.1 Operation of the RONDE system during data acquisition shall be performed by qualified and certified NDE technicians.

2.1.2 Set all equipment settings according to NDE procedure.

2.1.3 Position RONDE crawler and scanning bridge into position for scanning the knuckle region.

2.1.4 Reset the encoder to 0 to prior to beginning first scan.

2.1.5 Using the digital inclinometer readout and the camera views from the annulus cameras, assure that the scanning system is approximately perpendicular to the upper knuckle weld and the end roller wheels are within 3 inches of the upper knuckle weld.

2.1.6 Lock the electromagnets.

2.1.7 Initiate the first pulse echo SAFT scan.

2.1.8 Review data and decide whether any flaws require T-SAFT.

2.1.9 If not further data is required release the electromagnets and move approximately 12 inches further around the circumference of the tank and repeat the scan sequence.

Distribution

No. of
Copies

Offsite

4 **DOE / Office of Scientific and Technical Information & Information Release**

1 **DOE Office of Science and Technology**
Kurt Gerdes
1154 Cloverleaf Building
19901 Germantown Road
Germantown, MD 20874-1290

Onsite

8 **Tanks Focus Area Technical Team**

B. J. Williams	K9-69

1 **Tanks Focus Area Program Manager**

T. P. Pietrok	K8-50

1 **Tanks Focus Area - Safety**

M. T. Terry	K9-91

1 **Hanford Site**

E. J. Cruz	H6-60

30 **Pacific Northwest National Laboratory**

J. M. Alzheimer (1)	K5-22
S. M. Bowyer (1)	K5-26
S. L. Crawford (1)	K5-26
A. A. Diaz (1)	K5-26
S. R. Doctor (1)	K5-26
K. L. Gervais (1)	K5-22
R. V. Harris (1)	K5-26
A. F. Pardini (15)	K5-26
G. J. Posakony (1)	K5-26
D. M. Riechers (1)	K5-26
T. J. Samuel (5)	K5-22
G. J. Schuster (1)	K5-26